AN INVESTIGATION OF RNR REGULATION IN FISSION YEAST BY CONFOCAL LASER SCANNING FRET AND NEAR-TIRF MICROSCOPY

By

Asma Hadi Mohammed

THIS DISSERTATION IS SUBMITTED

FOR THE DEGREE OF DOCTOR OF

PHILOSOPHY

AT

The University of Sussex

Falmer

Sussex, UK

April 2011

Declaration

I hereby declare that this thesis has not been and will not be, submitted in whole or in part to another University for the award of any other degree.

Signature:……

Date:…….

ABSTRACT

For genome integrity, adequate levels of deoxyribonucleotide (dNTPs) are essential to maintain faithful DNA replication and repair via the regulation of ribonucleotide reductase (RNR). In the fission yeast, RNR is composed of two subunits: Cdc22 and Suc22.

The importance of Spd1 (RNR inhibitor) in Cdc22-Suc22 complex formation has been demonstrated by imaging of *S. pombe* containing fluorescent protein (FP) modified RNR subunit proteins in the presence of Spd1 and absence of Spd1 cells using confocal laser scanning microscopy. To investigate further the significant role of Spd1 in the regulation of RNR, 41 mutants created by Nestoras group. We used fluorescence resonance energy transfer (FRET) by acceptor photobleaching to investigate the RNR subunit interaction and provide evidence for a new model for the role of Spd1 in RNR regulation. Different treatments such as HU, 4NQO and heat shock have been used to investigate the effect of radical scavenging on the inhibition of RNR activity and induced DNA damage on *S. pombe* cell viability to elucidate further the role of Spd1 in the regulation of RNR.

Finally a novel imaging technique, near-total internal reflection microscopy has been developed and applied with dual-view detection. The technique has been applied to image, simultaneously, the donor CFP and acceptor YFP channels of the FP-tagged RNR complex in the wild-type *S. pombe* cells and perform FRET measurements that are consistent with the confocal fluorescence results.

In conclusion, a new hypothesis for the role of Spd1 has been drawn from the results, which is that the inhibitory role of Spd1 mediates the Suc22-Cdc22 (R1-R2) interaction to form a FRET competent but immature and inactive RNR complex, while with Spd1 deleted RNR is clearly active in a conformation that lacks FRET.

Acknowledgments

After praising and thanking the God

I would like to thank my supervisor Dr. Mark Osborne for his support, encouragement, and helping me throughout my research project with his incredible patience. I think, Dr. Mark has truly introduced me to the world of biophysics. I would also like to thank Prof. Antony Carr and his group in the genome damage and stability centre for their helpful advice. I am extremely grateful to Dr. Adam Watson for teaching me the basics of the biological aspects of the project. My thanks also to Dr. Kostantinos Nestoras, who supported me a lot in the biochemistry aspects of the project. Also, I would like to thank a colleague on the project, Ann-Sofie Schreurs, who worked with me around two years and who has made a great effort to learn and continue this project.

I am grateful to our group member Remi Boulineau and Liz Atkinson for their support. I would also like to thank Dr. Roger Philips for helping me in the confocal microscopy technique.

I would like to thank the Swedish government for giving me this great opportunity and funding me during these three years.

Finally I want to thank my husband Majid, whose constant smile, support and praying during these years have been the source of my ambition. Also I would thank my family and my parents who gave me the strength to finish this PhD.

Table of Contents

List of Figures

List of Tables

List of Abbreviations

4NQO	4-NitroQuinoline 1-Oxide
Amp.R	Ampicillin Resistance.
BP	Bandpass
bp	Base Pairs
Cdc22	Cell division cycle
CDK	Cycline-Dependent Kinase
CFP	Cyan Fluorescent Protein.
CLSM	Confocal Laser Scanning Microscopy
COP9	Signalosome complex
CSN	Catalytic subunit of the signalosome
dNDP	Deoxy nucleotide diphosphates
dNTP	deoxyriboNucleoside TriPhosphate
DSB	Double Stranded Break
E. coli	*Escherichia coli.*
FP	Fluorescent Protein.
FRET	Fluorescence Resonance Energy Transfer.
GFP	Green Fluorescent Protein
HR	Homologous Recombination
HSF	Heat Shock Factor
HU	HydroxeUrea Drug.
IDP	Intrinsically disordered protein.
KAN	Kanamycin Resistance cassette
LiAc-TE	Lithium Acetate-Tris EDTA.
MCS	Multiple Cloning Site.
MPF	M-phase Promoting Factor
mRNA	Messenger RNA

NA	Numerical Aperture.
NAD	Nicotinamide adenine dinucleotide
NDP	Nucleotide diphospates
ORF	Open Reading Frame
PBS	Phosphate buffered saline
PCR	Polymerase Chain Reaction.
PMT	Photomultiplier
PSF	Point Spread Function
RC	Replication Complex
RNR	Ribonucleotide reductase.
ROI	Region of Interest.
S pombe	*Schizosaccharomyces pombe.*
S. cerevisiae	*Saccharomyces cerevisiae*
SBT	Spectral Bleed Through.
SDS	Sodium Dodecyl Sulfate.
Spd1-	*Spd1* deleted.
Spd1	S-Phase Delayed 1 protein
Spd1+	*Spd1* present.
Suc22	Suppressor of the Cdc22
Ura4	Uracil
UV	Ultra Violet radiation
Wt	Wild Type.
YE	Yeast Extract
YEA	Yeast Extract Agar.
YFP	Yellow Fluorescent Protein.

Chapter 1

Introduction

1.1 *S. pombe*: a model eukaryotic cell

The word *pombe* means *beer* in Swahili, *Schizosaccharomyces pombe (S. pombe*) cells were originally isolated from millet beer in 1893 from Eastern Africa and have also been found in grape juice from southern France and kambucha tea [1-3]. *S. pombe* cells are cylindrical (rod shaped) with a 3-4 µm diameter and grow longitudinally to 7-15 µm in length. They undergo reproduction *via* medial fission, whereby daughter cells of equal sizes are produced by membrane separation at the cell centre, rather than by budding cells. The *S. pombe* cells have three mating types: homothallic h^{90} and heterothallic belonging to two opposite mating h^{-} and h^{+}. Under normal nutrient-rich conditions, the latter propagate in a haploid state throughout the cell lifespan, arrest in the G1 phase and exit the cell cycle when starved of nitrogen. However, if the opposite mating types are available in close proximity, they will form diploids by way of conjugation and immediately enter meiosis and sporulation. The result of sporulation is asci each of which contains four haploid spores and under certain conditions the spores germinate and re-enter the cell cycle. *S. pombe* cells are unicellular fungi having a eukaryotic cell cycle with an extended G2 phase and a short G1 phase [4-5].

Advantages of using *S. pombe* cell as a model for studying DNA damage and repair mechanisms include the ease detection of any mutation and abnormalities exhibited by the cell from the outlook appearance only, the ease with which it can be manipulated in the laboratory [6-8]. It presents a rapid growth with the cell cycle completing within 2.5 to 4 hours, allowing a high sample turn over. It is non-pathogenic and has stable diploid and

haploid states. The easy mating of haploid cells to generate diploids can be exploited to cross previously transformed cells. Simple complementation tests can be performed to compare strains for recessive mutant phenotypes. Importantly *S. pombe* cell can be readily transformed by homologous recombination of exogenous DNA to incorporate engineered mutations into the genome [9-11]. They have been used extensively in research laboratories since their genetic tractability allows detailed analyses of various aspects of a simple unicellular life cycle and additionally, they are very suitable models for the characterisation of genes in more complex eukaryotes and identifying cloned cells [12]. Sub-cellular localization of all *S. pombe* proteins was published in 2006 using green fluorescent protein (GFP) as a molecular tag (a valuable tool for studying the intracellular localization and dynamics of gene products in living cells). Even before the whole genome sequences were published, GFP-fusion libraries had been constructed for several organisms by fusing random fragments of genomic DNA and screened by microscope [11-14].

Recently, in a study made by Yasushi Hiraoka *et al*. [13], large-scale libraries consisting of GFP-fusion constructs were found to be useful for screening proteins based on their intracellular localization. The library has been constructed from chromosomally-tagged green fluorescent protein (GFP) fusions in *S. pombe*. This library consists of 1058 strains. The coding sequence of GFP in each strain is integrated at the 3'-end of a certain chromosomal open reading frame (ORF) such that the full-length construct of GFP fusion is expressed under the control of the original promoter [13]. Verification of the GFP integration of the coding sequence at the authentic chromosomal location of each gene was made by PCR. Interestingly, in 710 strains, sufficient levels of GFP signal were detected by microscopic screening. Localisation of 374 proteins were found in the nucleus, 34 proteins at the nuclear periphery and 65 proteins in the nucleolus, also at the plasma membrane 27 proteins were

detected [13]. Finally, *S. pombe* has also gained an importance in studying the cellular responses to DNA damage and DNA replication.

1.2 The cell cycle

The cell cycle can be described by a series of highly regulated events at which the living cell undergo division. The most distinct phases are DNA synthesis (S phase) and mitosis (M phase) that are separated by gap phases G1 and G2, during which RNA and proteins are constructed [15]. Each phase in the cell cycle has a specific role as shown in Figure 1.1. During G1, the cell grows until it reaches a critical size and DNA is prepared for replication. In S phase, DNA is duplicated. Through G2 phase further cell growth occurs and preparation for cell division. Finally, M phase can be subdivided into four subphases: prophase (condensation of chromosomes), metaphase (chromosomes binding to mitotic spindle and alignment of them on the metaphase plate), anaphase (separation of the two sets of chromosomes) and telophase (nuclear envelope reformation and DNA decondensation [16]. The cell cycle phases are explained with more details below:

M (mitotic): This phase includes two overlapping processes in which initial division of the nucleus (mitosis) occurs followed by division of the cytoplasm (cytokinesis) as seen in Figure 1.1. Condensation of the cell's chromatin into discrete chromosomes signals the beginning of mitosis; each chromosome consists of two joint and identical progeny chromatides at the centromere of the cell. In most organisms the nuclear envelope begins to break apart and the sister chromatids start to move towards the opposite poles under the microtubule action (MT) of the spindle mitotic cell. During this time, division of cytoplasmic

constituents has already started by septation and the nuclear membranes enclose two sets of progeny chromosomes as the division of the cell is completed [17-20].

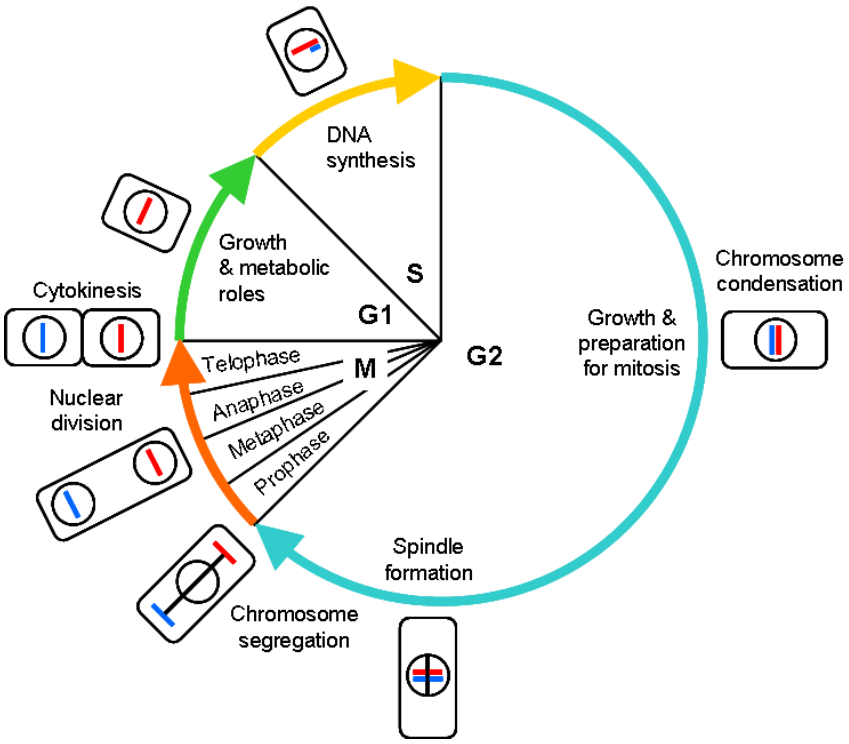

Figure 1.1: Schematic representation of eukaryotic cell cycle, consisting of four phases: G1- the cell grows to a specific size to prepare for DNA replication, S- DNA is replicated and G2 further growth and preparation. These three phases are called interphase. M can be subdivided into four sub phases: prophase, metaphase, anaphase and telophase.

G1 phase is the first gap, during which the cell grows in size and prepares itself for DNA replication. It encompasses the START/ Restriction point (transcriptional factor complex and cyclin-dependent kinase complex), in which the cell constantly monitors the internal and external status of the cell cycle in order to enter S phase and initiate cell division. However, in eukaryotic cells if conditions are limited for progressing into S phase and consequently through the mitotic cycle, the cell will be arrested in the stationary phase (G0

phase) until the conditions of the cell become satisfactory to re-enter the mitotic cell cycle [17-21].

S phase is the most complex and highly regulated phase of the cell cycle during which DNA replication and synthesis occurs. Through this phase, the entire genome of the cell replicates, demanding a huge number of proteins, a large amount of energy (for production of deoxynucleoside triphosphates (dNTPs)) and efficient timing to assemble the genetic code. Upon entry into S phase, DNA is replicated simultaneously at multiple replication origins, defined by specific sequence at different locations in the genome. The initiator protein (a helicase at each origin) unwinds the DNA slightly and synthesis of new strands forms a replication fork that allows the single-stranded DNA replication machinery to begin, including polymerase and ligase. Once replication of DNA is started, it commonly carries on in a bidirectional way. The replication forks are at the ends of a "replication bubble" that grows as replication continues in both directions from different origins. Each origin results in a replicon and a large number of origins results in a large number of replicons, in eukaryotic cells. During S phase, not all the replicons are initiated at the same time but all must be completed before entry to M phase. In S phase, after separation of the DNA strands, bases are exposed and therefore become sensitive to external agents including drugs and mutagens. Any error at this level can be catastrophic and fatal, so the synthesis must be completed rapidly with the highest possible fidelity [15-16].

G2 phase follows the completion of DNA replication and is the second gap phase in the cell cycle. G2 phase provides a safety network to ensure completion of the DNA replication process before starting mitosis. Many re-organisational and synthesis events take place in this phase including the start of chromatin condensation that paves the way to mitosis.

The G1 and G2 phases provide the cell with adequate time to grow and develop and at the same time screen out its suitability for further rounds of cell division and DNA replication. Thus, these phases provide a period in which genetic identity and integrity of the cell are maintained for the ensuing generations of offspring.

1.3 Ribonucleotide reductase (RNR) and dNTP regulation.

The survival of all cells depends on the ability of DNA to replicate and repair faithfully, which requires adequate and balanced pools of deoxyribonucleoside triphosphates (dNTPs) (the building blocks for DNA synthesis) that are maintained primarily through the regulation of ribonucleotide reductase (RNR).

There are three classes of RNR enzymes which employ different mechanisms for the generation of the protein radical, the first step in the reduction of nucleotide diphosphates (NDPs) by the active complex [22-28]. Class I reductases consist of two subgroups Ia (α_2) and Ib (β_2). These subgroups are differentiated by their primary structures, both comprised of two dimeric subunits (R1 and R2) see Figure 1.2. Class II reductase has a simpler formation (α or α_2) [26-27]. Class III reductases are $\alpha_2\beta_2$ heterotetramers, similar to class I [28].

In class I, the large subunit is R1 (α-protein) that contains the active site, binding NDPs in a site with three cysteine residues and a glutamate residue and a binding site for allosteric effectors. The cysteines residues are positioned at the C-terminal part of R1, whereas the effectors or ATP cone is located at the N-terminal [26,29,38,40]. R2 (β-protein) is the small subunit that is responsible for generating a tyrosyl free radical, which is ultimately transferred to the active site of R1 for NDP reduction.

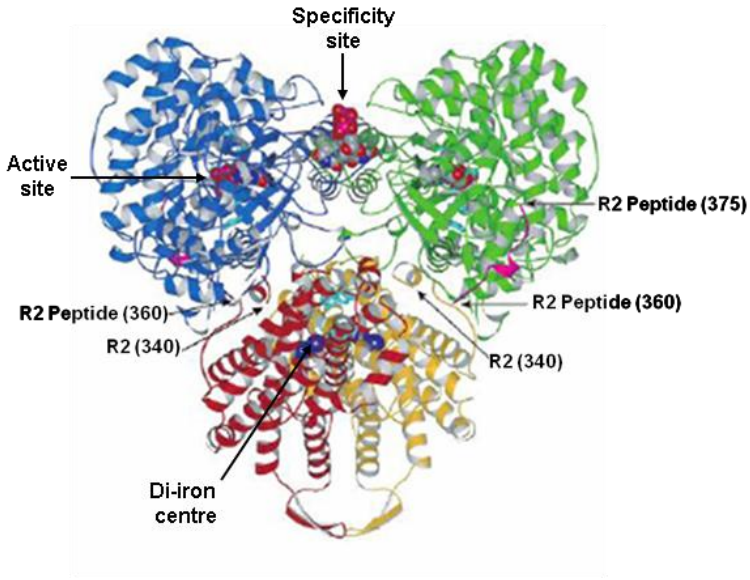

Figure 1.2: Crystal structure of RNR subunits: R1 and R2. The large subunit contains the active site and the binding site [28].

For eukaryotic cells, the classical RNR enzyme is class I. In vitro, both, R1 and R2 subunits [27] form a heterotetrameric ($\alpha_2\beta_2$) RNR complex (Figures 1.2). Rofougaran *et al.* [113] reported in vitro that R1 can be induced to form a hexamers (α_6) in both *E.coli* and mouse and can associate with the R2 dimer (β_2) subunit to form an octameric complex ($\alpha_2\beta_2$). The R1 subunit is about 90 kDa in size and is the "business end" of the enzyme as it contains the binding sites for the ribonucleotide substrate and allosteric effectors [29]. R2 is about 45 kDa and contains a binuclear ferric iron centre (Fe-O-Fe center) which participates in catalysis by generating and maintaining a tyrosyl radical cation (Tyr.) [29-32]. Tyr is positioned at a distance 10 nm inside the structure, and therefore there is no possibility to interact directly with R1. The distance between the tyrosyl radical site of R2 and the thiol radical site of R1 is about 35 nm, a network of residues in both proteins providing a pathway for electron transfer to the active site of R1. The R1 and R2 subunits together form the active sites of the enzyme as demonstrated in Figure 1.3a [33]. Both R1 and R2 subunits need to

dimerize to be activated [33-35], but the binding of monomers is weak and can easily dissociate during purification. Overall enzymatic activity is controlled by an effector (active binding effector). When the effector binds adenosine triphosphate (ATP) this acts as an activator by stimulating enzymatic reduction of NDPs. However, binding deoxyadenosine triphosphate (dATP) in the binding effector acts to inhibit RNR activity and will moderate the general level of the dNTP pools [27, 36-37].

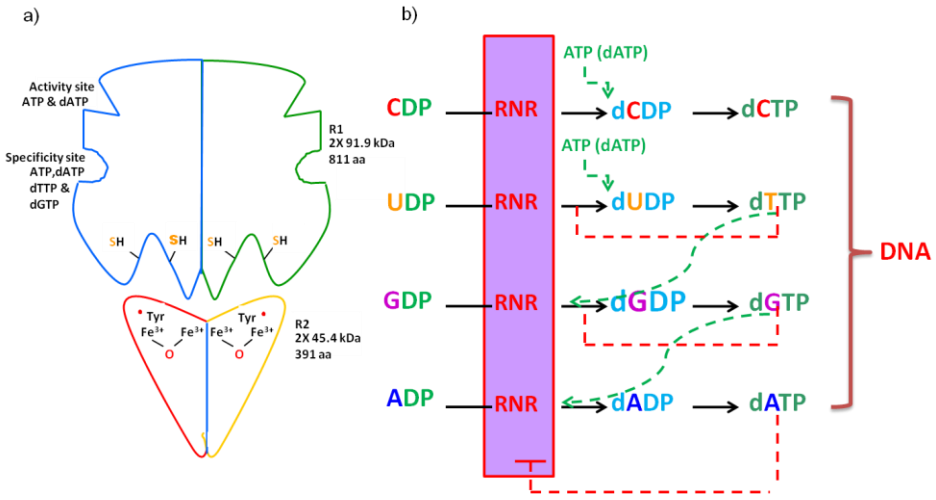

Figure 1.3:a) The schematic of RNR subunits. b) *De novo* biosynthesis of dNTPs with relative negative feedback [reproduced from Ref. [37]

A specificity site dictates the substrate that is reduced. This site binds ATP, dATP and also the products of uridine diphosphate and guanine diphosphate reduction and subsequent phosphorylation, dTTP and dGTP respectively. Ultimately this specificity allows equilibrium of the four nucleotides and a correct and balanced pool of dNTPs can be achieved throughout a multifaceted feedback mechanism, in a *de novo* biosynthesis schematised in Figure 1.3b. In brief, if cellular ATP levels are high it competes for both activity and specificity sites and activates NDP reduction. In this case both CDP and UDP are reduced and following phosphorylation the pool of dTTP and dCTP increases. When dTTP competes for the

specificity site, RNR promotes reduction of GDP and ultimately dGTP levels rise. dGTP binding the specificity site then stimulates the RNR to reduce ADP to make dATP, this in order to balance levels on dCTP [37-38] as dATP levels raise it competes with ATP in the overall activity site and ultimately shuts down RNR activity.

In *S pombe*, RNR consists of the large R1 catalytic subunit Cdc22 located in the cytoplasm and the small R2 regulatory subunit Suc22 in the nucleoplasm. The context map for genes encoding for Suc22 and Cdc22 and some of their physical properties are shown in Figure 1.4a and 1.4b respectively below [39].

a

Location at chromosome 2

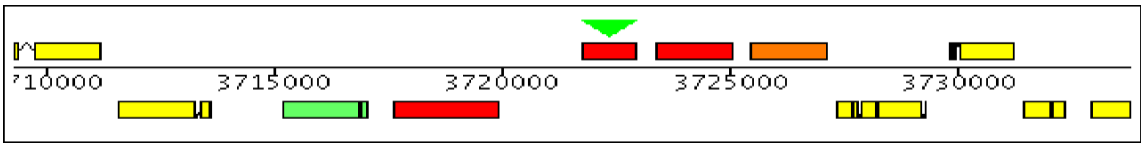

Mass	45.4 kDa	Amino acids	391
Isoelectic point	pH 4.6	Charge	-20.0

b

Location at chromosome 1

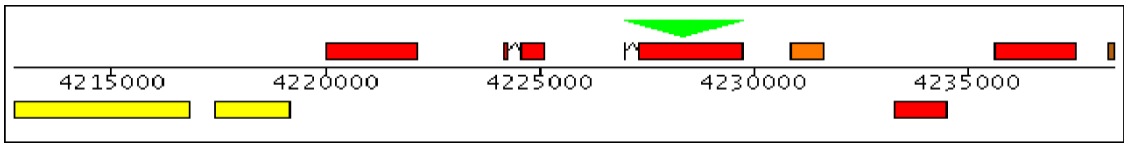

Mass	91.9 kDa	Amino acids	811
Isoelectic point	pH 6.4	Charge	-0.5

Figure 1.4: Context map and physical properties for the two protein subunits studied a) Suc22 and b) Cdc22 [39].

1.3.1 RNR chemistry: the nucleotide reduction pathway

As mentioned before R1 contains the catalytic site with the active dithiols which are essential for reduction process schematized in this reaction. Three cysteines (Cys) are formed in the mechanism of active site of R1, the first one is the initial thiyl-radical carrier which is essential in the reaction and the other two cysteines are responsible for providing reducing equivalents and they are directly involved in the reaction. During catalysis, the radical is transferred to a cysteine residue of the active site, where it is obligatory for catalysis [24, 29, 41]. Any chemical agent like HU can be used as antiproliferative drugs to destroy the free radical [30, 34].

Ribonucleotide reductase (RNR) enzyme catalyzes the biosynthesis of dNTPs by converting RNA precursors to DNA precursors by substituting the 2_OH group of a ribonucleotide with a hydrogen atom by a mechanism involving protein radicals after intricate oxidation-reduction reaction involving cofactors (Figure 1.5) [30,33,42]. Failure to regulate the pools of dNTP correctly can cause misincorporation of nucleotides into DNA, leading to genetic abnormalities and cell death [34]. Two different pathways are known for *E.coli* RNR: the first one uses thioredoxin, while the second uses glutaredoxin. However, in both cases NADPH is reduced. The mechanism of reduction process is explained below:

The reaction starts when an electron transfer occurs from a cysteine residue on R1 to the tyrosyl radical on R2. The loss of an electron creates a highly reactive cysteine thiyl radical within the active site of R1 which then capture hydrogen atom from C-3′ of the ribose unit, generating a radical at the third position carbon atom. This radical then stimulates the release of the hydroxide ion on the carbon-2 atom. The second residue of cysteine protonates the hydroxide ion to leave as a water molecule. A hydride ion is then transferred from a third cysteine residue to complete the reduction process of the C-2′ position, produces a disulfide

bond, and reproduces a C-3′ radical which then resubtracts the same hydrogen atom originally captured by the first cysteine residue, and the deoxynucleotide is free to leave the enzyme. The disulfide bond generated in the enzyme's active site is then reduced by specific disulfide-containing proteins, such as thioredoxin or glutaredoxin, to regenerate the active enzyme and starts a new cycle of production. To finish the overall reaction, the oxidized thioredoxin generated by this process is reduced by NADH in a reaction catalyzed by thioredoxin reductase [43].

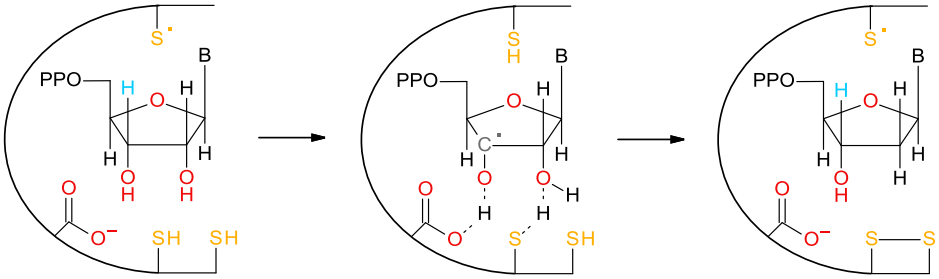

Figure 1.5: Chemical mechanism of nucleotide reduction by ribonucleotide reductase (RNR)**.**

1.3.2 Regulation of RNR in the cell cycle

The regulation of RNR activity involves cell cycle specific expression and degradation of the RNR proteins, as well as binding of allosteric effectors to the large RNR subunit [33]. In *S. pombe* as in budding and mammals, RNR activity is tightly controlled *via* transcription, specific protein inhibition and by subcellular localization of its two subunits, R1 and R2 (Figure 1.6).

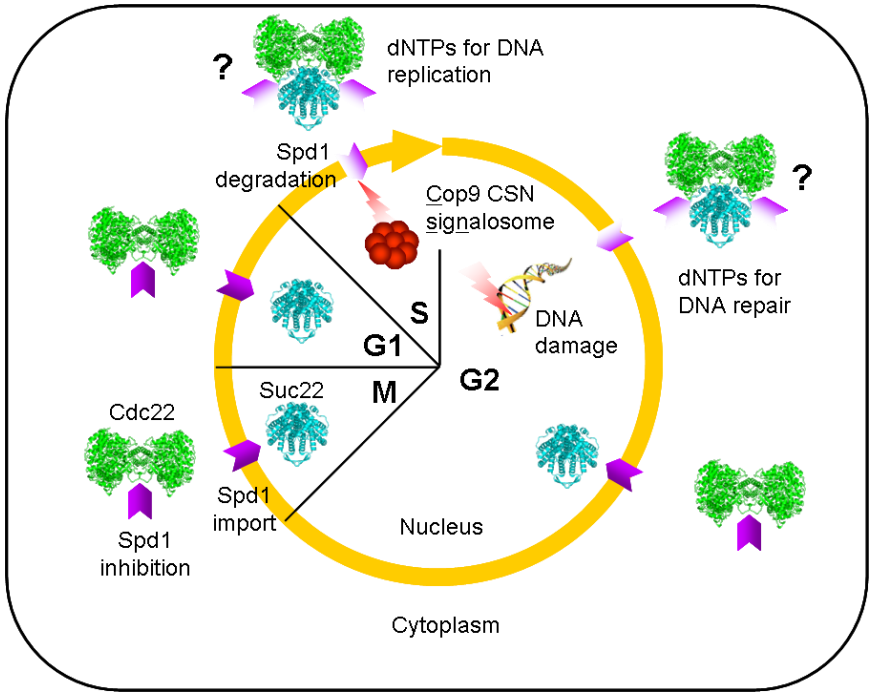

Figure 1.6: The simplified diagram of *S.pombe* cell cycle and its RNR in the current model. It explains the regulation of RNR in the cell cycle . Formatiom of RNR active complex for production of dNTPs that are required for DNA replication and repair *via* Spd1 degradation during S and G2 phase (DNA damage). Whilest, during G2, M and G1 phase, Spd1 inhibiting RNR by improting Suc22 into nucleus and binding Cdc22 into the cytoplasm

In the fission yeast, the transcription of R1, Cdc22, reaches its maximum levels on the G1/S boundary and maintains the maximum level during the S phase. However, the lowest level is observed in middle G2 phase [44]. While, the transcription of, Succ22 is encoded by two alternative transcripts [45]. The smaller of these transcripts is constantly expressed at high levels regardless of the phase of the cell cycle [46]. While Expression of the large transcript is periodic during the cell cycle and reaches its maximum at G1/S boundary coincident with the peak of R1 [46, 47]. Both transcripts of the two subunits R1 and R2 are induced following DNA damage [33, 45, 47].

RNR is highly regulated in the cell cycle *via* degradation of its inhibitor, Spd1, by the signalosome (known as COP9 constitutive photomorphogenesis or CSN) that is activated during unperturbed S-phase or following DNA damage [49]. It has been suggested that Spd1 anchors the small subunit (Suc22) of RNR into the nucleus, whereas binding the large subunit (Cdc22) in the cytoplasm. However after degradation of Spd1, the small subunit delocalizes from the nucleus to the cytoplasm to form an active RNR complex which leads ultimately to biosynthesis of dNTPs that are essential for DNA replication or repair (Figure 1.6). The degradation of Spd1 correlates with the nuclear export of the small RNR subunit Suc22 into the cytoplasm. When in the cytoplasm, Suc22 presumably forms an active complex with the cytoplasmic RNR large subunit Cdc22 [58]

Spd1 degradation is promoted by two separate signalosome-dependent mechanisms. During unperturbed S phase, Spd1 degradation is independent of checkpoint signalling pathways. But following DNA damage Spd1 degradation becomes dependent of checkpoint protein of DNA damage. Checkpoint signalling pathways induce the cell cycle to arrest in response to DNA damage. Indeed, some checkpoint proteins may participate directly in DNA repair events. Checkpoint signalling monitors the state of the genome prior to DNA replication (G1/S) and chromosome segregation (G2/M) and are essential in maintaining genome integrity.

1.3.3. DNA damage & replication checkpoint pathways.

Checkpoints are essential to maintain the completion of the cell cycle in the correct manner and avoid genetic and physiological abnormalities. In general; eukaryotic cells have three cell-cycle checkpoints at: G1/S transition, G2/M transition and the mitosis checkpoints during the metaphase/anaphase transition [27]. Before initiating S phase, a G1 yeast cell

makes sure it has got enough nutrients; if not, the cell stays in G1. At the same time, if mating pheromones are there, the cell may commence sexual differentiation instead of executing a mitotic cycle. Additionally, a small G1 yeast cell must remain in G1 until it grows to a specific size. If the cell is too small, the G2/M checkpoint delays entry into mitosis. Another mechanism working at the G2/M checkpoint ensures that mitosis is delayed if DNA is incompletely replicated or damaged. The third checkpoint ensures that the sister chromatide segregation (anaphase) does not take place before all the chromosomes are accurately aligned on the mitotic spindle (metaphase). These checkpoints block succession through the cell cycle by interfering with the cell cycle network engine, i.e. with the interactions that activate or inactivate M phase promoting factor (MPF) complex.

In the case of DNA damage and before starting the mechanism of DNA repair, the damaged point should be identified first by the checkpoint pathways. Then, checkpoint pathways are activated by arresting the cell cycle which allows adequate time for maintenance activities to take place before the next cell cycle phase starts. The DNA integrity checkpoint pathways occur at the G1/S, G2/M boundaries and during S phase. Without checkpoint systems, uncorrected problems can arise and pass; for example during S phase unreplicated DNA go uncorrected and produce catastrophic chromosome segregation after mitosis [68-69]. A checkpoint pathway can be defined as a signal transduction system that passes information from the DNA to the machinery of the cell cycle. To achieve these transmissions, sensors, mediators, transducers and effectors are needed. Sensors are responsible for detecting DNA lesions and activating transducer proteins which are central to the DNA damage response (since they are able to transmit DNA lesion signals from the sensor proteins to the effectors proteins). Once the effectors have been triggered, they perform the proper DNA damage response [68-69].

The response of the checkpoint pathways varies according to the type of challenge and the cell cycle phase and different types of conserved kinases are involved in the mechanism. For example, checkpoint proteins interact either with the replication complex (RC) during S phase or with the strand breaks of DNA during G2 phase. Different checkpoint pathways involve different types of conserved checkpoint proteins and kineases including the Ataxia Telangiectasia and Rad3-related (ATR)/ATR interacting protein (ATRIP) kinease complex, the RFC and PCNA-like complexes (Rad1, Rad9, Hus1 and Rad17), the mediator proteins (Crb and Mrc) and the effectors kineases (Chk1 and Cds1) [69].

In fission yeast, a large protein kinase of DNA-PK family is Rad3 which plays a major role in the checkpoint pathways. The other important kinase is ATR-ATRIP complex which is Rad3/Rad26 in fission yeast. This complex is responsible for phosphorylation many other checkpoint proteins. The phosphorylation of Rad3-dependent Chk1 and Cds1 is central to checkpoint activation. Several mediator complexes act in S and G2 phase. For example Mrc1 mediate Cds1-dependent checkpoint signalling during S phase. Activation of Cds1 kinase produces accumulation of Mik1 which phosphorylates Tyr15 residue of Cdc2, whereby, preventing mitosis. Mrc1/ Cds1 plays additional roles in S phase response as stabilizing stalled replication forks and inhibiting late firing replication origins. The mediator Crb2 mediates Chk1-dependent checkpoint signaling and activation of Chk1 produces in activation of Mik1 and Wee1 Cdc2 Tyr 15 kinases and this may inactive Cdc25 tyrosine phosphate. In G2 phase, Chk1 is also involving in controlling dNTPs synthesis and its activation induces degradation of small protein in fission yeast Spd1 protein [69].

1.3.4 Signalosome COP9-Pcu4-Ddb1 complex and RNR regulation

The signalosom (CSN) is a complex of conserved proteins and is comprised of eight subunits called csn1 to csn8. All are conserved in the human genome and other eukaryotes. In gel filtration columns, CSN fractionates as a 450–550 kDa complex [50]. CSN was initially identified as a negative regulator (repressor) of photo-morphogenesis in plants [51]. CSN is implicated in a wide variety of regulatory processes including cell cycle control, signal transduction, transcriptional activation, and plant photomorphogenesis. Recently, CSN complex has been identified in the *Saccharomyces cerevisiae,* as a quite divergent complex [52]

A simple version of a conserved signalosome complex was identified in the fission yeast [49] and that consists of six subunits. The two subunits csn6 and csn8 have not been reported in *S. pombe* [53]. Although the biochemical function of CSN is not yet completely known, it has been found that the signalosome is involved in regulating cullin-dependent ubiquitin ligase and protein kinase activities which are capable of phosphorylating important signalling regulators. The involvement of CSN in a number of cellular and developmental processes has been attributed to its control over ubiquitin-proteasome-mediated protein degradation. Ubiquitin is an important protein responsible for the turnover of most short-lived proteins [54,140]. The ubiquitin system selectively recognizes proteins by covalently binding to target lysines which in turn may be regulated for example by phosphorylation or allosteric interactions [141].

Outside S phase, CSN is inactive and Spd1 is not degraded thereby inhibiting RNR activity and thus Suc22 inside the nucleus. Activation of RNR by CSN *via* an intermediate stage of cullin-dependent ubiquitin ligase (Pcu4) of which leads to degradation of Spd1 resulting in

exportation of the small RNR subunit from the nucleus to the cytoplasm. The process correlates with a requirement for DNA replication and repair.

Nestoras group [63] showed that two signalosome subunits, csn1 and csn2, are essential to regulate ribonucleotide reductase (RNR) by regulating ubiquitin ligase through the degradation of the small protein Spd1 in order to produce dNTPs. However, deletion of csn1 and csn2 mutants, Spd1 is not destroyed and accumulated to high level that repress Suc22 function, probably by preventing delocalization of Suc22 from the nucleus to the cytoplasm. Additionally, csn1 and csn2 are required for DNA replication and responsible also for normal resistance to DNA damaging agent [53-55].

Ddb1/Pcu4/COP9 complex represent a key pathway controlling genome stability, repair, and differentiation *via* RNR regulation. In irradiated G2 cell, the degradation of Spd1 is promoted by checkpoint proteins Rad3 and chk1 dependent DNA damage in addition to signalosome copurifies with Pcu4/ cullin-4 homologue (association Pcu4-Ddb1-COP9). Pcu4, csn1, and csn2, explore a new role for the signalosome as a regulator of Pcu4-containing E3 ubiquitin ligase (plays a role in gene expression and DNA replication by targeting the degraded proteins) [55-56]. Transactivation of *S. pombe* cdt2+stimulates a Pcu4-Ddb1-CSN ubiquitin ligase [57].

Ddb1, associates with cullin 4 ubiquitin ligases and COP9 has a great role in S phase progression and also required for degradation of the ribonucleotide reductase (RNR) inhibitor protein Spd1. Christian Holmberg *et al* [58] showed that Ddb1 becomes essential when cells differentiate into meiosis and a mutant *S. pombe* strain lacking expression of the *ddb1*gene exhibited slow replication causing a delay S phase [58-60]. Furthermore, it has been demonstrated that the loss of Ddb1 protein is synthetically lethal with loss of *rad3* and some other DNA damage checkpoint genes and that these colethalities are restrained by *spd1::ura4+*

1.3.5 S-phase delay protein (Spd1) and its role in RNR activity

S-Phase Delayed 1 (*spd1*) is a gene of 375 bp situated on the chromosome 1 in *S. pombe.* During a screen for new *S. pombe* genes for cell cycle arrest *spd1* was found. When this small protein was overexpressed [55, 61] it causes S phase delay. Limited structural information and properties of *spd1* are demonstrated below in Figure 1.7:

a

Location chromosome 1:

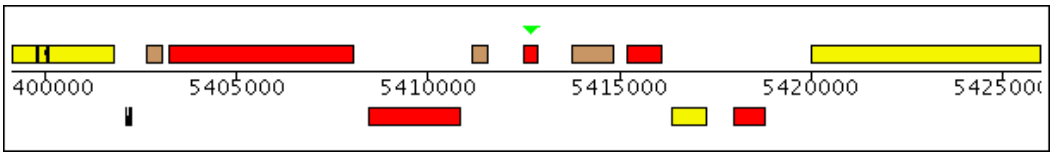

B

Mass	14.2 kDa	Amino acids	124
Isoelectric point	pH 7.6	Charge	1.0

Figure 1.7: a) location of *spd1* gene on the chromosome one of *S pombe* cell. b) Physical properties of *Spd1*.

Spd1 has proposed domains, found in the sequence-conserved *S. cerevisae* orthologues: Sml1, Dif1, and Hug1. Dif1 promotes R2 nuclear import. During S phase or genotoxic stress Dif1 is degraded will reduce the nuclear import and activate the nuclear export of R2 in the cytoplasm [62]. Spd1 in *S. pombe*, and Dif1 in *S. cerevisiae* found to regulate nuclear localisation. The HUG domain is conserved between Spd1 and Dif1, through which Dif1

binds R2 to promote R2 nuclear import. [62, 63] The role of Hug1 is not fully understood, however, its transcript is induced by DNA damage and it has been suggested to control RNR inhibition [64, 65]. Spd1 shares the last half of Sm1 domain, R1 binding as shown in Figure 1.8 [62, 63, 66], the function of this domain is well known as RNR inhibitor and that is consistent with Spd1 and Cdc22 association. Due to the above, it has been proposed that Spd1 may be the sole *S. pombe* ortholog of an ancestral gene.

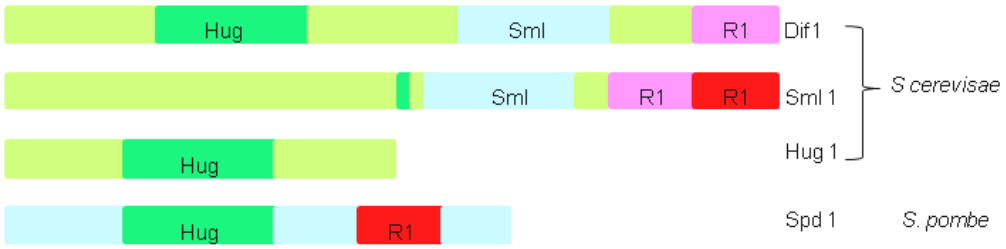

Figure 1.8: Cartoon representation of relationship to *S. cerevisiae* Dif1, Sml1 and Hug1 in a comparison to Spd1 domains in S. pombe. Spd1 in *S. pombe* and Dif1 in *S. cerevisiae* regulate R2 nuclear localization. The HUG domain is conserved between Spd1 and Dif1. Dif1 binds R2 via the HUG domain to facilitate R2 nuclear import. Spd1 also shares a region of sequence similarity with Sml1, equating to the last half of the suggested Sml1 RNR1-bindingdomain. The sequence conservation between Spd1, Dif1, Sml1, and Hug1 indicates that Spd1 may be the sole *S. pombe* ortholog of the ancestral gene [63].

The role of Spd1 in the regulation of RNR is not wholly understood in *S. pombe* cells, it has been thought to regulate RNR activity. Using in vitro assays with purified recombinant proteins, it has been demonstrated that Spd1 is indeed a very efficient inhibitor of fission yeast RNR, by binding to Cdc22 as well as act as an anchor factor for Suc22. Furthermore, bioassay techniques showed that Spd1 protein binds to the Cdc22 with a K_D of 2.4 µM while the affinity to Suc22 is negligible. Therefore, Spd1 inhibits fission yeast RNR activity by interacting with the Cdc22 [57-58]. When cells enter the S-phase, signalosome (CSN) is

activated to increase the supply of deoxynucleotides during DNA replication or repair and that leads transportation of Suc22 to the cytoplasm, where it forms active complexes with Cdc22. Spd1 degradation correlates with the nuclear export of the small RNR subunit and dNTPs level, which in turn, correlates with a requirement for RNR in replication and repair [67].

Using indirect immunofluorescence microscopy, Liu *et al.* observed that Spd1 responsible for nuclear co-localization of Suc22 [58, 68]. Although no direct evidence was obtained for protein-protein interaction, such an interaction was proposed in the model for the regulation of fission yeast RNR activity during S phase and DNA repair. To increase the supply of deoxynucleotides during DNA replication or repair, Spd1 is degraded by the Cop9/Pcu4/ Ddb1 pathway [57, 63 and 69] and this leads to a depletion of the Suc22 from the nucleus to the cytoplasm where it interacts with Cdc22 to form active RNR complex [58].

Recently, it has shown by Nestoras group [63] that Spd1 seems also to play a role as a nuclear importer rather than Suc22 nuclear anchoring factor. The deletion of Spd1 in *S. pombe* results in a delocalization of Suc22 from the nucleus to the cytoplasm, giving a typical Suc22 pan-cellular phenotype under the microscope. Experiments with a nuclear export blocking agent (Leptomycin B, LBM (100 ng/mL) which inhibits Crm1-dependent nuclear export of Suc22) followed treatment of *spd1*-deleted cells, Suc22-CFP, with HU (20 mM) to arrest the cells in S phase. The result showed no nuclear accumulation of Suc22 in response to LBM treatment. Additionally to examine whether Spd1 acts as a canonical Suc22 nuclear anchor, another experiment was performed for a nucleolus C-terminal signal to *spd1* locus to force *spd1* localisation in the nucleolus and if this occurs then there would be a concomitant nucleolar Suc22. Data showed no accumulation of Suc22 to the nucleolus. All these information indicate that Spd1, which binds to Suc22, is involved in its nuclear importation [63].

Furthermore, Nestoras *et.al* has created 41 independent mutants of *spd1* labelled from *spd1-m1- spd1-m41* by alanine mutagenesis. To elucidate the role of Spd1 in the nuclear accumulation of Suc22, Nestoras *et al.* crossed each *spd1* mutant into the Suc22-*GFP* background and observed Suc22 localisation by direct fluorescence in untreated cells and cells treated with 20 mM HU for 4 hours. In the presence of Spd1, Suc22 was largely nuclear (reflecting the fact that most asynchronous *S. pombe* cells are in G2. Following treatment with HU, cells arrested in S phase with Spd1 degraded and Suc22 became pan-cellular in approximately 80% of cells with only 20% of cells showing modest nuclear GFP fluorescence. A number of the *spd1* mutants were defective in Suc22 localisation, including complete loss of nuclear localisation (as seen in *spd1-m2, spd1-m14 and spd1-m26*). Three mutants, *spd1-m12, spd1-m13* and *spd1-m33* displayed weak localisation in G2 cells and this was completely lost upon HU treatment. Finally, four mutants, *spd1-m22, spd1m-38, spd1-m40* and *spd1-m41* showed strong localisation slowly reversed by treatment of HU. No mutant showed a complete failure to delocalise Suc22 to the cytoplasm, unlike the Spd1 deleted strain.

It has been tested Spd1-dependent inhibition of RNR by two independent assays [63]. As mentioned before, the degradation of Spd1 is promoted by the COP9-Pcu4-Ddb1 complex in addition to Rad3 and chk1 dependent DNA damage and the loss of Ddb1protein is synthetically lethal with loss of *rad3* and these colethalities are restrained by Spd1 [47, 58, 60]. Depending on this, the first assay performed by the group to show the ability of *spd1-* mutants to rescue the synthetic lethality by the signalosome component *csn1* and the checkpoint gene *rad3* checkpoint gene [63]. Essentially, in *csn1* mutants, Spd1 is stable and thus RNR inhibited, only mutants (*spd1-m10, spd1-m11, spd1-m13, spd1-m14, spd1-m15,*

spd1-m16, spd1-m17, spd1-m18, spd1-m19 and spd1-m26) have rescued *rad3 csn1* synthetic lethality with the approaching of efficiency that of the Spd1 deleted [63].

In a second assay, it has been showed that the ability of *spd1*deleted to rescue the spore formation defect evident in the Ddb1- deleted (*ddb1-)* background [63]. Again RNR is inhibited by Spd1 in *ddb1-* mutants that lead them not to progress through meiotic to S phase and unable to form spores [47, 58, 60, 63] The phenotype is reversed by either deleting *Spd1* or over-expressing Suc22. Then they combined each mutant with *ddb1-* and scored the percentage of asci (formation of four spores resulted from the crossing) with 0,1,2,3 or 4 spores. The result of spore formation was restored in mutants: *spd1-m3, spd1-m11* through *spd1-m16, spd1-m18, spd1-m26, spd1-m30, spd1-m34* through *spd1-m38, spd1-m41*.
Therefore, we conclude from these two assays that both growth of the cells the recovery of spore formation are correlated with loss of the inhibitory function of Spd1.

According to the *spd1* sequence, HUG domain (amino acids 30-62) is represented by in the region of *spd1-m10* to *spd1-m19.* Mutation this region showed mainly defect in nuclear localisation and unable to restraint RNR activity. Importantly, the nuclear relocalisation function does not correlate with RNR restraint activity. The R1 binding region (amino acid 83-97) is represented by *spd1-m28* to *spd1-m32* which showed that Spd1 able to restrain RNR activity [70] and showed lack in nuclear localisation. The region which includes *spd1-m1* to *spd1-m10* showed high ability to restrain RNR activity and lack in nuclear import function. The region which represents *spd1-m33* to *spd1-m41* except *spd1-m34* and *spd1-m41* showed keeps the ability to restrain the RNR activity and mainly keep nuclear localisation.

The Spd1 structure can play a great role in its function. Nuclear Magnetic Resonance (NMR) analysis [63] and structural genomic data showed that Spd1 is an intrinsically disordered protein (IDP) [69]. Programs for structural prediction such as DrDOS which predicts a high probability of disorder for Spd1, also shows the protein to potentially form

ordered coils with two regions [61]. Most consistent are the two helical regions between residues 27–44 and 66–76, in addition to the possibility of shorter extended structures between 6–10 and 115–120. The graphic web server FoldIndex© describes a facile method of predicting for a given protein sequence, whether it is intrinsically unfolded by implementing the algorithm of Uversky and co-workers based on the average residue hydrophobicity and net charge of the sequence [69]. The folded (structured) region *vs.* unfolded region of Spd1, Cdc22 and Suc22 as predicted by FoldIndex© shown in Figure 1.9:

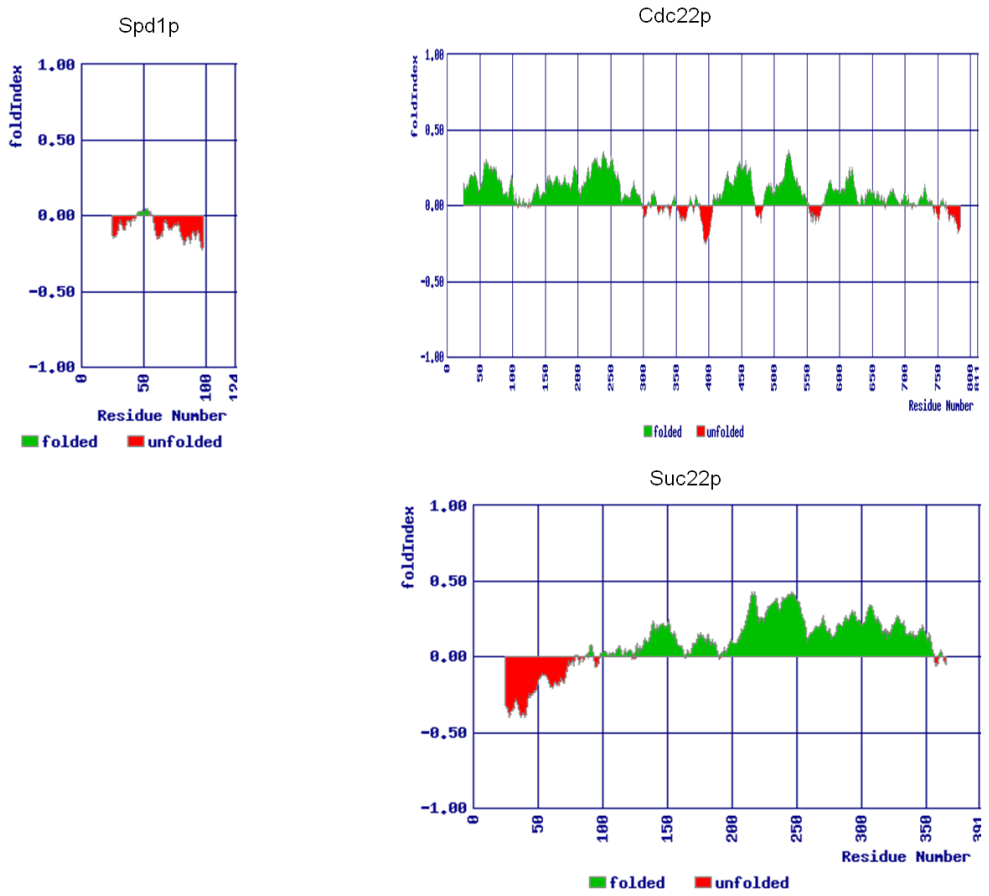

Figure 1.9: FoldIndex plotted for three protein sequences Spd1, Suc22 and Cdc22. The green regions refer to the well-folded (structured) regions while the red regions refer to the unstructured or unfolded regions within the protein [19, 69 and 71].

NMR studies reported that in solution IDPs can adopt transient arrangement and some IDPs can fold on their interaction partner when they associate. This process can be resulted from protein-protein interaction with high specificity and low affinity. According to that Spd1 can bind multiple substrates with high specificity but low affinity which reflects that Spd1 can interact with both Cdc22 and Suc22 subunit.

Overall experimental evidence suggests that Spd1 plays an intricate role in the regulation of RNR. Therefore, to investigate the function of Spd1 as an RNR inhibitor and whether it mediates the interaction of R1-R1 subunits, we have performed fluorescence energy transfer (FRET) experiments using confocal laser scanning microscopy (CLSM).

1.4 FRET: a spectroscopic reporter of protein-protein interactions

A number of spectroscopic tools can be applied to CLSM, including fluorescence fluctuation spectroscopy (FCS), fluorescence recovery after photobleaching (FRAP) and other derivatives of these techniques. A powerful tool for investigating intermolecular interactions is fluorescence (or Förster) resonance energy transfer (FRET), a process that involves the radiationless transfer of energy between two molecules, a donor and acceptor fluorophore. Generally, FRET provides information about distance between molecules which are tagged to two appropriate donor and acceptor molecules. In our project Cyan (CFP) and Yellow (YFP) has been used as a donor and an acceptor respectively. Three conditions are required for FRET to occur: firstly the emission spectrum of a donor overlaps (>30%) with the absorption spectrum of an acceptor (Figure 1.10). Secondly, the distance separating the donor and acceptor fluorophores is limited to between 1-10 nm, because the efficiency of energy transfer varies strongly as the inverse of the sixth power of the distance over which FRET can

occur. The range of distance is limited by the characteristic distance R_0 at which 50% energy transfer occurs [177-178]. Finally, the donor and acceptor fluorophore dipoles should be in a favourable mutual orientation.

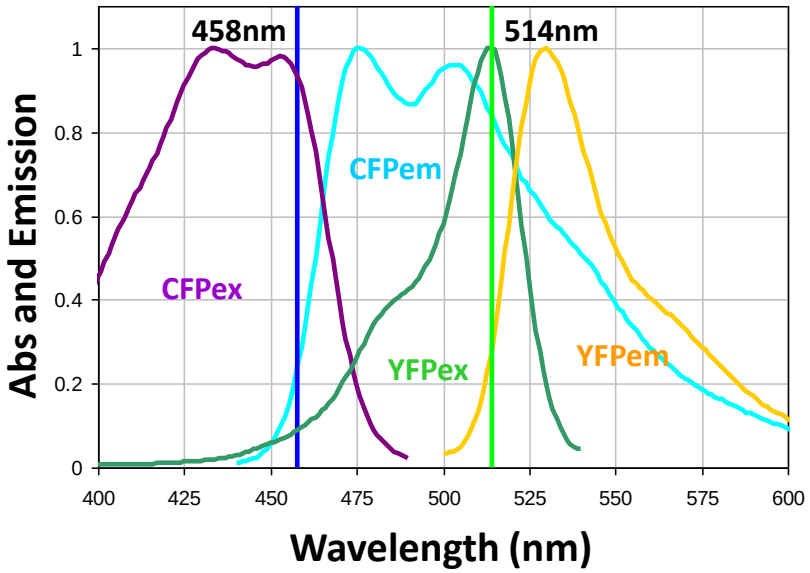

Figure 1.10: CFP-YFP absorption and emission spectra with their absorption peaks at 458 nm(blue line) and 514 nm (light green) respectively. The region between cyan and green curves represent the spectral overlap region between the donor emission and the acceptor absorption. This spectral overlap is important for efficient FRET because it increases the rate of donor that can transfer energy to the acceptor.

When the spectral, dipole orientation, and distance criteria are satisfied, illumination of the donor fluorophore results in sensitized fluorescence emission from the acceptor, indicating in our case that the tagged proteins are separated by <10 nm [72-75]. In the fluorescence cycle a photon from the laser excites the donor from a ground state S_0 to an excited state S_1. Vibrational relaxation in the excited state "slows" the oscillation of the donor transition dipole that would normally lead to the red shifted emission. In the presence of an acceptor molecule with a transition dipole frequency at that of the emitting donor, the

acceptor dipole is induced to oscillate in resonance with the donor, causing excitation of the acceptor and subsequent emission.

The relationship between the energy transfer efficiency (E) and the distance between donor and acceptor molecule, r, is quantitatively defined by the following Equation [74-75].

$$E = \left[1 + \left(r / R_0\right)^6\right]^{-1} \qquad 1.1$$

where R_0 is the distance between the donor and acceptor at which half the excitation energy of the donor is transferred to the acceptor while the other half is dissipated by all other processes. The functional form of this expression for the FRET efficiency is plotted in Figure 1.11 which clearly shows the sensitivity of the extent of energy transfer with small changes in distance.

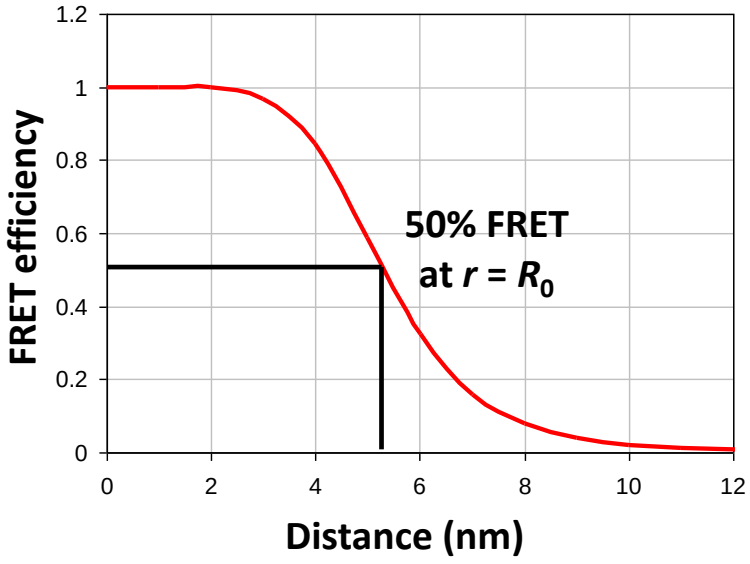

Figure 1.11 FRET efficiency dependency on donor and acceptor separation calculated in nanometres. The FRET efficiency decays as 1/6 with the distance which means the efficiency is so sensitive to any small change in the distance.

The energy transfer efficiency in terms of the intensity of the donor in the presence of accepter, I_{DA}, and the intensity of the donor in the absence of the acceptor, I_D can be given by

$$E = 1 - \left(I_{DA} \Big/ I_D \right) \qquad 1.2$$

where I_{DA} is the measured intensity of the donor fluorescence in the presence of the acceptor, I_D is the intensity of the donor in the absence of the acceptor and in order to measure it alone the acceptor must be removed in some manner. In general photobleaching of the acceptor results in a large shift in its absorption wavelength and hence overlap with the donor fluorescence. In this case no FRET occurs and the measured donor intensity is simply I_D.

In the experiments presented here we employ this method of FRET measurement by acceptor photobleaching to determine the extent of the RNR subunit interactions in the *S .pombe* cell (Figure1.12). As mentioned above one of the most important conditions for FRET to occur is the overlap of the emission spectrum of the donor with the absorption spectrum of the acceptor. However, as a result of spectral overlap, the FRET signal is often contaminated by donor emission in the acceptor channel and by emission resulting from direct excitation of the acceptor molecule at the donor excitation wavelength and both signals which are termed Spectral Bleed Through (SBT) and in a calculation of the absolute FRET efficiency the extent of SBT should strictly be taken into account [76-79].

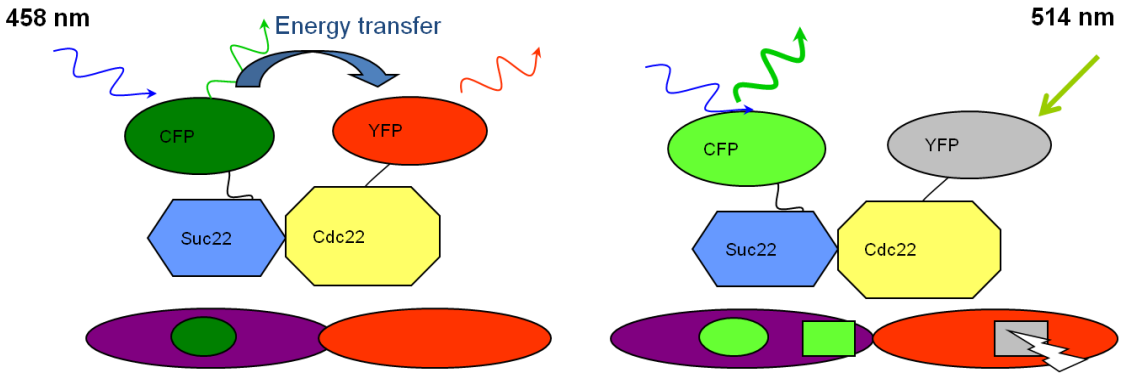

Figure 1.12: Cartoon representation of FRET between CFP- and YFP-tagged RNR subunits Suc22 and Cdc22 respectively and the relative energy transfer in the presence of the acceptor resulting quenching donor (CFP) energy (left-handside). Bleaching the YFP acceptor (eliminating YFP) resulting no more quenching for donor energy.

1.5 Confocal laser scanning microscopy (CLSM)

Initially fluorescence was observed by Sir John Hershel, but it was not until George Gabriel Stokes published it in a publication **"**on the refrangibility of light**"** in 1852 [80] and the term fluorescence coined. Stokes used the term as a description of the fundamental nature of the mineral fluorite (fluor-spar), composed of calcium fluoride and which, when illuminated with (UV) radiation gave a visible emission.

Fluorescence is an extremely sensitive reporter of information about a system. In reality fluorescence is an optical phenomenon which occurs when a molecule gets excited by absorbing photons from incident light. A transition from the ground to a high-energy electronic state can take place and then emits photons of longer wavelength as it goes back to its initial state, in a short time (less than 10^{-9} sec). This change in emission wavelength, the Stokes shift, occurs due to the dissipation of the absorbed energy by the excited molecule some through vibration or heat.

The confocal microscope is a modification of reflected light microscopy that is capable of imaging thin optical sections of about few micrometers thickness in both; *vitro* and

vivo. It was originally invented by Marvin Minsky in the mid-1955 [83] when he was junior fellow research at Harvard University attempting to image neural networks in unstained sample of brain tissue [81-83]. Due to the lack of intense light sources which are essential for imaging and computing software required to handle the large amounts of collected data, Minsky's invention remained unnoticed for a long time [84-85]. The word 'confocal' came from the first letter of names used by Dutch physicist G. Fred Brakenhoff and others in 1979 [85, 86].

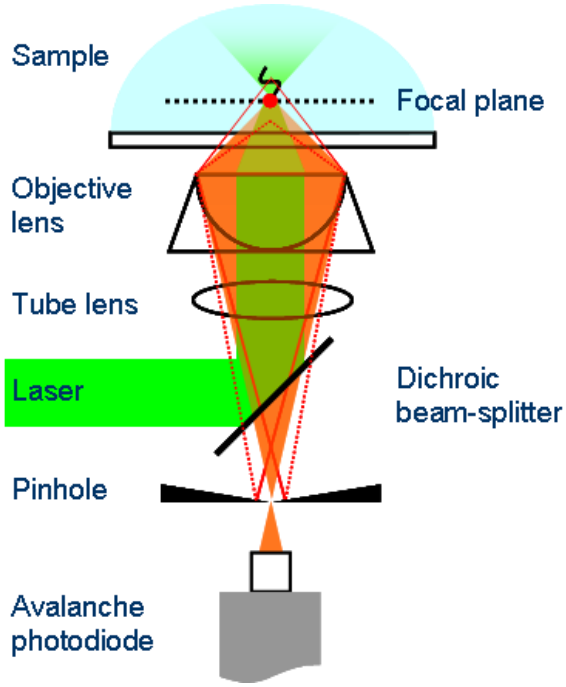

Figure1.13: Schematic diagram of the optical pathway and principal components in a laser scanning confocal inverted microscope. A laser is reflected off a dichroic mirror, passes through the objective lens and is then reflected off the specimen. The light retraces its path but passes through the dichroic mirror through the pinhole and then into the detector.

The principle of confocal fluorescence laser scanning microscopy (CLSM) is based on two key ideas: pointed by point illumination of the specimen and elimination of out of focus fluorescence [87-88]. In CLSM, the objective of the microscope forms a diffraction-limited

image of the laser source in the object plane within a confocal volume of the specimen. In a typical setup of CLSM (Figure 1.13) a coherent light emitted by a laser passes through a pinhole aperture that is situated in a conjugate plane with a scanning point on the specimen, defined by the objective lens. As the laser is reflected by a dichromatic mirror and scanned across the specimen in a defined focal plane, fluorescence from the specimen (in the same focal plane) passes back through the dichromatic mirror and is focused as a confocal point at the detector pinhole aperture. The significant amount of fluorescence emission that is collected from points above and below the objective focal plane is not confocal with the pinhole and is thus rejected at the aperture plane [85, 89].

In a typical optical system, in all fluorescence microscopes, resolution is limited by the numerical aperture of the optical components and by both the excitation and emission wavelengths of light. Resolution can be defined as the minimum separation between two points that results in a certain level of contrast between them [85, 90]. Imaging a point-like light source in the microscope generates an electromagnetic field in the image plane whose amplitude fluctuations can be considered as a sign of the response of the optical system to the specimen. This field is generally characterised by the amplitude point spread function and permits evaluation of the optical transfer features of the combined system components [84-85, 90-91]. The observable image of the point source formed in the microscope and recorded by the imaging system is the intensity point spread function (PSF). Resolution of a microscope is directly linked to the full width at half maximum (FWHM) of the intensity PSF of the instrument in the component directions [81, 85, 88, 93-94].

The axial resolution (*z*-axis) is calculated along with the optical axis and can be verified by the reduction of out-of-focus signal. The axial resolution is proportional inversely with the squared value of the numerical aperture, *NA*, of the objective lens, the wavelength of

light λ and the refractive index, n, of the sample medium. [85, 95] The axial resolution is also referred to as the depth of the field, d and can be calculated from Equation 1.3

$$d = \lambda\sqrt{n^2 - (NA)^2}\,\Big/\,(NA)^2 \qquad 1.3$$

The lateral resolution in the plane-of-focus is dependent on the Rayleigh Criterion, which defines distinct objects as those where the first minima of the Bessel function that describes the airy (diffraction) disk of one object overlaps with the maxima of the second object (Figure 1.14). The resolution is then given by [85, 96]:

$$r = \frac{1.22\lambda}{2N.A.} = \frac{1.22\lambda}{2n\sin\alpha} \qquad 1.4$$

Where n is the refractive index of the medium, λ is the wavelength of the emanating fluorescence, N.A is the numerical aperture of the objective lens and α is the angular aperture.

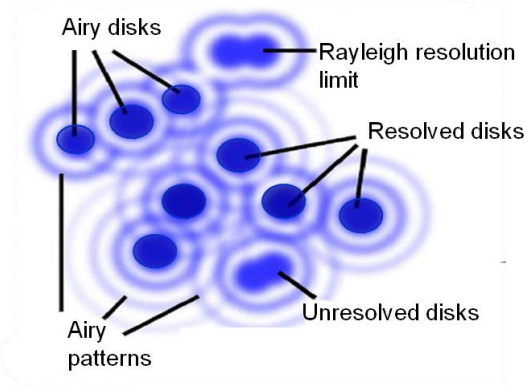

Figure 1.14: Representations of Airy disk and Airy patterns formed in the fluorescence microscope, Rayleigh criteria limit forms when two objects are regarded just resolved (when the principal diffraction maximum of one object coincides with the first minimum of the other). Resolved disk forms when the first minimum of one Airy disk is overlapped with the central maximum of the second Airy disk. Formation of unresolved disks can occur when zero contrast exists [85].

1.6 Near-total internal reflection fluorescence (nTIRF) microscopy

In addition to CLSM, another technique, the near-total internal reflection microscopy (near-TIR), has been used in this thesis for FRET imaging the interaction of RNR subunits in *S pombe* cells. The near-TIRF technique was performed on a modified TIRF microscopy. TIRF microscopy restricts the excitation of fluorescence to a plane at the interface between a high refractive index substrate and low refractive index medium. In this case, the optical phenomenon by which light, incident on the substrate at a supercritical angle, is completely reflected at the interface with a lower refractive index medium to produce a shallow evanescent field is exploited to restrict the excitation depth. Near-TIR highly inclined and oblique angle techniques have advantages of a single lens set-up for ease of alignment, extended fields of view and relatively shallow depths-of-field. Light sheet microscopies detect fluorescence orthogonal to an excitation beam that is focused to an extended sheet of light and thus potentially exhibit lower background scatter from the illumination source. However, accurate alignment of the light sheet close and parallel to the image plane of the lens make these techniques less easy to implement. Due to the simple adaptation of the TIRF microscope for high inclined illumination, nTIRF microscopy was explored as a means of achieving high contrast, high frame-rate, simultaneous dual-channel imaging, ultimately for long-term live cell studies. The fluorescence enhancement observed in the nTIRF images and more specifically the contrast ratio derived is primarily due the nature of the excitation field under highly inclined illumination. As a final demonstration of the sensitivity of nTIRF the technique was applied to been the visualization of *S. pombe* cells and the interrogation of the RNR interaction by performing photobleaching FRET.

1.6.1 Optical sectioning in CLSM, TIRFM and other techniques

The principle if TIRF microscopy is based on the production of an evanescent field at the interface of two media. Evanescence is generated only under the condition of total internal reflection (TIR) of an excitation beam at the interface between a substrate of high refractive index and sample of lower refractive index [129]. This condition is met when the angle of incidence of the excitation beam propagating in the medium of high refractive index is greater than a critical angle defined by the refractive index mismatch (n_2/n_1). The evanescent field is then produced on the low refractive index side of the interface and propagates parallel to the surface with a component normal to the surface that decays exponentially in intensity with distance z from the interface, at a rate determined by the characteristic penetration depth d. The penetration depth (typically in the range 30-300 nm for visible light) depends on the wavelength of the excitation light, λ, refractive indices n_1 and n_2, and the angle of incidence of the excitation beam θ_i according to Equation 5.1

$$d = \frac{\lambda}{4\pi\sqrt{n_1^2 \sin^2 \theta_i - n_2^2}} \qquad 1.5$$

For incident angles $\theta_i > \theta_C$ the penetration depth d decreases with incident angle θ_i such that some control over sampling different depths can be achieved albeit with a necessary interface.

In the conventional CLSM technique reported here optical sectioning is limited by the depth-of-field (DoF) of the objective lens. For highly restricted excitation in a single plane this requires a narrow DoF such that excitation and detection becomes rapidly inefficient above and below the plane of focus. For high numerical aperture objective lenses the DoF is limited by interference and phase shifts in the focused excitation source and fluorescence

wavefronts, while at low magnification the circle-of-confusion dominates, where light rays aligned close to the optical axis are focused at different points to those passing through the periphery of the lens. The overall DoF is generally given by the sum of the two contributions as

$$d = \frac{\lambda n}{NA^2} + \frac{n}{M \cdot NA} r \qquad 1.6$$

where λ is the excitation or emission wavelength, n the refractive index of above the objective (typically air or immersion oil), NA the numerical aperture of the lens, M the magnification of lens and r is the minimum resolvable lateral distance in the image plane. Thus the resolution increases longitudinally along the z axis more rapidly with NA than the lateral resolution which is dependent only on the first order inverse of the NA. While CLSM has high sectioning capabilities it lacks the widefield advantages of TIRFM.

TIRFM is ideal for capturing high resolution, high signal to noise ratio in planar samples such as monitoring membrane binding events occurring in exocytosis and receptor/transporter dynamics. Low laser power is required for TIRF to generate an axial resolution on the order 50 -100 nm with fast image acquisition, whereas, confocal requires high laser power to produce axial resolution on the order of 500 nm with slow image acquisition. [130-133] In contrast to both CLSM and TIRFM, epi-fluorescence microscopy provides high light throughput and wide-field imaging, but generally suffers from poor contrast and with large DoFs, lacks real optical sectioning with depth-of-field achieved only through post-acquisition image deconvolution poor contrast [134-135].

Recent developments have focused on optical configurations that can combine the wide-field imaging associated with epi-illumination and TIRF with the high longitudinal

resolution of CLSM. These techniques can be loosely categorised as TIRF-like, such as highly inclined lamination optical microscopy (HILOM) and oblique plane microscopy (OPM), or light sheet microscopies that include numerous acronyms such as selective plane illumination microscopy (SPIM), objective coupled planar illumination microscopy (OCPIM), light sheet fluorescence microscopy (LSFM), digital scanned laser light sheet fluorescence microscopy (DSLM), orthogonal-plane optical sectioning (OPFOS), and thin light sheet microscopy (TLSM). Highly inclined and oblique angle techniques have advantages of a single lens set-up for ease of alignment, extended fields of view and relatively shallow depths-of-field. Light sheet microscopies detect fluorescence orthogonal to an excitation beam that is focused to an extended sheet of light (typically using a cylindrical lens) and thus potentially exhibit lower background scatter from the illumination source. However, accurate alignment of the light sheet close and parallel to the image plane of the lens make these techniques less easy to implement. Due to the simple adaptation of the TIRF microscope for high inclined illumination, nTIRF microscopy was explored as a means of achieving high contrast, high frame-rate, simultaneous dual-channel imaging, ultimately for long-term live cell studies.

1.6.2 Principles of near-TIRF and oblique angle microscopy

The near-TIRF principle is analogous that described elsewhere (Figure 1.15) [136-137] highly inclined laminated optical sheet (HILO) microscopy which can be easily performed on a TIRFM setup [136-137]. Essentially, a thin laser beam is inclined at a subcritical angle on a TIRFM microscope configured in the objective-type TIR mode in which the high NA of the objective is exploited to achieve high angles of refraction of the excitation beam. Focusing this beam at the back focal plane of the objective produces a near- collimated beam that

traverses the specimen at a highly inclined angle (with respect to the optical axis). The oblique angle of illumination essentially produces an "optical slice" through the specimen of thickness in *z* on the order of

$$dz = \frac{D}{\tan\theta_t} \qquad 1.6$$

where D is the diameter of the illuminated footprint and θ_t is the angle of refraction of the transmitted beam. For typical TIRF illumination diameters of D = 30 μm, in order to achieve a sectioning depth of 3 μm, in this case the typical diameter of the *S. pombe*, high angles of refraction in the region of θ_t = 84^o are required. For a cytosol/glass interface (n_2/n_1 = 1.38/1.55) this requires an incident beam angle of around θ_i = 65^o and thus a lens of minimal $NA = n_1 \sin\theta_i$ = 1.37. One advantage of illuminating at high angles is that the specimen directly above the objective-lens along the optical axis is not subject to excitation by the beam with the potential benefits of reduced autofluorescence and background scatter. Furthermore is has also been reported that photo-bleaching was found to be significantly lower than in CLSM and four to eight-fold increases in signal to-noise ratio over epi-illumination have also been observed. A clear demonstration of the technique was provided by imaging the distribution of single GFP-importin β molecules across the depth the nucleus of a mammalian cell by changing the optical thickness *dz* across a series of images [136]. The achievable field of view in near-TIRF microscopy can be limited because the "slab" of light is strictly tilted with respect to the sample plane. To compensate for this in more recent development the image plane is also tilted with optics in the detection path that match the image plane to the illuminated object plane [138].

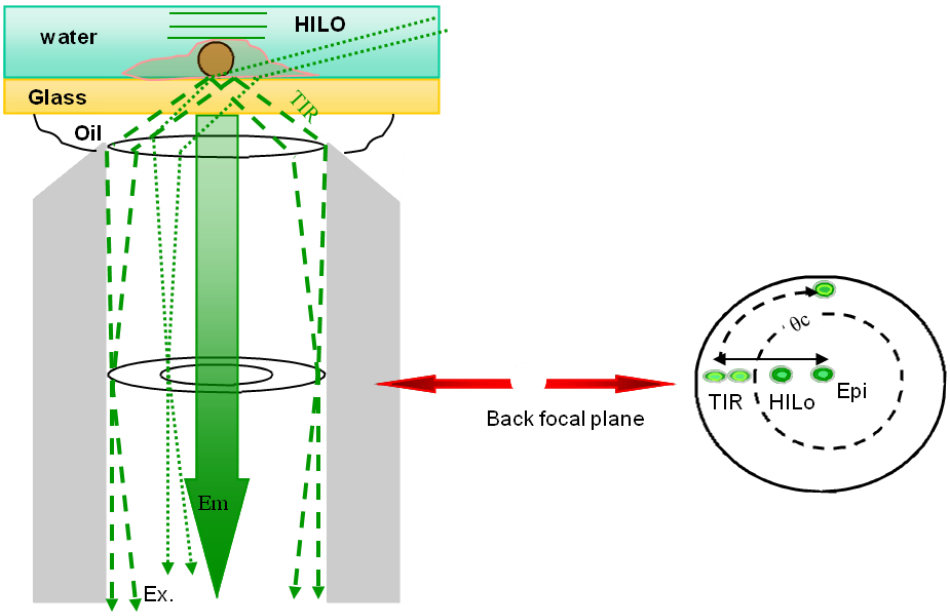

Figure 1.15: The setup of TIRFM objective type. Excitation light (Ex, 458 nm) is positioned on the edge of the back focal plane of a high-NA (1.45) objective lens. Translocation can change the incident angle and penetration depth of the evanescent field, HILO can be permitted when less than the critical angle (θi < θc) obtained. Scanning the beam in a circle or semicircle can decrease interference artifacts when using laser light. Em, emitted light [138].

1.6.3 Optical near-TIRF enhancement

Snell's law describes the interactions at a boundary between two media of different refractive indices n_1 and n_2 where $n_1 > n_2$ [134]. When an incident light-beam, propagating through medium of n_1, strikes the boundary with an incident angle $\theta_{i,}$ a fraction of the power in this ray is reflected with angle θ_r while the remaining power is transmitted into medium n_2 and refracted with angle θ_t defined by Equation 1.7 and illustrated in Figure 1.16:

$$n_1 \sin\theta_i = n_2 \sin\theta_t \qquad 1.7$$

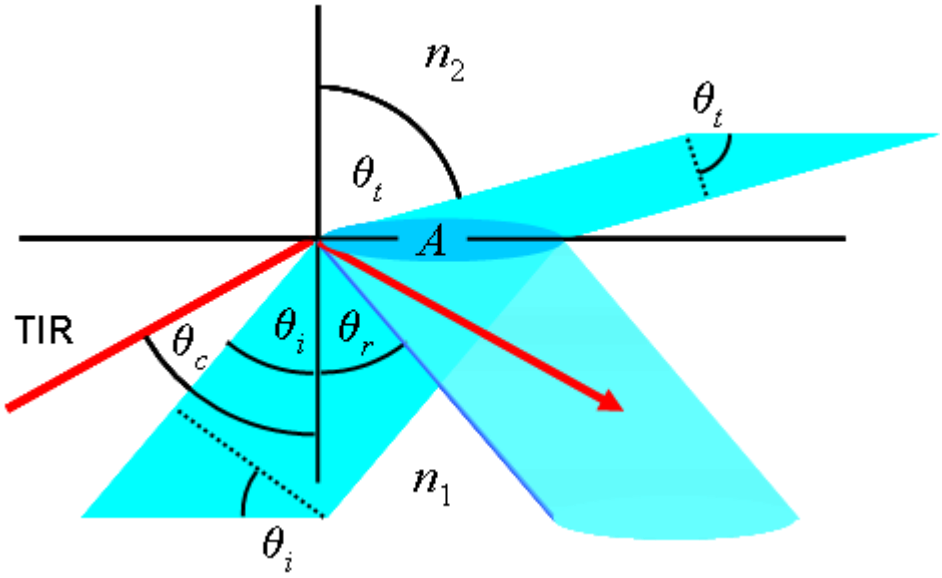

Figure 1.16: Schematic of incident, refracted, reflected rays of light at the interface between two media (having refractive indices n_1 and n_2). TIR (red line) is produced when the rays pass from a higher to a lower refractive index at an angle $\theta_i > \theta_c$ the critical angle. The illuminated area A is a projection of the incident beam cross-section and hence a function of the incident angle θ_i.

Total internal reflection occurs at a maximum angle of refraction $\theta_t = 90^o$, which then defines a critical angle θ_c at which the light must be incident for the beam to undergo TIR.

$$\theta_c = \sin^{-1}\left(\frac{n_2}{n_1}\right) \qquad 1.8$$

For an interface between glass (n_1 = 1.52) and water (n_2 = 1.33), the value of the critical angle θ_c is ~ 61^o which rises to ~65.2^o in the case where the low refractive medium is a cell, where the refractive index is typically that of the cytosol (n_2 = 1.38).

The variation in the electric field intensity of the transmitted light beam as the angle of incidence approaches the critical angle can be determined from Fresnell's equations for the

coefficients of reflection. For an incident angle $\theta_i > 0$ the electric field of the beam will have a component parallel and perpendicular to the interface the fraction of the incident field reflected into each component are given by the reflection coefficients

$$r_{\parallel} = \frac{\tan(\theta_i - \theta_t)}{\tan(\theta_i + \theta_t)} \qquad r_{\perp} = \frac{\sin(\theta_i - \theta_t)}{\sin(\theta_i + \theta_t)} \tag{1.9}$$

The energy flux per unit area or intensity of each component is proportional to the square of the respective coefficient and the total intensity of the reflected beam proportional to the sum of the squares $r^2 = r_{\parallel}^{\ 2} + r_{\perp}^{\ 2}$. For an incident beam, projecting a cross-sectional area *A* on the plane of the interface, the cross-section of the beam itself is $A\cos\theta_i$, while that of the transmitted beam is $A\cos\theta_t$. Using Snell's law the ratio of transmitted and incident beam areas is given by

$$\frac{A\cos\theta_t}{A\cos\theta_i} = \frac{\sqrt{1-(n_1/n_2)^2 \sin^2\theta_i}}{\cos\theta_i} \tag{1.10}$$

For an incident beam of intensity I_0, the energy flux through this cross-section is given by $I_0 A\cos\theta_i$. The energy flux in the reflected beam is $r^2 I_0 A\cos\theta_r$ and that in the transmitted beam is $t^2(n_2/n_1)I_0 A\cos\theta_t$ where t^2 is the Fresnel coefficient of transmission and n_2/n_1 accounts for the change in field strength on passing from the high to low refractive medium. By conservation of energy

$$r^2 I_0 A\cos\theta_r + t^2 \frac{n_2}{n_1} I_0 A\cos\theta_t = I_0 A\cos\theta_i \qquad 1.11$$

And given that the angle of reflection must equal the angle of incidence Equation 1.8 reduces to the conventional relationship between transmission and reflection

$$r^2 + t^2 \frac{n_2 \cos\theta_t}{n_1 \cos\theta_i} = 1 \qquad 1.12$$

Using the relationship between incident and transmitted beam cross-sections in Equation 1.7, Equation 1.9 can be rearranged to obtain t^2 the fraction of the incident intensity in the transmitted beam at the interface as a function of the incident beam angle θ_i, which is given by

$$t^2 = \frac{\left(1 - r^2\right) n_1 \cos\theta_i}{n_2 \sqrt{1 - \left(n_1 / n_2\right)^2 \sin^2\theta_i}} \qquad 1.13$$

1.7 Structure of the thesis

Chapter 2 describes the materials and methods used to investigate RNR in *S. pombe*. This includes an overview of the library of yeast strains, constructed using standard cloning and transfection technique that have been used in the FRET experiments reported in this thesis. Single fluorescent protein-tagged RNR strains (CFP/YFP-Suc22, Cdc22-CFP/YFP) were ultimately crossed to obtain a set of RNR wild type (Wt) double-tagged strains with Spd1 present or deleted followed by various types of verifications like PCR, WB and gel

filteration. In addition a library of 41 mutants, created by Nestoras *et al. via* the alanine scanning mutagenesis of the *spd1* gene is also discussed in this chapter in relation to their construction and genetic characterisation.

Chapter 3 presents the results of CLSM imaging experiments and the analysis of FRET by acceptor photobleaching for Wt double FP-tagged RNR strains in the presence and absence of Spd1. Controls employing swapped FP-tags and single tagged strains, to test for any anomalous photophysics exhibited by the FPs, which may be detrimental to the measurement of FRET is also presented. Also reported here, are results of FRET imaging of the same strains following treatment with hydroxy urea (HU), a radical quencher and hence known inhibitor of RNR, 4-nitroquinoline 1-oxide (4NQO), an inducer of DNA damage and finally after heat shock with FRET monitored at elevated temperatures.

Chapter 4 reports the CLSM imaging results of 41 Spd1 mutant strains with double FP-tagged RNR and corresponding FRET measurements. Correlations, or lack thereof, between FRET levels observed in CLSM and the loss of R2 (Suc22) nuclear localisation, restraint of RNR activity, the functional binding domains of Spd1 and its degradation as determined from genetics and biochemical assays are examined. A number of possible models are presented that provide useful insight into what FRET represents in the formation of the RNR complex and how Spd1 may mediate the transition between an inactive and active enzyme.

Finally Chapter 5 presents a novel imaging technique, near-total internal reflection microscopy (nTIRF) that has been developed and applied to image the *S. pombe*, RNR system with demonstrated enhanced contrast over conventional wide-field epi-fluorescence. The addition of a simple dual-view optic in the detection train has allowed the simultaneous imaging of donor CFP and acceptor YFP channels on a single camera. The imaging system is characterized in terms of excitation field enhancement near-TIR and image contrast ratio as

well as the constraint in excitation depth by oblique angle illumination. Finally measurements of FRET on double FP-tagged RNR complex in the wild-type *S. pombe* cells are presented and demonstrated to highly consistent with the results of CLSM.

Chapter 2

Materials and Methods

2.1 Cloning

Yeast strains were constructed using standard cloning and transfection techniques. From the simple isolation of genes for protein expression to the transformation of organisms, these techniques have been widely used across genetics, molecular and cell biology. Since the first demonstration of a DNA plasmid, constructed from separate fragments and forming a fully functional replicon in *E. coli* [97], tools and procedures for cloning DNA in bacteria are now highly developed and have been used here to transform fluorescent proteins into the RNR system of *S. pombe* yeast cells

The ability to genetically manipulate cells by incorporation of exogenous DNA constructs has allowed the study of cell structure and cellular processes and the effects of mutation thereon, in a highly systematic manner by the accurate and selective addition, modification, deletion and/or substitution of genes in whole or in part. The importance of cloning in yeast, in particular in the study of the cell-cycle in *S. pombe*, is exemplified by early studies of the cell-cycle in *S. pombe* by Lee and Nurse [98]. By cloning the human homologue of the cell cycle control gene *cdc2* into fission yeast, they ultimately established *S. pombe* as an archetypal eukaryotic cell and model for mammalian cell growth, replication and division. Coupled with the pioneering yeast work of Fields and co-workers [99] on the two-hybrid system for the identification of protein-protein interactions between an unknown and target, these techniques have been central to the rapid growth in the number of identifiable

and functional protein-protein interactions in the cell, including those of the cell-division cycle. Since these studies the cloning of other mammalian genes has led to a greater understanding of inducers on the cell cycle such as the mammalian homologous gene CDC25 of the fission yeast *cdc25+* mitotic inducer and also on the cycle checkpoint control as HRAD1 and MRAD1 mammalian homologues of the fission yeast rad1+ cell cycle checkpoint control gene [100-101].

2.2 Summary of FP-tagged *S. pombe* strains

The strain constructs were created using PCR to amplify the desired open reading frame (ORF) with primers having at least 80 bp homology to the genomic ORF, followed by insertion into the yeast genome by homologous recombination. The fluorescent protein-tagged RNR strains (CFP/YFP-Suc22, Cdc22-CFP/YFP) were made by Dr. Adam Watson [97-99,102], as well as the *spd1*::ura4 strain, which will be referred to as Spd1 deleted. The strains were crossed to obtain a set of RNR wild type (Wt) double-tagged strains with Spd1 present or deleted. Table 2.1 summarises the *S pombe* library of fluorescent protein-tagged RNR strains used in this work and the base strains from which they are derived.

The *spd1* mutant constructs were created by independent alanine mutagenesis PCR [63] by Dr Marius Poitela and Dr Konstantinos Nestoras and again integrated into *S. pombe* genome by homologus recombination. Finally, different *spd1* mutants were crossed with the double- tagged strains and selected for different markers. G418 resistance was used to validate the presence of Cdc22-CFP/YFP construct, while loss of uracile resistance was used to indicate the correct integration of the *spd1* mutant. PCR was used to confirm the presence of Suc22-CFP/YFP. All the *spd1* mutants were incorporated in the YFP-Suc22-Cdc22-CFP

strains and half the array was crossed into the RNR "swapped- tagged" strain (Wt/ CFP-Suc22-Cdc22-YFP) strain, as outlined in Table 2.2.

Base strains	AS501	ade6-704 leu1-32 uraD18 h-
	AS503	ade6-704 leu1-32 uraD19 h+
Spd1 deleted	AS128	*Spd1*::ura4 ade6-704 ura4-D18 leu1-32 h-
	AS129	*Spd1*::ura4 ade6-704 ura4-D18 leu1-33 h+
RNR single tags	AS101 YFP-	suc22 (nt) ade6-704 ura4-D18 leu1-32
	AS102	cdc22-YFP::Kan (ct) ade6-704 ura4-D18 leu1-32
	AS103	CFP-suc22 (nt) ade6-704 ura4-D18 leu1-32
	AS104	cdc22-CFP::Kan (ct) ade6-704 ura4-D18 leu1-32
RNR double tags (Spd1+ & Spd1-)	AS108	YFP-suc22 (nt) cdc22-CFP::Kan (ct) *Spd1* wt ade6-704 ura4-D18 leu1-32 h-
	AS120	YFP-suc22 (nt) cdc22-CFP::Kan (ct) *Spd1* wt ade6-704 ura4-D18 leu1-32 h+
	AS122	YFP-suc22 (nt) cdc22-CFP::Kan (ct) *Spd1*::ura+ ade6-704 ura4-D18 leu1-32 h-
	AS123	YFP-suc22 (nt) cdc22-CFP::Kan (ct) *Spd1*::ura+ ade6-704 ura4-D18 leu1-32 h+
	AS154	YFP-suc22 (nt) cdc22-CFP::Kan (ct) *Spd1*::ura+ ade6-704 ura4-D18 leu1-32 h+
	AS155	YFP-suc22 (nt) cdc22-CFP::Kan (ct) *Spd1*::ura+ ade6-704 ura4-D18 leu1-32 h-

Table 2.1: Library of *S. pombe* strains with single-tagged RNR subunits derived from the base and Spd1 deleted strains and double-tagged RNR strains resulting from crossing [63].

Spd1 mutants	AS01	*Spd1*::mutant ade6-704 ura4-D18 leu1-32 and same background with *Spd1* mutants 2-41
Spd1 mutants (CFP-YFP)	AS-CY2	suc22-CFP (nt) cdc22-YFP::Kan (ct) *Spd1*-m2 ade6-704 ura4-D18 leu1-32 and same background with *Spd1* mutants 4, 7, 10-14, 19, 21-24, 26,27,29, 33, 34, 36, 37, 38, 41
Spd1 mutants (YFP-CFP)	AS-YC1	suc22-YFP (nt) cdc22-CFP::Kan (ct) *Spd1*-m1 ade6-704 ura4-D18 leu1-32and same with *Spd1* mutants 1-2, 4-5, 9, 12-18, 21-32, 34-36, 38-40

Table 2.2: Library of *S pombe* strains with Spd1 mutant strains and with double tagged RNR and Spd1 mutant strains that have been used to create the desired system [63].

2.3 Construction of the FP-tagged RNR & Spd1- strains

The first step in cloning is the design of the vector primers of interest that are used in the Polymerase Chain Reaction (PCR) with the engineered plasmid to create the required strains (exogenous DNA) which will be hosted later in the genome by homologous recombination.

2.3.1 FP-tagged Cdc22

For Cdc22, encoding the large subunit of RNR, fluorescent protein tags were introduced at the protein C-terminus. Using nucleotides containing 500bp of homology to the Cdc22 locus, a construct containing the fluorescent protein tag, the *S. cerevisiae* ADH1 terminator sequence and the kanamycin resistance marker (conferring resistance to the antibiotic G418) was amplified from the corresponding plasmid vector. The result is a linear fragment was used to transform Wt *S. pombe* cells by homologous recombination and cells screened on YEA plates containing the G418 antibiotic. Transformants were confirmed by

both PCR and sequencing. Figure 2.1b shows the transformed sequence and a gel purification (GFX kit) which consists in this case of 8 lanes. The first lane is the DNA ladder which provides a reference for PCR product length. Lane 2, 5, 6, 7 and 8 are the G418 resistant transformants, the larger PCR product corresponds to insertion of the C-terminal tag sequence while lane 3 and 4 are non integrated products.

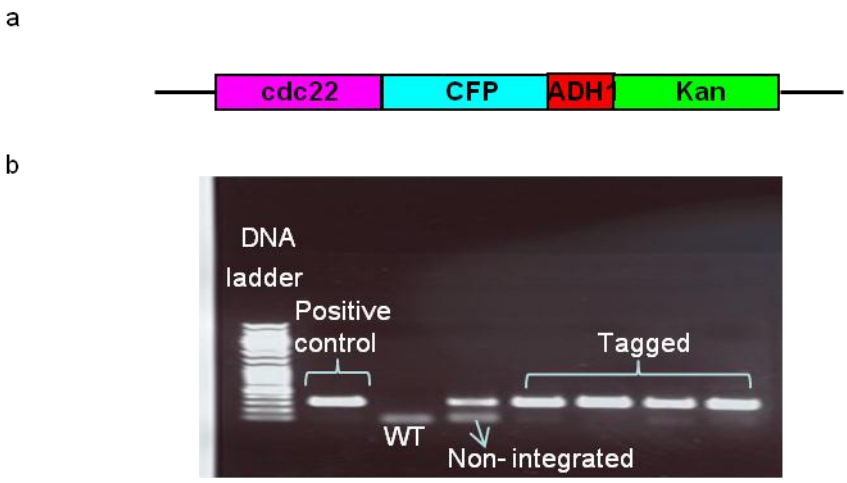

Figure 2.1 a) Schematic of the constructed strain (FP - fluorescent protein, S. cerevisiae ADH1 terminator, KAN – kanamycin resistance cassette) after integration by homologous recombination that are ready to verify. b) PCR verification of G418 resistant transformants.

2.3.2 FP-tagged Suc22

Both RNR genes *suc22* and *cdc22* are essential genes, meaning that deletion of the gene sequences or disruption of the protein function leads to cell death. Tagging *suc22* at the C-terminus was found to be lethal, presumably because protein function was compromised. Therefore, for Suc22 the fluorescent protein tag was introduced at the N-terminus. The used system allows N- terminal tagging and ultimately control of *suc22* gene expression from its native promoter in a two-step process. The strain was confirmed by both PCR and sequencing.

Figure 2.2b shows a gel purification (GFX kit) which consists in this case of 13 lanes. Lanes 5, 7 and 10 are PCR products corresponding to insertion of the N-terminal tag sequence while the lanes 2, 3, 4, 6, 8 and 11 correspond to non integrated products. Lanes 12 and 13 are the positive and negative control respectively.

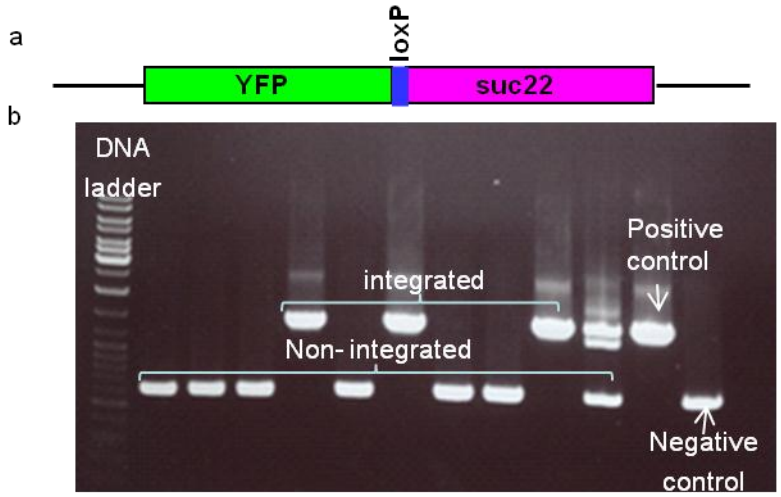

Figure 2.2: a) Schematic of the constructed strain that contains of *suc22* gene, YFP after integration by homologous recombination. c) PCR verification.

Both RNR tagged strains were found to be viable and subsequently crossed together to create the double- tagged strain. To test any phenotypic effects of the tags, spot tests were performed. The single and double tagged strains were exposed to hydroxyurea (HU - 0, 2.5mM, 5mM and 7.5mM), camptothecin (CT – 0, 4uM, 6uM, 8uM, 10uM and 12uM) and ultraviolet light (UV- 0, 50 joules and 100 joules). The only phenotype observed was a slight, slow-growth defect of tagged Suc22 cells on plates containing HU.

For our FRET studies, both Suc22 and Cdc22 were tagged with the GFP derivatives cyan fluorescent protein (CFP) and yellow fluorescent protein (YFP). The following double

tagged strains were constructed, Wt/Suc22-CFP/Cdc22-YFP and Wt/Suc22-YFP/Cdc22-CFP so any FRET data could be confirmed by analyzing the strain with the tags reversed.

2.4 Western Blot (WB) analysis of FP-tagged RNR proteins

Preparation of cell extracts for SDS-PAGE (sodium dodecyl sulphate polyacrylamide gel electrophoresis) and Western blotting was performed as described by Dr. Adam Watson [104]. Cells incubated with SDS are lysed by the solubilisation of the lipid membranes and proteins are rendered negatively charged by the anionic surfactant, the number of charges being proportional to the size of the protein which allows size separation across a potential difference. Samples were resolved by 8% SDS-PAGE, transferred onto nitrocellulose membrane and probed with mouse monoclonal anti-Green fluorescent protein antibody (diluted 1:4000; Roche). Peroxidase-conjugated rabbit-anti-mouse secondary antibodies (diluted 1:5000, Dako A/S) were used to detect the primary antibody and these were revealed using an ECL detection kit (Amersham). Radioactive detection was used to probe protein bands by placing medical X-ray film directly against the western blot and developed for a period of time (few minutes) as it is demonstrated in Figure 2.3.

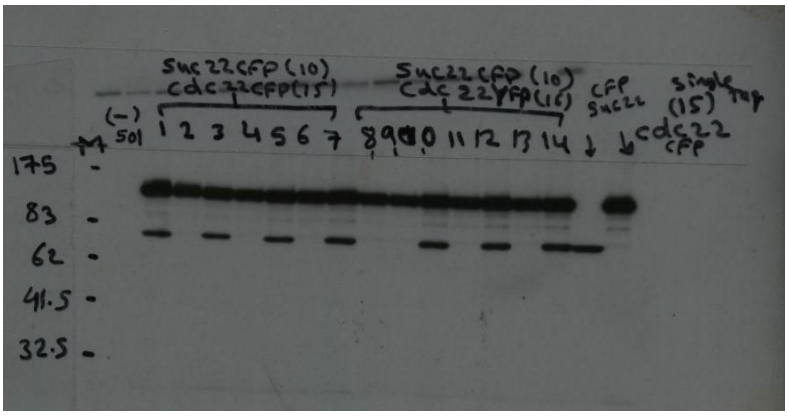

Figure 2.3 Radioactive detection using medical X-ray film directly against the WB which develops as it is exposed to the label and creates dark regions that correspond to the protein bands of interest. The first Lane corresponds to the marker which is used as a reference followed by negative control (untagged WT strain). Lanes 1-7 corresponds to double tag proteins (Suc22-CFP+Cdc22-CFP), only 1, 3, 5 and 7 are integrated while the rest are not specified. Lanes 8-14 correspond to the double tag strains (Suc22-CFP+Cdc22-YFP), only 10, 12 and 14 have integrated. The last two lanes are single tag proteins Suc22-CFP and Cdc22-CFP respectively.

2.5 Spd1 deleted

As *S. pombe spd1* is a non-essential gene, the *spd1* coding sequence was replaced by *ura4+* selectable marker in a similar way that was used in the RNR construction;. The process was originally implemented by Dr. Adam Watson [63].

2.6 Spd1 Mutants

To investigate the role of the Spd1 in the regulation of RNR Dr. K. Nestoras has created 41 independent mutants of *spd1* by site-directed mutagenesis [63]. Each individual mutant protein was created by substituting three individual alanine by three amino acids after the first methionine as shown in Figures 2.4a and 2.4b.

a

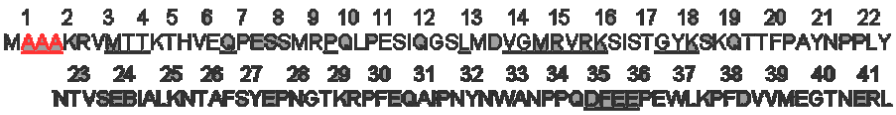

b

Residue No.	*spd1*-mutant No.	Residue No.	*spd1*-mutant No.
1-3	*spd1-m1*	64-66	*spd1-m22*
4-6	*spd1-m2*	67-69	*spd1-m23*
7-9	*spd1-m3*	70-72	*spd1-m24*
10-12	*spd1-m4*	73-75	*spd1-m25*
13-15	*spd1-m5*	76-78	*spd1-m26*
16-18	*spd1-m6*	79-81	*spd1-m27*
19-21	*spd1-m7*	82-84	*spd1-m28*
22-24	*spd1-m8*	85-87	*spd1-m29*
25-27	*spd1-m9*	88-90	*spd1-m30*
28-30	*spd1-m10*	91-93	*spd1-m31*
31-33	*spd1-m11*	94-96	*spd1-m32*
34-36	*spd1-m12*	97-99	*spd1-m33*
37-39	*spd1-m13*	100-102	*spd1-m34*
40-42	*spd1-m14*	103-105	*spd1-m35*
43-45	*spd1-m15*	106-108	*spd1-m36*
46-48	*spd1-m16*	109-111	*spd1-m37*
49-51	*spd1-m17*	112-114	*spd1-m38*
52-54	*spd1-m18*	115-117	*spd1-m39*
55-57	*spd1-m19*	118-120	*spd1-m40*
58-60	*spd1-m20*	121-123	*spd1-m41*
61-63	*spd1-m21*		

Figure 2.4 *spd1* mutants: a) *spd1* sequences, every three amino acids were replaced by three alanines to produce one mutant. b) Mutant array (labelled *spd1-m1* to *spd1-m41*) [63].

Once all the mutants were obtained on plasmids, the mutated *spd1* genes were inserted in the *S. pombe* yeast cell at the locus of the *Spd1* wild type gene. Thus, a collection of the 41 yeast strains, labelled *spd1-m1* to *spd1-m41*, were generated with the different mutations indicated in Figure 2.4 that were verified by sequencing the *spd1* gene. To reiterate the conclusions from genetic assays of Nestoras *et al* [63] a number of the *spd1* mutants were defective in Suc22 localisation, including complete loss of nuclear localisation (as seen in *spd1-m2, spd1-m14 and spd1-m26*). Three mutants, *spd1-m12, spd1-m13* and *spd1-m33* displayed weak localisation in G2 cells and this was completely lost upon HU treatment.

Finally, four mutants, *spd1-m22, spd1m-38, spd1-m40* and *spd1-m41* showed strong localisation slowly reversed by treatment of HU. No mutant showed a complete failure to delocalise Suc22 to the cytoplasm, unlike the *Spd1*deleted strain [63].

Considering RNR activity with respect to Spd1 degradation, in *csn1* mutants Spd1 is stable and RNR predicted to be inhibited. Only mutants (*spd1-m10, spd1-m11, spd1-m13, spd1-m14, spd1-m15, spd1-m16, spd1-m17, spd1-m18, spd1-m19 and spd1-m26*) have rescued *rad3, csn1* synthetic lethality with efficiency approaching that of the *spd1* deleted [63] From this assay [63], it has been showed that there is a lack of RNR inhibition when Spd1 is degraded and thus increased dNTPs production. When *csn1* is deleted, there will be no degradation of Spd1 and hence a greater loss of RNR activity leading to apoptosis (cell death). In the case of DNA damage, *rad 3* will be activated and in turn csn1 to produce more dNTPs *via* Spd1 degradation. Therefore, it was concluded from this assay that growth of the cells is correlated with loss of the inhibitory function of Spd1. In the alternative assay in which the specific component of the ubiquitin ligase required for Spd1 degradation, *ddb1* was deleted (*ddb1*-) spore formation was found to be restored in mutants *Spd1-m3, Spd1-m11* through *spd1-m16, spd1-m18, spd1-m26, spd1-m30, spd1-m34* through *spd1-m38, spd1-m41* [63]. This assay shows that with *ddb1-*, there is more RNR inhibition because Spd1 is not degraded and thus no more spore formation in meiosis and vice versa. Thus, the recovery of spore formation is correlated with the loss the inhibitory function of Spd1.

2.7 Synchronization of *S. pombe* cells

In general a yeast cell culture in the log phase (exponential) of the population growth will be have a distribution in the fraction of cells in the different phases of the cell cycle, G1, S, G2 and M. This results from the fact that the residence time in a particular phase is distributed

across the cell population with a characteristic average that is dependent on the growth conditions. In our case this is typically 20 and 48 minutes in the S and G2 phases respectively. Thus, in order to investigate FRET contributions in a particular phase we may only be sampling a small fraction from the total population. Here, particular cell phases were enhanced by synchronizing cell growth *via* elutriation, a process by which cells are separated according to size by the opposing forces of centrifugation and the pump pressure of a counter flow. In the elutriation chamber, sedimentation of cells suspended in a medium of yeast extract peptone (YEP) is balanced by a flow velocity that establishes a size gradient throughout the volume of the chamber, from larger cells at the base to small cells at the top of the chamber. Increasing the flow rate against the centrifugal force moves the size gradient through the chamber until the smallest size fraction elutriates from the chamber mouth at the top. Increasing size fractions are elutriated with increasing flow rates. Evidently in the septation phase S cells are small and elutriated first whilst those in the mitotic phase M are extended and elutriate last. In this manner the fraction of cells in a particular phase can be isolated. S phase and M phase fractions were elutriated every 15 min and cells counted over the course of approximately 5 hrs. The resulting populations as a function of time are shown in Figure 2.5.

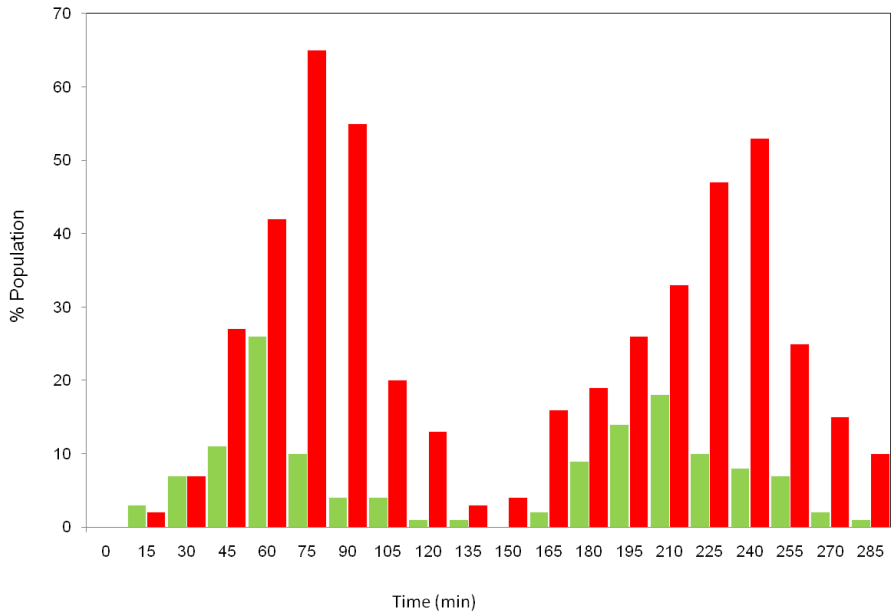

Figure 2.5 The percentage of cells in the septation S (red) and mitotic M (green) phases as a function of time for two cell cycles.

Synchronizing phase populations in this manner has facilitated the investigation of larger numbers of cells to build more statistically robust FRET averages whilst circumventing the laborious task of sampling from a mixed phase population.

2.8 Cell growth and fixation

Cells were grown to log phase at 30°C in Yeast Extract (YE) media. For FRET analysis using confocal-microscopy, cells were harvested, washed with Phosphate buffered saline (PBS, a water based salt that contains sodium chloride and sodium phosphate). The cell then fixed with methanol and dried on the slide (76x26x1.35 mm) and a drop of 2.5 µl mounting agent added (50% glycerol, 50%water) before being covered with a coverslip (22x22 mm) to

prevent evaporation. Samples for near-TIRF imaging were prepared in a similar way, the only difference is 40x22 mm coverslips the support instead of a slide.

In the case of treating the cell with Hydroxy Urea (HU – Sigma, H8627-100G), the compound was added to the culture medium at a final concentration of 20 mM and the cells incubated for 4 hours prior to analysis. For the alternative drug, 4-NitroQuinoline 1-Oxide (4NQO – Sigma, Aldrich N8141- 1G) cells were incubated for the same period at a final NQO concentration in YE growth medium of 5 μM.

2.9 RNR after heat shock.

The transcriptional response to heat shock is conserved in eukaryotes organisms, and is controlled by a heat shock factor (HSF). In *S. pombe*, this transcription factor is essential for growth [46]. It has been reported that the larger transcript of Suc22 is highly induced after heat shock (42°C), while Cdc22 transcripts are reduced [115]. This strong induction of Suc22 has been demonstrated to be part of a separate pathway from that of DNA damage repair (*rad1* independent). The aim here, was to see how heat shock affected the RNR complex formation and FRET. This was undertaken, in brief, by growing in parallel RNR double-tagged strains in both presence of *spd1* and *spd1::ura4* at 30°C and separately at 42°C for 145 min after which the heat shock culture was shited back to 30°C

2.10 Confocal laser scanning microsope instrumentation

A laser scanning microscope Ziess (LSM 510) was used to image *S. pombe* cells and perform FRET experiments. Figure 2.6 shows a simplified optical train for the microscope. The output of an Argon ion gas laser (Innova 70, Coherent Inc. USA) is directed through a *xy* scanning-

head *via* a switchable, longpass dichroic beamplitter (either a 458 nm or 514 nm) and through a tube lens and objective lens (C-Apochromat NA 1.2 x63, Zeiss, USAO)to the sample *via* a prism in the base of the microscope body. Fluorescence, collected by the same objective pass back through the same optical path through the scanning-head, which now maps the diffraction-limited focus onto the pinhole. Emission emerging from above and below the plane of focus is rejected at the pinhole and only fluorescence from the focal plane passes to the photomultiplier (PMT) detector. Short and long wavelength emission is separated at a dichroic beamsplitter (545 nm) and projected onto orthogonal PMTs after further spectral filtering through bandpass filters (475-525 nm for CFP and 530-600 nm for YFP). A switchable dichroic mirror between the objective lens and tube allows widefield imaging, under illumination from a mercury vapour lamp to check cell quality and locate regions of interest. Furthermore, differential brightfield and interference contrast imaging (DIC) was made possible *via* a conventional halogen lamp and condenser system and coupled Wollaston prisms and polarisation filters.

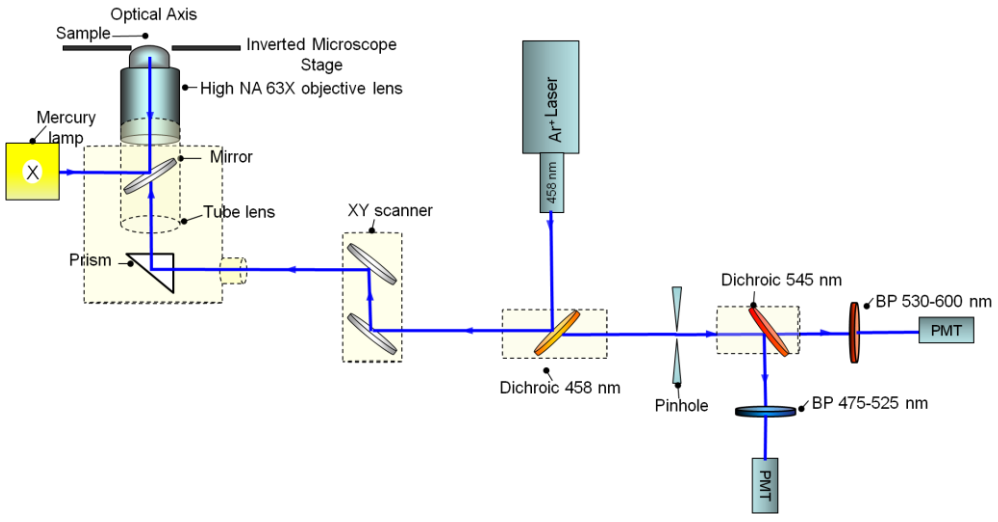

Figure 2.6: Schematic of the dual-channel confocal microscopy. For CFP excitation (donor), laser line 458 nm is used and 458 nm dichroic which passes the light to the xy scanner and then to the sample through the objective lens. For emission, another dichroic 545 nm is used to separate the emission of the donor from the

acceptor. Before emission imaged by two photomultipliers (PMT), each of them passes through beampass (BP) filter 475-525 nm and 530-600 nm respectively.

2.10.1 Image acquisition and processing

In a typical experiment performed on transformed *S. pombe* containing both RNR-tagged subunits Suc22-CFP and Cdc22-YFP, cells were initially fixed with methanol prior to loading on the microscope according to the protocol described above. Under these conditions imaging times were limited by a substantial increase in autofluorescence over about few hours, as was observed in untagged wild-type cells. Subsequent fixation with formaldehyde allowed extended periods of imaging (for few days) with negligible changes in the autofluorescence.

Image acquisition consisted of a pre-bleach and post-bleach set of images, each set containing a brightfield DIC image, a CFP and YFP fluorescence image on separate channels. Following acquisition of a DIC image, the microscope was configured with the 458 nm dichroic for scanning-confocal imaging of the sample with the 458 nm line of the Argon ion laser, providing near-optimal excitation of the donor CFP tag, as seen from the absorption spectrum presented in Figure 2.10. Fluorescence images on CFP (475-525 nm) and YFP (530-600 nm) channels were acquired simultaneously at a typical laser power of 1.37 μW and corresponding to a diffraction-limited intensity of 0.8 k Wcm^{-2}. The fraction of the donor CFP and acceptor YFP fluorescence spectra captured in these channels can be seen in Figure 2.10 which summarises the spectral range of the experiment.

Acquisition of the pre-bleach image set was followed by photobleaching of the acceptor by scanning the 514 nm line of the Argon ion laser across a specific region of interest (ROI) covering the whole cell or within the cell cytoplasm or nucleus only for a number of iterations between 500 and 2000.

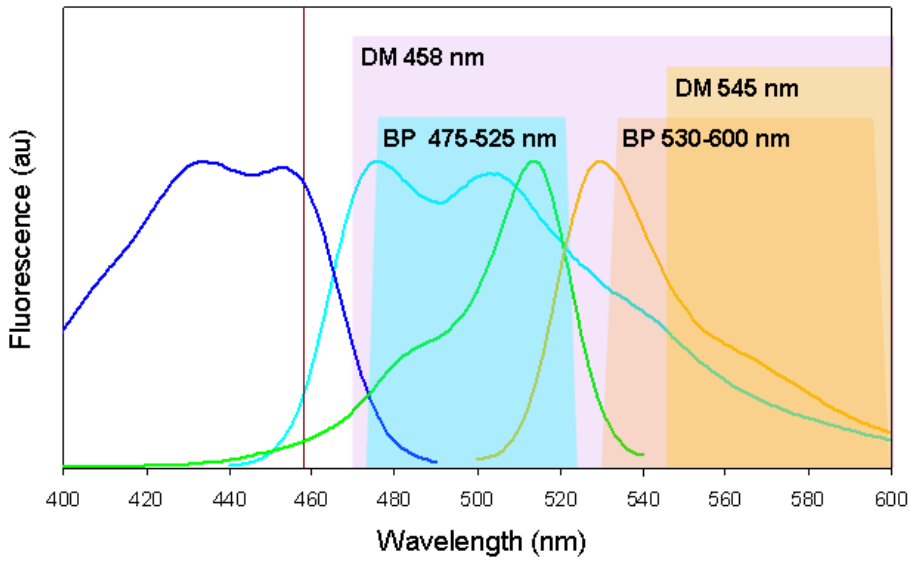

Figure 2.10: CFP-YFP spectra with the set of dichroicmirrors and filters used in the set up. To excite the donor, laser line 458 nm was used as shown the brown line. Dichroic 458 nm was used for passing the longer wavelength and reflects the shorter wavelength as shown in the purple area. For separtion the fluorescence, dichroic 545 nm was used which is not optimum. Beampass filters were used before detecting the CFP (475-525 nm) and the YFP (530-600 nm) emission by two PMT.

At a bleaching power of 4.1 µW, this number of iterations provided sufficient bleaching (up to 70%) of the acceptor YFP to observe increases in donor CFP fluorescence, whilst preventing the damage and increased auto-fluorescence observed at higher numbers (>2500) of iterations. DIC imaging and 458 nm scanning with was then repeated to acquire the post-bleach image set. Images were analysed in the open source image processing software Image-J (NIH, USA). Table 2.3 summarises the CFP and YFP peak excitation and emission wavelengths and the set of dichroic mirrors and filters that were used in the set up of dual channel confocal microscopy.

FP	Peak λ_{ex}	Laser Line	Dichroic Mirror	Peak λ_{em}	Bandpass Filter
CFP	434 nm	458 nm	458 nm	477 nm	475-525 nm
YFP	513 nm	514 nm	514 nm	527 nm	530-600 nm

Table 2.3: Set of laser line, dichroic, and beam pass filters for FRET (CFP-YFP) experiment.

Pre- and post-bleached image sets are processed to determine a measure of FRET by acceptor (YFP) photobleaching. The FRET efficiency in this case is formally given by the expression

$$E = 1 - \left(I_{DA} / I_{D} \right) \qquad 2.1$$

where E is the percentage efficiency of energy transferred, I_{DA} is the intensity of the donor in the presence of the acceptor; I_D is the intensity of the donor (CFP) in the absence of the acceptor (YFP). In practice the donor signal intensities I_{DA} and I_D will be only one of a number of contributions to the total intensities I_{TOT} measured in the pre- and post-bleached donor image. These contributions can be summarised in Equation 2.2

$$I_{TOT} = I_{DA} + I_{D} + I_{AD} + I_{A} + I_{AUTO} \qquad 2.2$$

where I_{AD} is the intensity contribution from the acceptor fluorescence on the donor channel due to sensitised emission in the presence of the donor, I_A is the fluorescence contribution from direct excitation of the acceptor at the donor CFP imaging wavelength 458 nm and I_{AUTO} is the cell autofluorescence background. In the pre-bleach CFP image, all components

can contribute to the total intensity to a greater or lesser extent, whilst in the post-bleach image contributions I_{DA}, I_{AD} and I_A will be expected to be significantly depleted and I_D enhanced for a system undergoing efficient FRET. In practice the photobleaching of acceptor YFP at 514 nm will in general be accompanied by a nominal level of bleaching of donor CFP as evidenced from control FRET experiments with single CFP-tagged RNR strains. For doubled-tagged RNR strains donor bleaching likely affects the free donor contribution I_D over that of the quenched donor undergoing FRET although these components are not readily resolved in the ensemble imaging experiments presented here. The discussion above leads to the conclusion that an increase in the fluorescence intensity in the CFP channel following acceptor photobleaching will only be observed if the fraction of donor CFP undergoing FRET is large compared to the free donor fraction and contributions from acceptor fluorescence either sensitised by FRET or directly by the 458 nm imaging wavelength. Given that the extent of YFP (and indeed CFP) photobleaching will be strongly dependent on the total dose of 514 nm excitation, uncertainties in the laser line intensity and net exposure time do not allow quantitative determination of the components contributing to the total intensity in the pre- and post bleach donor CFP image. As such we simply use FRET, strictly the measured donor CFP fluorescence enhancement following acceptor photobleaching, as a reporter of the Suc22-Cdc22 interaction rather than any quantitative measure of the proximity of the RNR subunits. For contributions $I_{D,}$ from non-interacting donor CFP and acceptor contributions I_A and I_{AD} in the pre-bleach image have been ignored, while in the post-bleach acceptor contributions I_A and I_{AD} along with the quenched donor contribution I_{DA} due to unbleached acceptor. In summary pre- and post-bleach image intensities are only corrected for the cell autofluorescence background, a "nominal" level determined from the untagged wild type Wt strain, and the "level" of FRET is given by

$$E = 1 - \frac{I_{PRE} - I_{AUTO}}{I_{POST} - I_{AUTO}} \qquad 2.3$$

where I_{PRE} and I_{POST} are the average fluorescence intensities in the pre- and post-bleach ROIs in donor CFP image. To more accurately compare pre- and post-bleach images, individual frames are first background subtracted before normalizing intensities in a non-bleached region of each image.

For comparison we also calculated FRET efficiencies using a dedicated Image-J macro developed by Stepensky *et al* for the method of FRET by acceptor photobleaching [109].

2.11. Materials and methods: the near-TIRF microscope

The near-TIRF technique was performed on a modified TIRF microscope. A standard inverted microscope (Nikon TE2000) was coupled to a mixed gas (Ar/Kr) ion laser (Spectra Physics 165 Spectra Physics Beamlock 2060-RM) that operates at the key wavelengths 457 nm and 514 nm for imaging CFP and photobleaching YFP of the double-tagged RNR strains of *S. pombe* described previously. The laser output was first circularly polarised to reduce in-plane or out-of-plane dipole excitation biasing. For imaging, the 458 nm beam was directed into the microscope *via* the TIRF lens, which focuses the beam at the back focal plane of the objective lens (100×, Nikon CEI, NA = 1.45), following reflection of a 458 nm dichroic (FF458-D01, Semrock, USA). The focused light was directed off the optical axis of objective lens to achieve the desired angle of refraction by a kinematic mirror. This allowed a

collimated and highly inclined beam (just below the critical angle for total refraction) to penetrate through the entire depth of the cell as a thin optical sheet (Figure 2.11). The fluorescence emitted from the sample is collected by the same objective lens and filtered through a longpass glass filter 475nm (475LP, Thorlabs., UK) before being separated into CFP and YFP fluorescence channels by the combination of a dichroic (540 DRLP, Omega Optics, USA) and mirror separated by an 'O'- ring spacer. The spacer is selected in thickness to project the shortpass emission that is reflected off the dichroic face into one half of a CCD array and the longpass emission reflected from the backing-mirror onto the other half of the imaging chip. The fluorescence (both CFP and YFP) is detected by an intensified charge coupled device (ICCD) camera (PImax 512F, Princeton Instruments, USA) that is controlled by open source ImageJ (NIH, USA) and μManager© (Vale Lab, UCSF) data acquisition software.

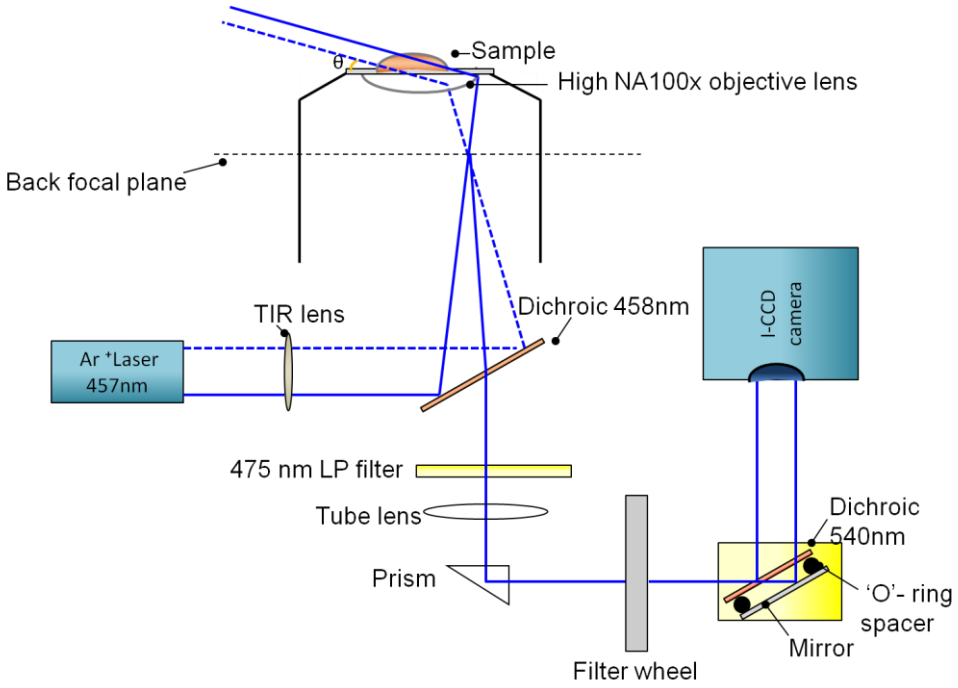

Figure 2.11: Schematic of the experimental set up of highly inclined illumination in near-TIRF

Chapter 3

FRET imaging of *S. pombe* RNR interactions

3.1 Introduction

Regulation deoxyribonucleoside triphosphates (dNTPs) pools for faithful DNA replication ultimately requires the formation of the ribonucleotide reductase (RNR) complex *via* the interaction of the Suc22 and Cdc22 subunits. The ability to tag these subunits with fluorescent proteins now allows the application of FRET spectroscopy to interrogate the Suc22-Cdc22 interaction directly, in vivo. Presented here are the results from analysis of the wild type (Wt), double-tagged library of *S. pombe* strains summarised in Chapter 2. FRET by acceptor photobleaching was applied in the first instance to Wt Suc22-CFP+Cdc22-YFP (Spd1+), primarily due to the strong nuclear localisation of the Suc22-CFP and hence identification of nuclei in the FRET reporting donor channel. The same experiments were repeated for single-tagged Suc22-YFP and Cdc22-CFP controls, to ensure the host protein had no influence on the generation of fluorescent byproducts that may affect the overall interpretation of positive FRET. For consistency, a swapped-tag system, Wt/Suc22-YFP-Cdc22-YFP, was used to examine the FRET level in both RNR-tagged strains in different cell cycle phases. The necessity to investigate the role of Spd1 as an inhibitor of RNR activity in various phases led to imaging and photobleaching experiments to be repeated on samples of Suc22-CFP+Cdc22-YFP *S. pombe* cells after deletion of Spd1. *S pombe* cells were also treated with different drugs such as Hydroxyurea (HU), which arrest the cell in the Sphase and 4 NitroQuinoline 1-Oxide (4NQO – Sigma), a DNA damage inducer, to investigate their effects on RNR activity with respect to Spd1.

3.2 Wt Suc22-CFP + Cdc22-YFP in the presence of Spd1.

A typical pre-bleach set of images is presented in Figure 3.1 which shows the brightfield DIC image and corresponding CLSM images on the CFP and YFP channels of donor-tagged Suc22 and acceptor-tagged Cdc22 *S. pombe* cells. The DIC image is obtained by illumination from a halogen lamp, the light from which is split or "sheared" by a Wollaston prism into two wavefronts that have different optical paths through the sample, resulting in a phase difference between the two paths and hence interference when the wavefronts are recombined by second prism. Image contrast then arises from regions of rapidly changing optical density, in this case at the interface between cytoplasm and the cell wall as seen in Figure 3.1a. Through the corresponding CFP fluorescence window (475-525 nm) shown in Figure 3.1b, cells with well defined nuclei are observed due to the presence of the Suc22 protein, which is largely (up to 90%) concentrated in the nucleolus by the import function associated with presence of Spd1 strains.

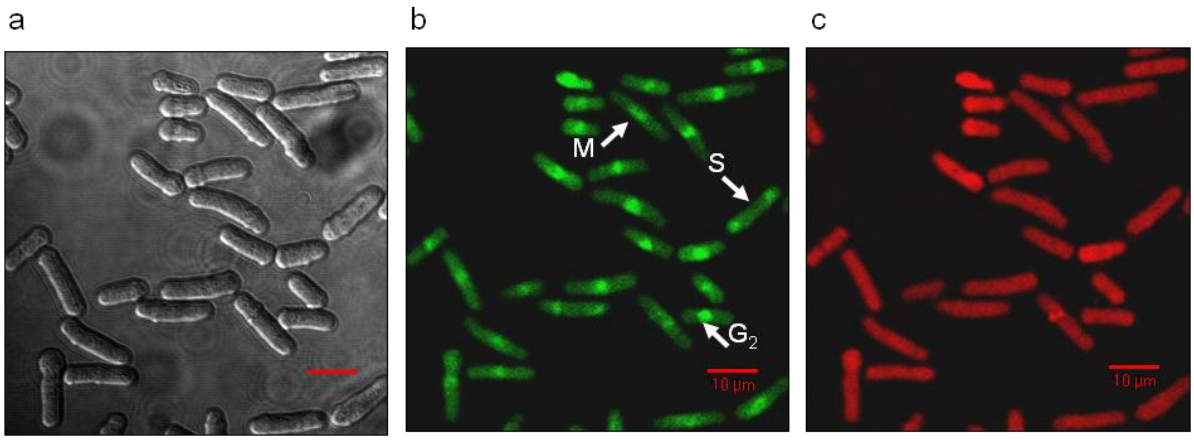

Figure 3.1: A typical image set of the *S. pombe* cells on different detection channels a) under brightfield DIC, b) the CFP window 475-525nm under 458nm excitation. Cells in states representative of the main phases of the cell cycle are highlighted. c) the corresponding YFP window 530-600 nm.

Cells representative of each phase of the cell cycle are labeled in Figure 3.1b. The YFP channel (530-600 nm) presented in Figure 3.1c shows the same cells with no nuclei

highlighted. In this case YFP-tagged Cdc22 is distributed near-uniformly throughout the cytoplasm. Of greatest interest is the distribution and interaction of Suc22 and Cdc22 in the DNA replication and segregation phase (S) at which Suc22 is expected to delocalise to the cytoplasm and form a mature and active RNR complex with Cdc22 and thus FRET activity between the Suc22-CFP and Cdc22-YFP might be expected to peak in this phase sub-units. The extent of Suc22 delocalisation can be gauged from a comparison between the nuclear and cytoplasmic CFP intensity ratio in the S phase and that of the pre-segregation G2 growth phase, while the formation of the RNR complex and its distribution, or at least the interaction between subunits over nanometre distances, is reported by the measurement of FRET. Figure 3.2 demonsrates a typical set of pre- and post-bleach CLSM images which contain cells in S phase, the G2 growth phase and "post-S" phase immediately following segregation.

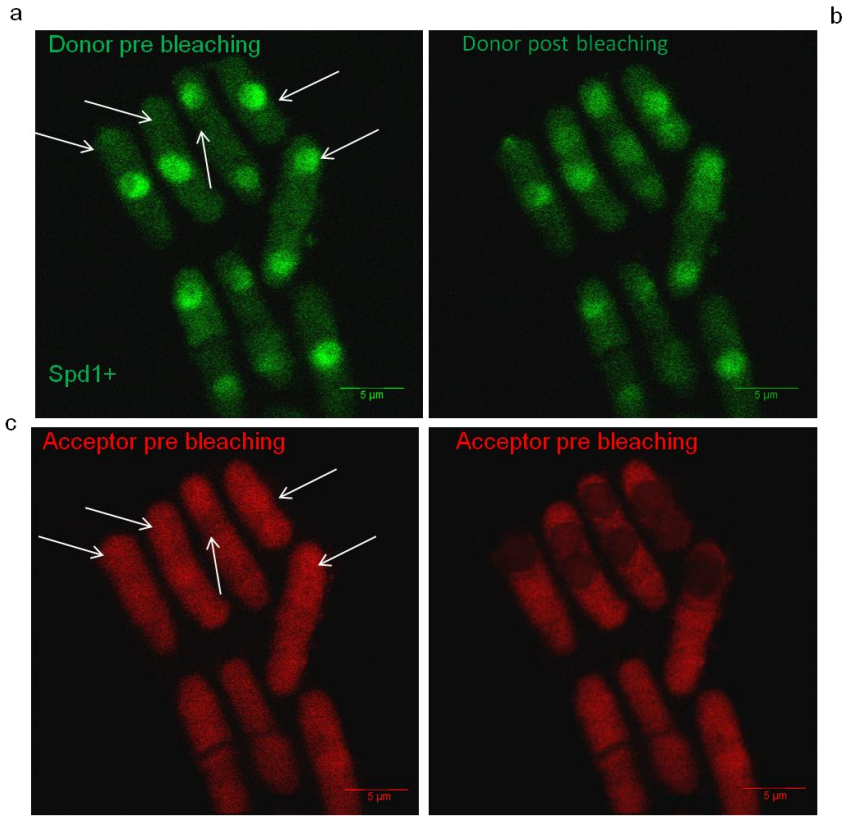

Figure 3.2: CFP and YFP images at 458 nm of tagged *S. pombe strain* prior to and following photobleaching of YFP at 514 nm. a) pre-bleach CFP. b) post-bleach CFP. c) pre-bleach YFP and d) post-bleach YFP

It is clear from the these images that on the CFP channel, the intensity of the donor in ROIs subjected to 514 nm laser illumination (identified by arrows) has increased as a result of acceptor (YFP) photobleaching, while on the YFP channel a decrease in the intensity of the acceptor is observed for the same area. Furthermore, a qualitative comparison of between G2, S-phase cells in the pre-bleach CFP images shows the expected trend in the redistribution of Suc22 in the cell, as indicated by highly localised, bright CFP fluorescence in G2-nuclei with weak CFP fluorescence in the cytoplasm and a depleted CFP fluorescence intensity in S phase nuclei with stronger fluorescence from delocalised Suc22-CFP in the cytoplasm.

To provide a more quantitative "picture" of FRET throughout the cell and to provide more accurate measurements of FRET efficiencies, a number of macros were developed in ImageJ. The first of these corrects for any frame shift that occurs between pre- and post-bleach images as was ocassionally observed, presumably due to a shift in the microscope stage position between acquisitions. By scanning the pre-bleach image over the post-bleach image and performing the logical AND operation between the two images at each image off-set the optimum overlap between cells pre- and post-bleached cells was determined from the AND image with maximum overall intensity. A second macro allows normalisation of the images, first by subtracting any background noise measured in a ROI away from the cells and then by scaling the pre-bleach image intensity to match that of the post-bleach image in a ROI containing fluorescence but well away from an photobleached areas. A final macro then subtracts the pre-bleach from the post-bleach and normalises the resulting FRET image to the post-bleach (donor only) fluorescence image, to map FRET efficiencies cross the cells.

Figure 3.3 shows corresponding map of the FRET efficiency obtained from the pre- and post-bleach images contained in Figure 3.2.Clearly –ve FRET efficiencies are physically meaningless and arise where the post-bleach pixel intensities are less than the corresponding pre-bleach pixel intensity. In regions where CFP is not undergoing FRET but the area is

subjected to YFP photobleaching, this will correspond to the incidental bleaching of CFP. However, it is clear from the post-bleach YFP channel in Figure 3.2d that unbleached cells show some modulation in the corresponding FRET effeciency between typically 0.2 and -0.2 which arise from differences in the image intensities despite normalisation. Additional smoothing and Fourier transform filtering techniques could be applied to reduce these fluctuations, but here the FRET map serves only to provide a rapid identification of +ve FRET hotspots, while the range of apparent transfer efficiencies in unbleached regions provides a level of error in the calculated FRET.

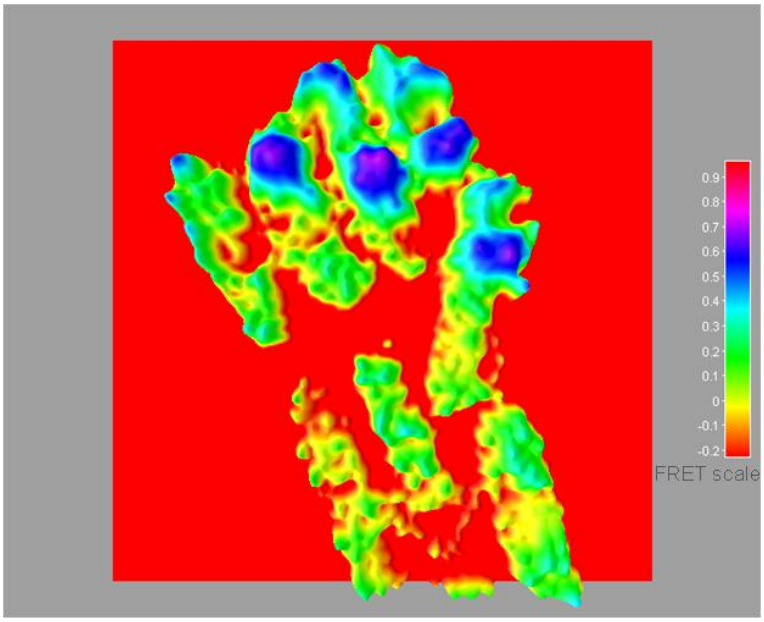

Figure 3.3: Three dimensions (3D) Surface plot display of the normalized image between CFP pre and post of Figure 3.2. It is clear that the bleached regions which have got an increase in the intensity are represented by the blue hot spots while the regions got a decrease in the intensity are represented in the holes. The plot indicates FRET level as well as gives an idea of the background that is produced from the normalisation process.

3.3 Analysis of single FP-tagged RNR control strains

In order to confirm the increase in CFP fluorescence is due to a genuine FRET interaction between and CFP and YFP and not due to some photophysical change induced by

the 514 nm bleaching laser acting on either of the fluorescent proteins, which may lead to enhancement in the CFP channel, CLSM imaging and photobleaching experiments were repeated on control samples. *S. pombe* cells transformed with only Suc22-CFP, Suc22-YFP and separately with Cdc22-CFPand Cdc22-YFP were used as controls and wild type untagged-cells were also examined to ensure there was no enhancement from autofluorescence. All controls showed a decrease in the intensity of the donor after bleaching. Examples of pre- and post-bleached images for a selection of single-tagged and untagged cells are shown in Figures 3.4-3.8.

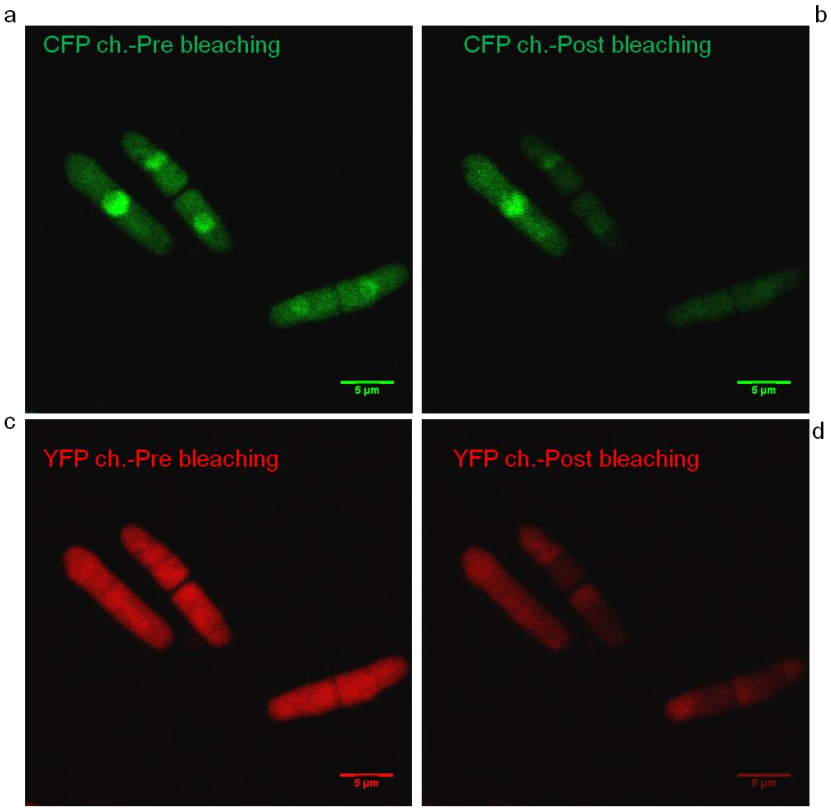

Figure 3.4: The effect of photobleaching on CFP tagged Suc22 *S. pombe* Cell, a) Pre-bleached CFP, b) Post-bleached CFP, c) Pre-bleaching of the bleed through of CFP in the 530-600 nm channel and d) Post-bleaching of the SBT of CFP.

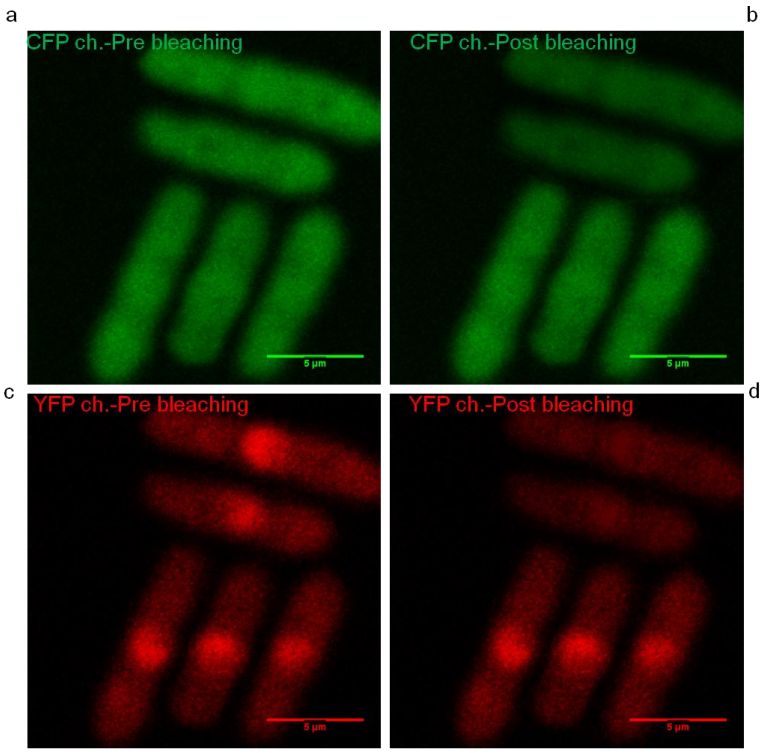

Figure 3.5: The effect of photobleaching on YFP tagged Suc22 *S. pombe* Cell, a) Pre-bleached CFP, b) Post-bleached CFP, c) Pre-bleaching of the SBT of CFP in the 530-600 nm channel and d) Post-bleaching of the SBT of CFP.

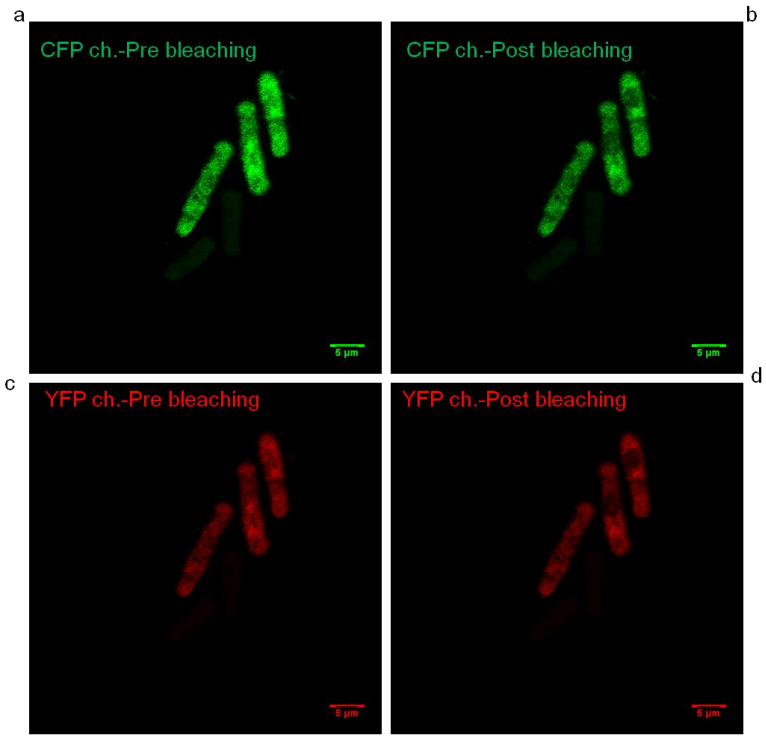

Figure 3.6: The effect of photobleaching on CFP tagged Cdc22 *S. pombe* cell. a) Pre-bleached on CFP ch, b) Post-bleached on CFP ch., c) Pre-bleaching of YFP on the YFP ch. and d) Post-bleach of YFP on YFP ch.

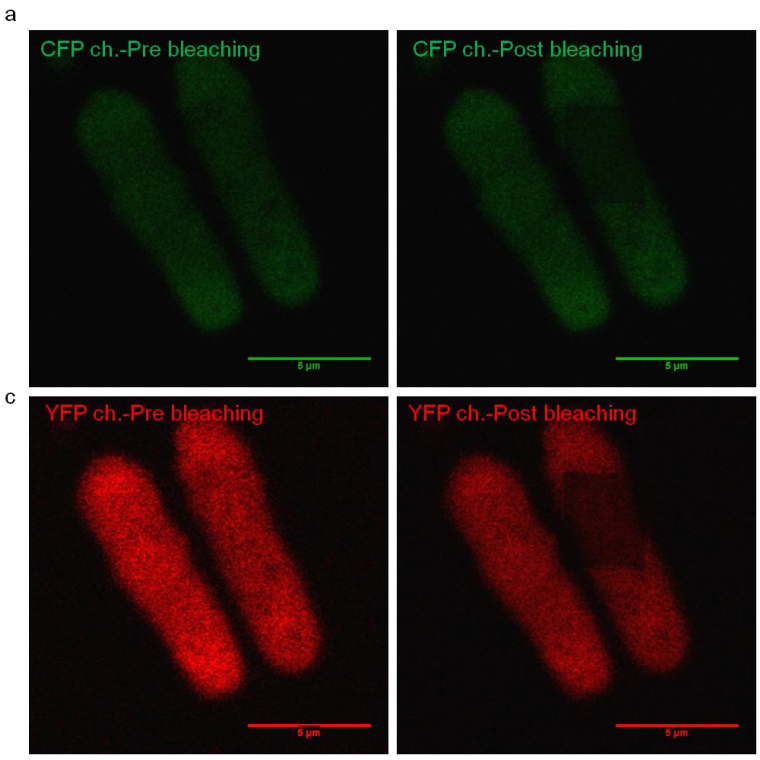

Figure 3.7: The effect of photobleaching on CFP tagged Cdc22 *S. pombe* cell. a) Pre-bleached on CFP ch, b) Post-bleached on CFP ch., c) Pre-bleaching of YFP on the YFP ch. and d) Post-bleach of YFP on YFP ch.

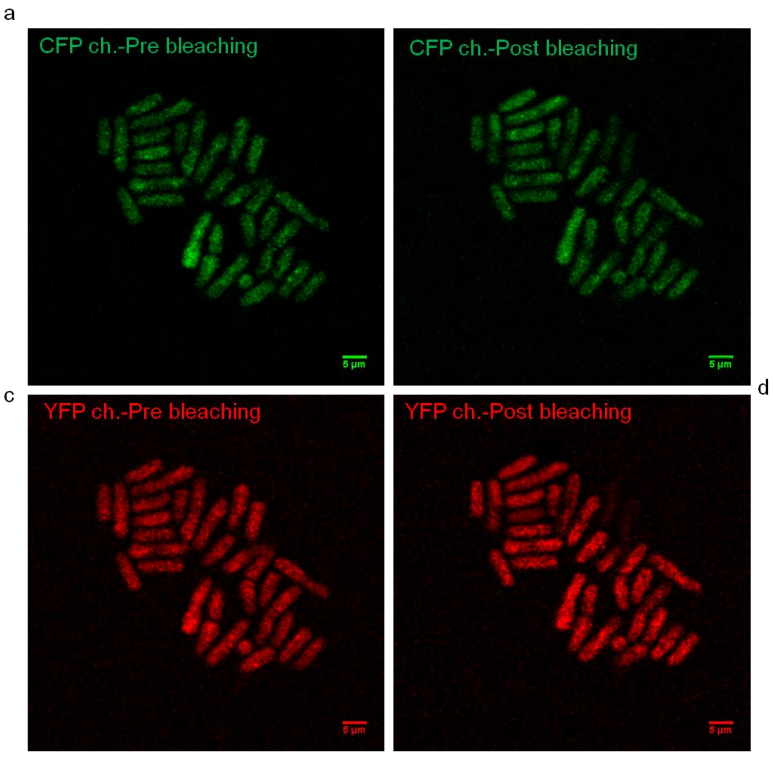

Figure 3.8: The effect of photobleaching on untagged *S. pombe* cell. a) Pre-bleached on CFP ch, b) Post-bleached on CFP ch., c) Pre-bleaching of YFP on the YFP ch. and d) Post-bleach of YFP on YFP ch.

In this case spectral bleed through or crosstalk of CFP signal on the YFP channel is generated from CFP emission spectrum (the long wavelength wing of the CFP fluorescence profile) overlaps to that of YFP spectrum in addition to that there is also bleed through of the YFP signal into CFP channel resulted from the same reason. Since this overlapping is quite extent whereby corrections by filter design are not easy [110]. It is important to emphasise here that the contrast and brightness has been adjusted for presentation purposes only and in fact the CFP intensity ratio in the short wavelength and long wavelength channels is about 6 to 1 from a calculation made with the mixed cell images (mixture of double-tagged cells, single-tagged cells and Wt). Importantly, all controls show a clear reduction in CFP intensity on both CFP and YFP channels (Figures 3.4-3.8).

Experiments were also performed on single-tagged Suc22-YFP and Cdc22-CFP controls, to ensure the host protein had no influence on the generation of fluorescent byproducts that may affect the overall interpretation of positive swapped double-tagged, Wt/Suc22-YFP+Cdc22-YFP, FRET images discussed in the next section. Post-bleach images of both single-tagged controls exhibited decreases in both CFP and YFP channel fluorescence consistent with the equivalent Suc22-CFP and Cdc22-YFP only controls. The results indicate that the fusion protein or its compartmentalisation, in either the nucleus or cytoplasm, has negligible influence on the ability to photobleach YFP and that no unfavourable fluorescence enhancement is produced on the FRET reporting, CFP channel following the photobleaching of single-tagged FP-subunit proteins.

It is evident from the levels of CFP and YFP fluorescence that both Cdc22 and Suc22 persist throughout the cell but with a significant concentration of Suc22-CFP in the nucleus in both S and G2 phases. For this purpose, the fluorescence microscopy has been used to measure the relative fluorescence intensity between Cdc22 and Suc22. Suc22 fluorescence was approximately three fold more intense in the nucleus than the cytoplasm in G2 phase,

with 74% of the signal residing in the nucleus (Figure 3.9). In S phase, nuclear Suc22 fluorescence is divided between two nuclei and comprises 26.5% of the CFP-Suc22 signal. By comparing with G2 phase, each nucleus shows individually a significant loss of intensity and corresponding gain in intensity (from 26% to 63.5%) in the cytoplasm.

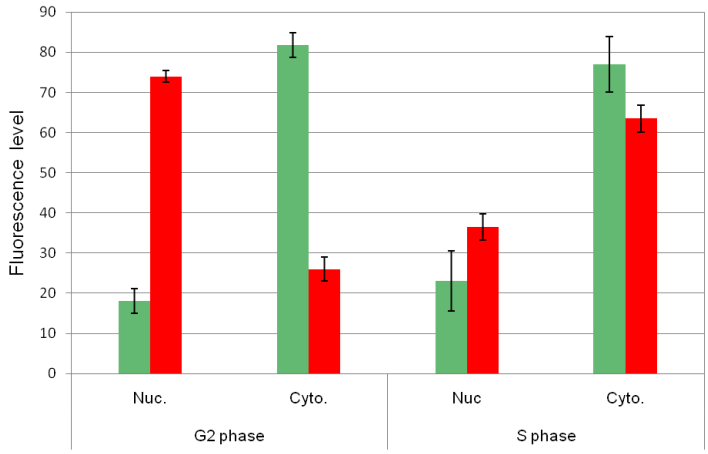

Figure 3.9: Percentage of nuclear and cytoplasmic fluorescent intensity of Cdc22-CFP (green) and YFP-Suc22 (red) in single tagged cells visualized under the same microscope slide for apopulation more than 60 cells .

3.4 Wt Suc22-YFP + Cdc22-CFP in an Spd1+ background

To investigate the behaviour of the fluorescence protein tag and its potential influence on the Suc22-Cdc22 RNR subunit interaction, FRET experiments on swapped tagged *S. pombe* strains expressing Suc22-YFP and Cdc22-CFP were performed. Results from FRET experiments on this system were found to be highly consistent with the Suc22-CFP+Cdc22-YFP system on which FRET was originally demonstrated for the first time. Figure 3.7 shows a selection of tagged *S. pombe* cells in G2 and early S phases. In the pre-bleached images, localisation of the Suc22 appears on the 530-600 nm channel and Cdc22-CFP appears delocalised as expected on the 475-525 channel. From the post-bleach images presented it is

clear that on the CFP channel, the intensity of the donor in cells subject to photobleaching has increased, while identification of the bleached cells is clear from a comparison between pre- and post-bleach YFP channel images.

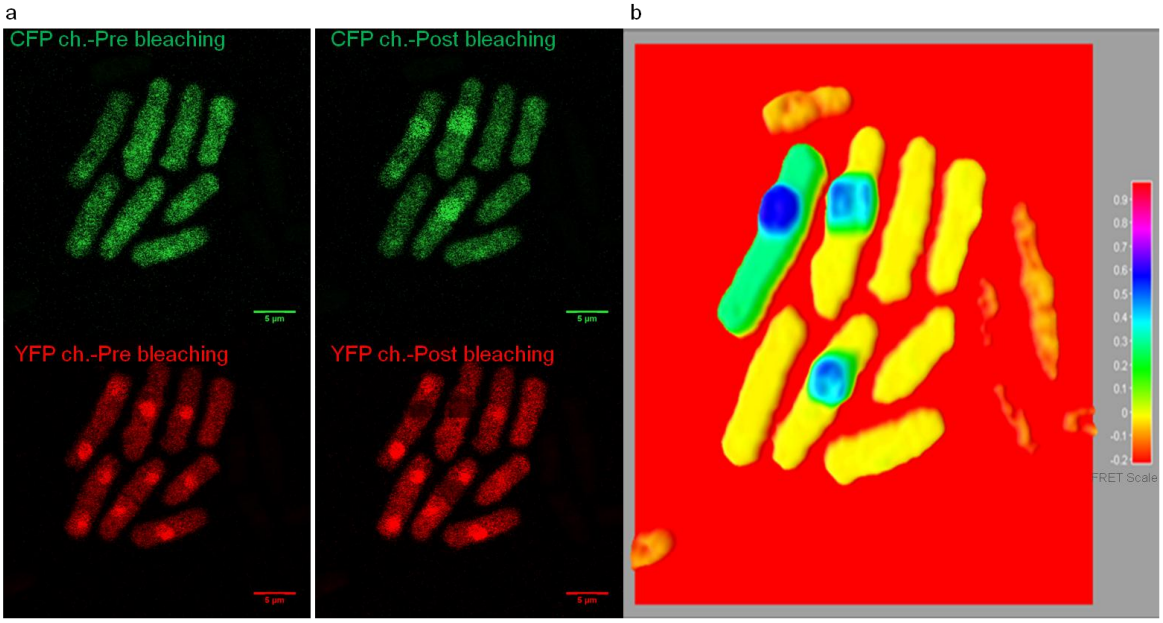

Figure 3.10: a) Double tagged strain, Suc22-YFP-Cdc22-CFP, images at 458 nm of tagged *S. pombe* prior to and following photobleaching of YFP at 514 nm.. b) Surface plot display of the normalized covariance image between pre and post CFP.

3.5 FRET comparison between double-tagged RNR strains

Quantitative analysis of the CLSM images is performed within the ImageJ software environment, the results of which are presented for a number of individual cells (S phase) in Table 3.1. It is evident from the results that our simple approach to estimating the FRET efficiency, following background subtraction and normalization of fluorescence intensities outside the bleached region of interests, ROIs, shows good comparison with that of the FRETcalc plugin. The plugin is designed primarily for analyzing cells with complex non-continuous shapes, such as intra-cellular tubuli, which in general will not extend (or fill) a

regular shaped ROI that is bleached. In this instance a threshold is used to eliminate any unlabelled space within the ROI that should not contribute to any FRET determination. In our case, the tagged RNR protein sub-units Suc22-CFP and Cdc22-YFP extend uniformly throughout the ROIs that are bleached, whether in the nucleus or cytoplasm. In essence the threshold set in FRETcalc is equivalent to the background subtraction made in our simplified approach. The fluorescence intensities I_{DA} and I_D are then averaged over only those pixels above threshold but ultimately the same FRET calculation [E=1-(I_{DA}/I_D)] is performed. Since the CFP intensity across the ROI in both pre- and post-bleached images does not drop below threshold, all pixels are included in the calculation of I_{DA} and I_D, in the same way that the average is performed over the entire ROI in our simplified approach [109]. The accumulation number of cells that have been used here is more than 300 cells .

S phase										
	Nuc.1	**Cyto.1**	**Nuc.2**	**Cyto.2**	**Nuc.3**	**Cyto.3**	**Nuc.4**	**Cyto.4**	**Nuc.5**	**Cyto.5**
a) FRET *basic*										
I_{DA}	123.1	96.4	127.4	148.8	84.8	59.2	133	57.7	*151*	58.5
I_D	131.9	135.6	129.1	213.4	118.4	120.9	138.2	111.6	144.2	108
E	**7.1**	**33.2**	**1.23**	**38.8**	**18.7**	**49.34**	**3.75**	**39.6**	**-4.45**	**32**
b)* FRET *calc										
I_{DA}	128.8	146.1	129.4	160.4	195.1	190.8	195.5	137.8	146.3	184
I_D	118.2	78.1	125.2	68.9	89.3	39.3	59.3	126.3	144.3	115
E	**6.24**	**39.4**	**2.82**	**38.4**	**24.2**	**48.3**	**7.24**	**50.2**	**-0.74**	**40.3**

Table 3.1: FRET calculations for *S. pombe* cells (Wt/Suc22-CFP-Cdc22-YFP) applying a) FRETbasic a simple background subtraction and normalization to measurement, I_{DA} and I_D b) the open source FRETcalc ImageJ plugin of Strepensky [109].

S phase										
	Nuc.1	**Cyto.1**	**Nuc.2**	**Cyto.2**	**Nuc.3**	**Cyto.3**	**Nuc.4**	**Cyto.4**	**Nuc.5**	**Cyto.5**
FRET *basic*										
I_{DA}	124.3	87.64	137.67	83.72	109.43	73.18	107.1	60.65	102.46	70.38
I_D	161.07	119.81	144	126.93	130.41	101.65	118.55	91.99	171.14	109.83
E	**24.23**	**29.6**	**4.2**	**37.5**	**17.4**	**31.8**	**9.9**	**39.5**	**42.9**	**40.3**
FRET *calc*										
I_{DA}	202.71	82.38	153.71	51.94	157.05	71.74	103.82	36.03	230.14	63.76
I_D	153.13	117.06	133.88	104.1	127.94	100.15	115.07	90.09	163.82	108.04
E	**23.7**	**34.17**	**5.7**	**40.9**	**20.51**	**33.48**	**8.97**	**43.1**	**45.42**	**39.8**

Table3.2: FRET calculations for the swapped systemof *S. pombe* cells (Wt/Suc22-YFP-Cdc22-CFP) for S phase, following same instructions made in Table 3.1

Tables 3.3-3.7. demonstrate a significant decrease in CFP emission upon photobleaching for the single-tagged Suc22-CFP, Suc22-YFP, Cdc22-YFP and cdc22-CFP strains in both S and G2 phases. This decrease is represented in the negative values of FRET derived the subtraction of post-bleached image from the pre-bleached image, similar results were found for Cdc22-YFP.

G2& S phase										
	Nuc.1	**Cyto.1**	**Nuc.2**	**Cyto.2**	**Nuc.3**	**Cyto.3**	**Nuc.4**	**Cyto.4**	**Nuc.5**	**Cyto.5**
FRET *basic*										
I_{DA}	121.1	96.4	136.4	48.8	81.56	59.2	133.3	111.7	99.4	110.23
I_D	99.9	75.6	94.1	39.4	61.4	34.9	98.2	94.6	79.45	101.76
E	**-45.2**	**-24.2**	**-51.44**	**-9.4**	**-39.41**	**-14.4**	**-55.17**	**-40.8**	**-30.4**	**-9.6**
FRET *calc*										
I_{DA}	118.8	106.1	119.4	76.4	65.1	50.8	105.5	137.8	80.5	99
I_D	78.2	58.1	74.2	69.9	39.3	39.3	59	126.3	65.3	89.4
E	**-46.24**	**-29.4**	**-48.82**	**-8.4**	**-29.2**	**-16.3**	**-58.24**	**-50.2**	**-29.4**	**-8.5**

Table 3.3: FRET calculations for single tagged sample, Suc22-CFP.

G2& S phase										
	Nuc.1	**Cyto.1**	**Nuc.2**	**Cyto.2**	**Nuc.3**	**Cyto.3**	**Nuc.4**	**Cyto4**	**Nuc.5**	**Cyto.5**
FRET basic										
IDA	100.3	88.3	102	66.5	73.8	93.8	98.6	101.3	106	76.4
ID	87.6	66.3	90.6	60.7	54.7	74.3	70.6	80.4	90.7	54.9
E	**-17.2**	**-41.9**	**-14.8**	**-12.3**	**-46.7**	**-32.2**	**-49.3**	**-31.4**	**-19.9**	**-52.4**
FRET calc.										
IDA	86.45	94.7	110.4	70.4	70.1	88.8	101.3	117.2	90.3	88.9
ID	76.6	69.6	99.6	64.9	51.9	70.6	73.6	90.9	79	64.8
E	**-15.7**	**-45**	**-12.5**	**-10.7**	**-47.8**	**-32.1**	**-46.3**	**-34.1**	**-17.3**	**-47.3**

Table 3.4: FRET calculations for single tagged sample, Suc22-YFP

G2& S phase										
	Nuc.1	**Cyto.**	**Nuc.2**	**Cyto.**	**Nuc.3**	**Cyto.**	**Nuc.4**	**Cyto.**	**Nuc.5**	**Cyto.**
FRET basic										
IDA	82.6	108.3	82	76.4	103.8	98.1	118.2	112.7	98.5	84.2
ID	57.6	86.3	60.6	50.2	94.7	79.2	103.6	97.2	77.9	67.3
E	**-57.1**	**-30.3**	**-45.8**	**-72.1**	**-11.2**	**-28.9**	**-16.2**	**-18.6**	**-32.1**	**-31.6**
FRET calc										
IDA	103.9	89.9	115	80.3	98.6	96.9	113	98.5	104	90.8
ID	69.9	65.1	80.5	57.2	88	80.1	99.5	84.9	83.1	73.9
E	**-60.6**	**-48.4**	**-51.7**	**-53.3**	**-14.3**	**-25.3**	**-15.7**	**-19.1**	**-30.1**	**-28.1**

Table 3.5: FRET calculations for single tagged sample, Cdc22-YFP

G2& S phase										
	Nuc.1	**Cyto.1**	**Nuc.2**	**Cyto.2**	**Nuc.3**	**Cyto.3**	**Nuc.4**	**Cyto.4**	**Nuc.5**	**Cyto.5**
FRET basic										
IDA	102	89.5	108.1	121.3	110.8	86.9	92.8	92.2	102	101.7
ID	74	79.6	95.6	107.6	95.1	73.8	70.7	72.9	80.1	86.9
E	-46.5	-15.9	-15.2	-14.6	-19.3	-21.8	-38.8	-32.7	-33.1	-20.2
FRET calc										
IDA	98.7	84.8	110	98.6	95.1	83.8	96.9	98.1	112.9	100.4
ID	72.6	76.4	95.7	89.7	80.3	70	73.9	77.8	86.9	87.8
E	**-44.8**	**-13.4**	**-17.4**	**-11.7**	**-22.2**	**-24.5**	**-38.3**	**-31.7**	**-35.6**	**-17.5**

Table 3.6: FRET calculations for single tagged sample, Cdc22-CFP

G2& S phase										
	Nuc.1	**Cyto.**	**Nuc.2**	**Cyto.**	**Nuc.3**	**Cyto.**	**Nuc.4**	**Cyto.**	**Nuc.5**	**Cyto.**
FRET basic										
IDA	45	33	29.7	35.4	19.7	24.2	42.6	36.3	28.5	36.5
ID	30	20	18.4	22.7	10.7	18.6	32.9	30.4	16.8	27.8
E	**-30.6**	**-25.9**	**-12.2**	**-19.5**	**-30.1**	**-19.1**	**-28.2**	**-10.4**	**-40.4**	**-17.9**
FRET calc										
IDA	44.5	37.5	31.6	37.5	21.7	30.1	45.6	39.5	34.7	40.7
ID	31.6	24.8	20.6	26.7	15.5	23.7	37.8	33.7	20.1	29.7
E	**-32.4**	**-24.4**	**-17.4**	**-21.1**	**-32.6**	**-22.1**	**-29.3**	**-11.5**	**-42.6**	**-17.4**

Table 3.7: FRET calculations for wildetype untagged sample of *S.pombe* cells (Wt/Cdc22- Suc22).

The calculations here do not take into account Spectral Bleed Through (SBT) of YFP, $I_{A(SBT)}$ in the CFP channel or the contribution from "free" CFP $I_{D(FREE)}$ that is not undergoing the FRET that is associated with the interaction of Cdc22-CFP with Suc22-YFP. Absolute calculations of FRET efficiencies by acceptor photobleaching require the use of the following corrected intensities:

$$I_{DA(FRET)} = I_{DA} - I_{D(FREE)} - I_{A(SBT)} - I_{AUTO} \quad 3.1$$

$$I_{D(FRET)} = I_{D} - I_{D(FREE)} - I_{A(SBT)} - I_{AUTO} \quad 3.2$$

where $I_{DA(FRET)}$ is the intensity of only those donor molecules actually undergoing FRET in the presence of the acceptor and $I_{D(FRET)}$ is the intensity of the same molecules following photobleaching assuming all acceptor is bleached and I_{AUTO} is the cell autofluorescence background. The calculations here represent changes in donor emission due to different

relative levels of FRET between the *S. pombe* nucleus and cytoplasm but not an absolute measurement of FRET.

By accumulating a large number of FRET images spanning more than 60 cells representative of the S phase of the cell-cycle and 60 cells in the G2 phase and interrogating both the cytoplasm and nucleus for FRET in each case, averages and standard deviations over the population were determined as presented in Figure 3.8. Cells in the G2 phase reported a percentage of FRET efficiency of 35±3.9 in the cytoplasm and 9±3.2 in the nucleus whereas for S phase; 38±3.1 and 19±4.2 for both cytoplasm and nucleus respectively.

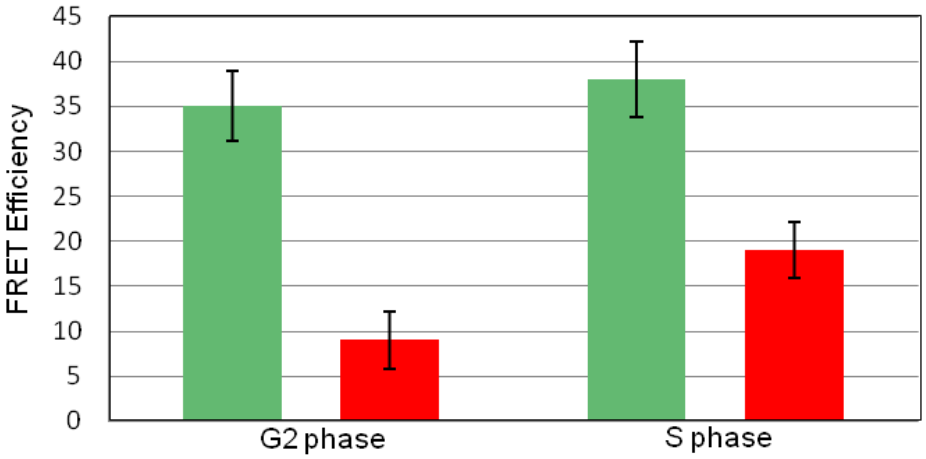

Figure 3.11: FRET efficiency of the RNR in different phases and compartments . Where the red bars represent the %FRET effiiceny in the Nucleus while the green bars represent the FRET level in the cytoplasm

3.6 Wt Suc22-CFP/YFP + Cdc22-YFP/CFP in the absence of Spd1

To investigate further the role of Spd1, imaging and photobleaching experiments were repeated on samples of Suc22-CFP+Cdc22-YFP *S. pombe* cells after deletion of *spd1*. The nuclear localisations were undetected in these samples under fluorescence microscopy as

shown in Figures 3.12-3.13, giving a typical Suc22 pan-cellular phenotype under the microscope. This result correlates with the biochemical data provided by Nestoras *et al.*[63].

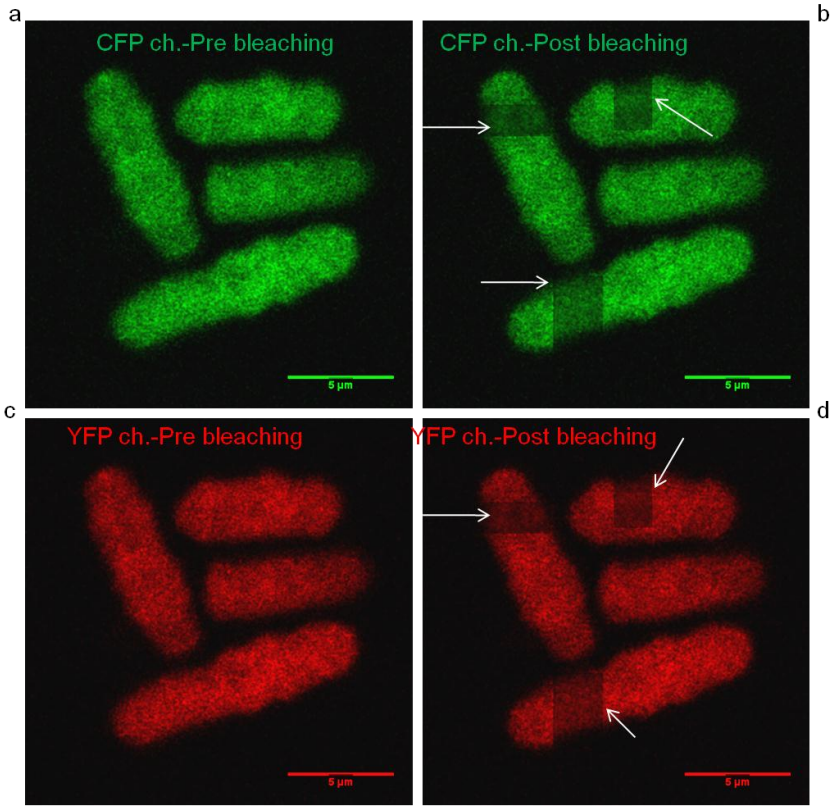

Figure 3.12: Suc22-CFP- Cdc22-YFP images at 458 nm of tagged *S. pombe* after deleting *spd1* prior to and following photobleaching of YFP at 514 nm. a) Pre-bleached on CFP ch, b) Post-bleached on CFP ch., c) Pre-bleaching of YFP on the YFP ch. and d) Post-bleach of YFP on YFP ch.

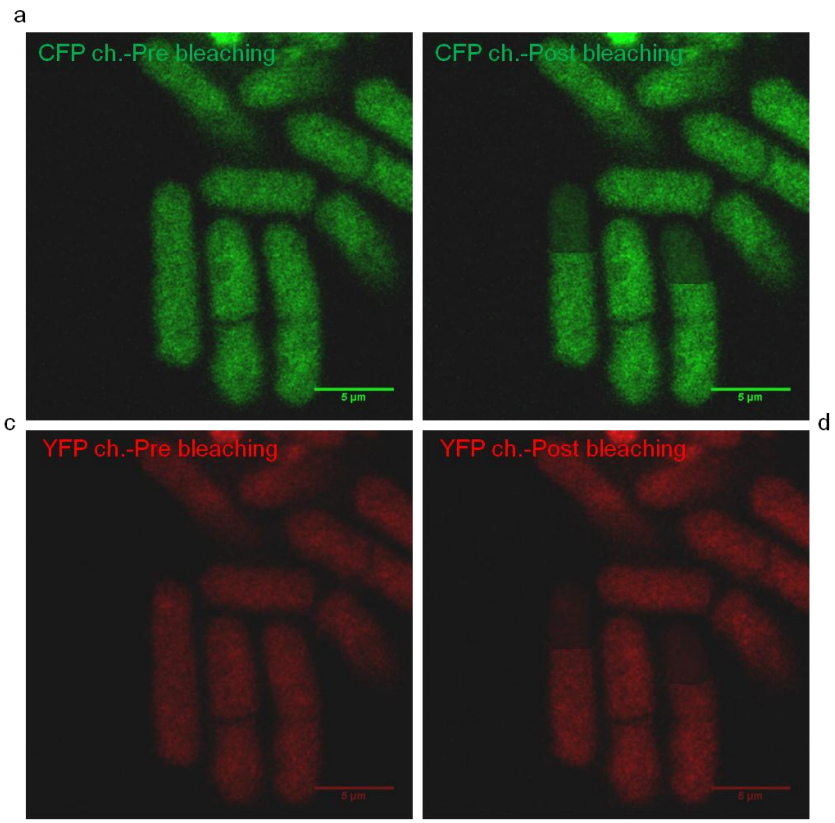

Figure 3.13: Suc22-YFP-Cdc22-CFP images at 458 nm of tagged *S. pombe* after deleting *spd1* prior to and following photobleaching of YFP at 514 nm. a) Pre-bleached CFP ch., b) Post-bleached CFP ch., c) Pre-bleached YFP ch and d) Post –bleached YFP ch.

3.7 Analysis of the effects of HydroxyUrea (HU) and 4-NitroQuinoline 1-Oxide (4NQO) on RNR interactions

Hydroxyurea (HU), chemical formula CH_4N_2O, is a potent agent that inhibits RNR and synchronizes cells in S phase. When Wild-type *S pombe (*both presence and absence of *spd1)* cells were treated with 20 mM of HU for 4 hours, the cell-cycle progression was arrested in response to a DNA replication block, but the cell continues to survive with a typically elongated phenotype as seen in Figure 3.14. Hydroxyurea inactivates RNR by destroying or quenching the free radical in the active site of the enzyme, in this case the tyrosil radical in the small subunit (Suc22) of RNR, and thereby depletes the pool of deoxyribonucleoside

triphoshate (dNTPs) [57]. It is important to emphasize here that HU has been used in chemotheraptic as a drug for cancer treatment, e.g. chronic myeloide leukemia. HU inhibits RNR (a target for cancer therapy) which precludes DNA transcription and repair that ultimately leads to cell death (apoptosis) [111].

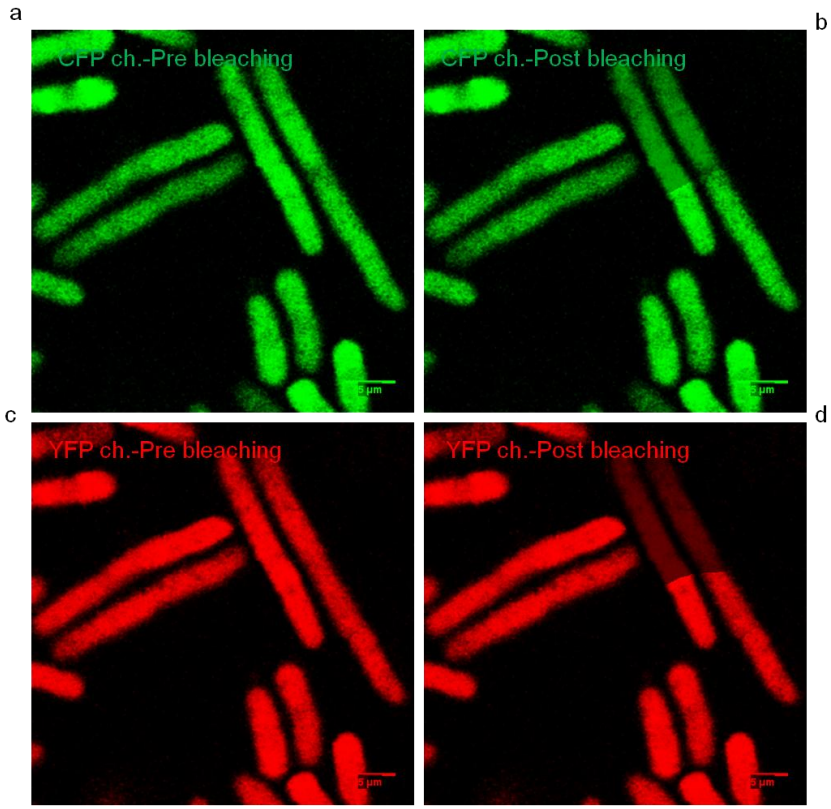

Figure 3.14: The effect of HU on the *S. pombe* cells. a) Pre- bleached CFP ch., b) Post-bleached CFP ch., c) Pre-bleached YFP ch and d) Post –bleached YFP ch.

FRET was inhibited (post-bleach images) for cells treated with HU compared to the equivalent untreated Wt double-tagged cells. The assumption here is that the lack of donor enhancement following photobleaching of acceptor is the result of some sort of changes in the RNR complex that prevents the FPs of the respective subunits from undergoing FRET, and ultimately the cells behave like *spd1::ura4+*. A number of possibilties can be envisaged for this lack of a FRET response: The generation of the tyrosil radical requires the oxidation

of the di-iron centre of the R2 active site from Fe^{2+} to Fe^{3+}. Changes in sizes of these ions may provide some conformational change in the R2 subunit and an allosteric effect on RNR activity [47,56,58,86,107,112]. Relative positions and/or dipole orientations of the FP tags of Suc22 and Cdc22, that favours FRET. An alternative posibility that may result in a similar outcome include the possible oligomerization of the RNR complex. Studies of mouse and *E coli* RNR showed possible formation of large oligomeric complex [113-114]. Nestoras group observed on the size exclusion column a higher order of protein complex resulted from cells treated with HU, however is not a direct evidence [63]. Oligomerization complex may lead to aggregation of the FP tags leading to possible self-quecching. Another possibility is that the same radical quenching properties of HU acts to quench directly the excited states of the FPs tags. There is also the possibility of a second Suc22 transcript to be involved and ultimately leads to a different complex.

In order to confirm that the effect of HU on the FRET signal was due to the direct effect of the HU on the RNR in S phase, Nestoras *et al*. [63] crossed cdc25-22, a check point mutant that block the cell in G2 phase, with RNR tagged strains and then treated with HU. Similarly FRET was undetactable , this reflects that S phase is independent of HU effect. Interestingly, in the case of treating *S. pombe* with the DNA damage inducing drug, 4 NitroQuinoline 1-Oxide (4NQO, Sigma)at 5 μM for 4 hours, Suc22 remained mainly in the nucleus in contrast to HU, FRET levels were maintained at comparable levels to those in untreated double-tagged Wt (presence of *spd1*) cells (Figure 3.14).

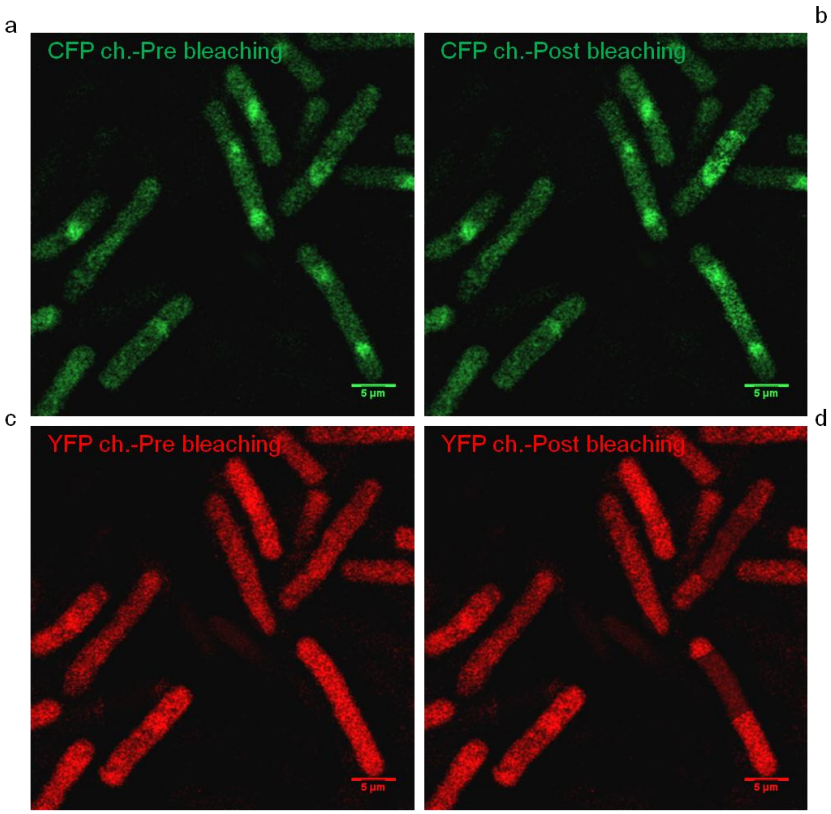

Figure 3.15: The effect of 4NQO drug on the *S. pombe* cells in the presence of Spd1. a) Pre-bleached CFP ch., b) Post-bleached CFP ch., c) Pre-bleached YFP ch and d) Post –bleached YFP ch.

A summary of FRET levels across a large population of cells, for all experiments performed on Wt double-tagged strains in the presence of Spd1protein and *spd1* deleted backgrounds and also HU and 4NQO treated samples is presented in Figure 3.15.

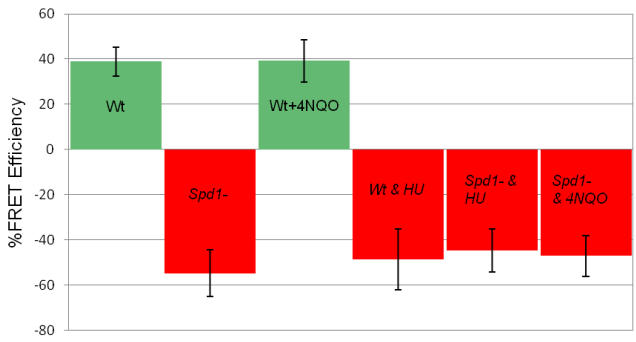

Figure 3.16: FRET efficiencies of Spd1+ and *Spd1::ura4* strains, without and with treatment of HU and 4NQO.

3.8 FRET of the RNR after heat shock.

The transcriptional response to heat shock is conserved in eukaryotes organisms, and is controlled by a heat shock factor (HSF). In *S. pombe*, this transcription factor is essential for growth [46]. It has been reported that the Suc larger transcript of Suc22 is highly induced after heat shock (42°C), while Cdc22 transcripts are reduced [115]. This strong induction of Suc22 has been demonstrated to be part of a separate pathway from that of DNA damage repair (*rad1* independent). The aim here, was to see how heat shock affected the RNR complex formation and FRET. This was undertaken, in brief, by growing in parallel RNR double-tagged strains with the presence of Spd1 and *spd1::ura4+* at 30°C and separately at 42°C for 145 min after which the heat shock culture was shited back to 30°C *spd1::ura4+* strains was observed to show no FRET, as might be expected, but in the presence of *spd1* strain displayed some curious results. The culture maintained at 30°C had a constant FRET efficiency whereas the 42°C culture showed a slow increase in the FRET level in aliquots measured at time intervals over the course of the 145 min incubation. The higher FRET level was lowered concomitantly with the cooling of the culture. The phenomenon was especially pronounced in S Phase cells. Histograms were build up for results at 30°C and 42°C (Figure 3.15 a). The rise in FRET must reflect a "stronger" Suc22-Cdc22 interaction, either in a conformation whereby the FPs are closer or more favourably aligned for FRET and/or the population of FRET efficient complexes rises with temperature. Whether the rise is correlated with increased dNTP pools and RNR activity remains to be tested. As it has previously been proposed that the active RNR complexes is allowed to form when dNTPs are required [47, 57- 58,106,112,133]. Histograms in Figure 3.14a, reflect the FRET data at 30 °C and 42 °C for S phase (nucleus and cytoplasm), while Figure 3.14b shows percentage of FRET for G2 phase at 30°C and 42°C in both RNR compartments.

a

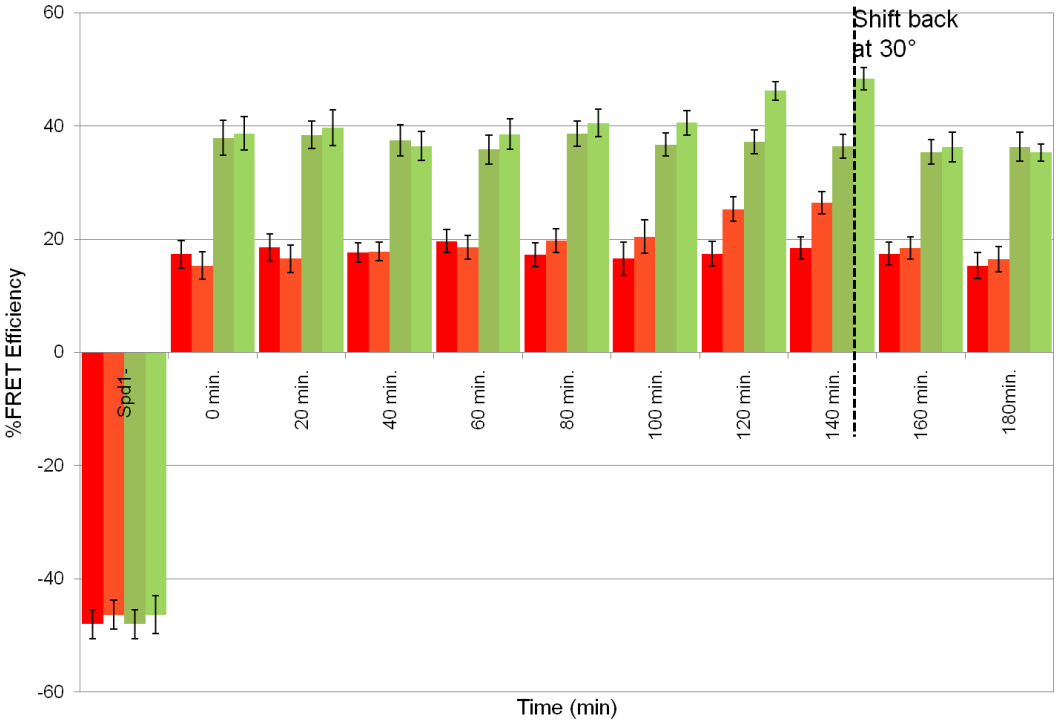

b

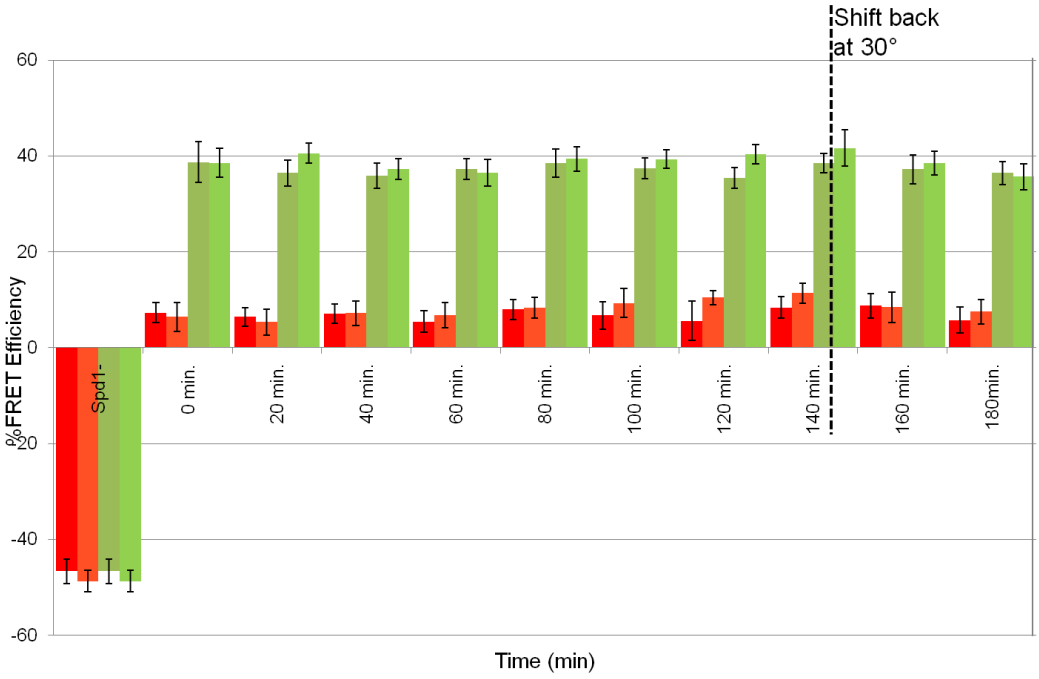

Figure 3.17: FRET efficiencies of the RNR after heat shock. a) FRET histogram for Wt *S pombe* cells in the S phase in both nucleus(red bars) and cytoplasm (green bars) at 30 °Cand 42 °C , b) FRET in both nucleus and cytoplasmic in G2 phase at 30°C & 42°C.

3.9 Conclusions

In vivo, significant FRET levels (+ve FRET) were detected for RNR-tagged strains (both; Wt/Suc22-CFP-Cdc22-YFP and Wt/Suc-YFP-Cdc22-CFP) in both compartments (nucleus and cytoplasm) and in different cell-cycle phases (G2 and S phase) during which RNR is tightly regulated. Various single-tagged strains, Suc22-CFP/YFP and separately Cdc22-CFP/YFP, and wild type untagged-cells were examined to ensure there was no donor enhancement from photoinduced by products or autofluorescence.

Surprisingly, in S phase, the FRET level reported in the cytoplasm was found to be comparable to that in the G2 phase. The former phase (DNA replication) was predicted to have higher FRET signals due to delocalisation of Suc22 from the nucleus to the cytoplasm, as a result of Spd1 degradation, and hence an expected increased level of interaction with Cdc22 (formation of active complex due to the requirement of dNTPs) [47, 57,87,105,112]. Detected FRET levels in the nucleus in the S phase was found to be approximately double that in the G2 phase. Indeed the strongest changes in FRET were observed in the nucleus suggesting the component of the RNR regulatory pathway that induces, Cdc22 and Suc22 subunit interaction may be proliferate in the nuclei as well as the cytoplasm.

Spd1 is reported to be intrinsically disorderd protein (IDP) [117] and NMR studies reported that IDP tends to adopt folding onto its interaction partner during their association [117]. This process can take place in protein-protein interactions with low affinity but high specificity [118]. When Spd1 deletion, the nuclear localisations of Suc22 were undetected in the samples under fluorescence microscopy. Furthermore, both double-tagged RNR strains showed no FRET (-ve FRET) in both S and G2 phase and since FRET is an indicator of RNR interaction. Thus, Spd1 is also important in mediating

the Suc22-Cdc22 interaction in the formation of a FRET competent, but not necessarily active RNR complex.

2 When Spd1+ and *spd1::ura4+* cells were treated with HU, Cdc22-Suc22 FRET was also lost. When Wt (in the presence of Spd1) cells blocked in G2 and then treated with HU showed no FRET despite not progressing into S phase, indicating that HU may independently quench the FRET signal. Treating *S. pombe* cells with 4NQO, an inducer of DNA damage, nuclear localisation was largely detected and also FRET maintained in both nucleus and cytoplasmic compartments in both S and G2 phase as for the wild type double-taggged strain but only in the presence of *spd1*.

Chapter 4

FRET imaging of RNR under Spd1 mutation

4.1 Introduction

The evidence for the instrinsically disordered protein (IDP) Spd1 playing multiple roles in the regulation of RNR has been provided by the genetic studies of [63] and moreover the CLSM studies of both the single and double FP-tagged RNR strains with the presence os *spd1* and *spd1::ura4+* backgrounds, presented in Chapter 3. Most significantly with Spd1 deleted, cells exhibited a loss of R2 nuclear localisation and the loss of FRET efficient R1-R2 interactions, despite an RNR activity that maintained dNTP pools for DNA replication and passage through the cell-cycle. This was attributed to the inhibitory role of Spd1 mediating the Suc22-Cdc22 interaction to form a FRET competent but immature and inactive RNR complex, while with Spd1 deleted RNR is clearly active in an conformation that lacks FRET, presumbly due to some relative positional or orientational change in the donor/acceptor FP tags.

To further elucidate the roles of Spd1 in the regulation of RNR a collection of *S. pombe* strains containing the *spd1* gene mutations (41 of *spd1::ura4+* mutants) generated by Nestoras *et.al* [63] were analysed using CLSM and FRET. These 41 independent mutants scan the whole protein by site-directed mutagenesis in which every 3 amino acids have been substituted by three individual alanines as described in Chapter 2. Various domains of Spd1 protein which function independently have been examined. After crossing these mutants with the double-tagged strains of *S. pombe* (both Suc22–CFP+Cdc22-YFP and Suc22-

YFP+Cdc22-CFP) yeast cells were tested for their ability to promote FRET. The *spd1* mutants were treated with HU (block the cell in S phase and Spd1 degraded) and 4NQO (DNA damage inducer). Finally, data were analysed in relation to Wt doubled-tagged strains to provide further insight into the possible roles of Spd1 in the RNR regulation.

Spd1 has similar domains, found in the sequence-conserved *S. cerevisae* orthologues: Sml1, Dif1, Hug1. In these budding yeast, Dif1 promotes R2 nuclear import, during S phase or genotoxic stress, while its degradation activates nuclear export of R2 in the cytoplasm [62]. Spd1 in *S. pombe*, and Dif1 in *S. cerevisiae* were found to regulate nuclear localisation. In Dif1, it is the HUG domain through which Dif1 binds R2 [62-63] to promote R2 nuclear import and this appears to be conserved in Spd1. The role of Hug1 that also contains the HUG domain is not fully understood, however, its transcription is induced by DNA damage and it has been suggested that it controls RNR inhibition [64-65]. Spd1 also contains a similar R1 binding domain as that of Dif1 Sml1 upstream from the C-terminus [62-63,66]. The function of this domain is well known as inhibiting RNR that is consistant with Spd1 associating with Cdc22. Since Spd1 alone has domain sequences conserved with Dif1, Sml1 and Hug1 it may be that Spd1 is the sole ortholog of ancestral yeast gene, with a multiplicity of functions adopted by the separate proteins in *S. cerevisiae*. In the *spd1* sequence, the HUG domain (aa 30-62) is represented by the mutants *spd1-m10* to *spd1-m19*. Mutations in this region largely affect nuclear localisation and restraint of RNR activity [62-63]. The R1 binding region of Spd1 (aa 83-97, by conservation with Sml1) is represented by *spd1-m28* to *spd1-m32* and mutations in this region have been found not to influence significantly restraint of RNR activity and or nuclear localisation [70].

4.2 Spd1 *S. pombe* mutants with double FP-tagged Suc22+Cdc22

CLSM imaging and FRET by acceptor photobleaching experiments were performed on Spd1 mutants and positive (Wt /FRET) and negative controls (single- tagged protein and untagged wild type strains). Out of the 41 mutants, only 12 showed FRET in S and G2 phases in both compartments. Generally, the FRET levels of the s*pd1* mutants: *spd1-m2, spd1-m3, spd1-m4, spd1-m8, spd1-m12, spd1-m23,spd1-m25, spd1-m33,spd1-m36* and *spd1-m41* were found to be comparable to that in wildtype (Wt in the presence of Spd1). The remaining Spd1 mutants were more closely aligned with deleted of Spd1 (*spd1::ura4+)* with loss of FRET and the concomitant bleaching of CFP fluorescence upon exposure of the acceptor YFP to the 514 nm photobleaching laser. Pre- and post bleach images and FRET maps for a sample of Spd1 *S. pombe* mutants are shown in Figures 4.1-.4.3 The specific mutants displayed in these images *spd1-m1*, *spd1-m2* and *spd1-m12*, represent examples that were characterised by Nesteros *et. al*. [63] as exhibiting a separation of the key Spd1 phenotypes, that is R1 (Suc22) nuclear localisation and restraint of RNR activity. Moreover these examples highlight a lack of correlation between these phenotypes and the ability of the mutants to undergo FRET.

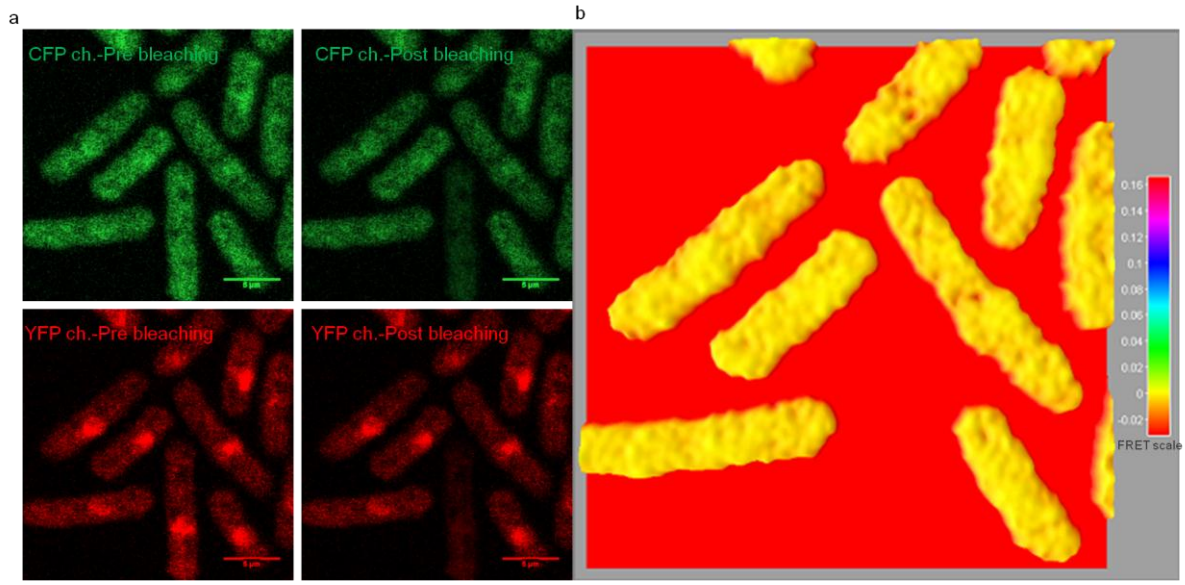

Figure 4.1: a) YFP– CFP *spd1-m1* 1images at 458 nm, prior to and following photobleaching of YFP at 514 nm. b) Surface plot display of the normalized covariance image between pre and post CFP

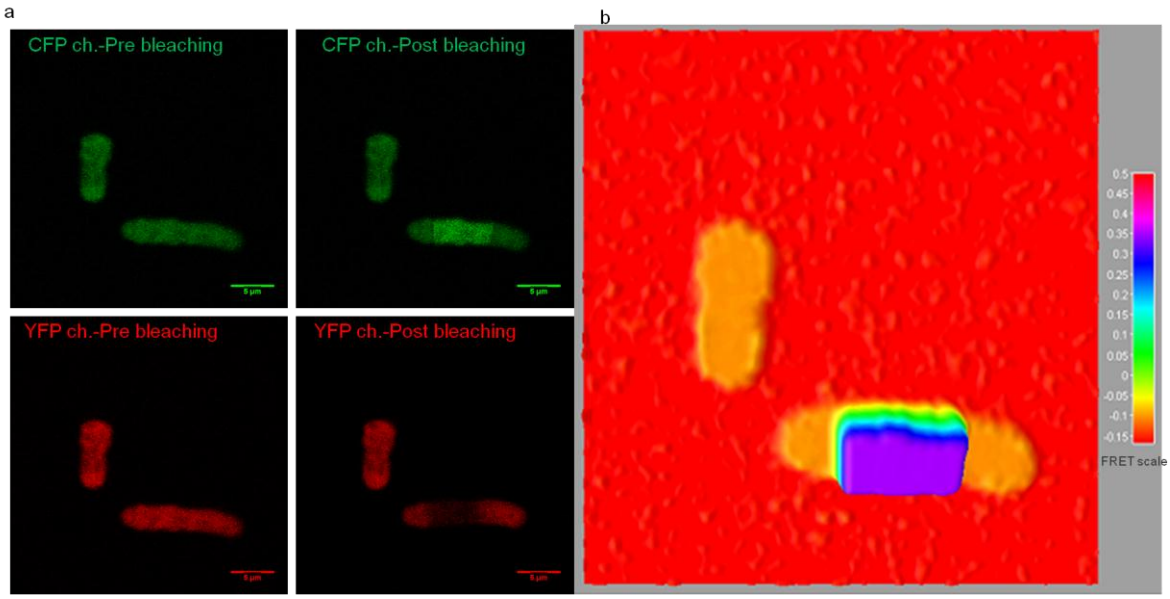

Figure 4.2: a) YFP– CFP *spd1-m2* images at 458 nm, prior to and following photobleaching of YFP at 514 nm. B) Surface plot display of the normalized covariance image between pre and post CFP.

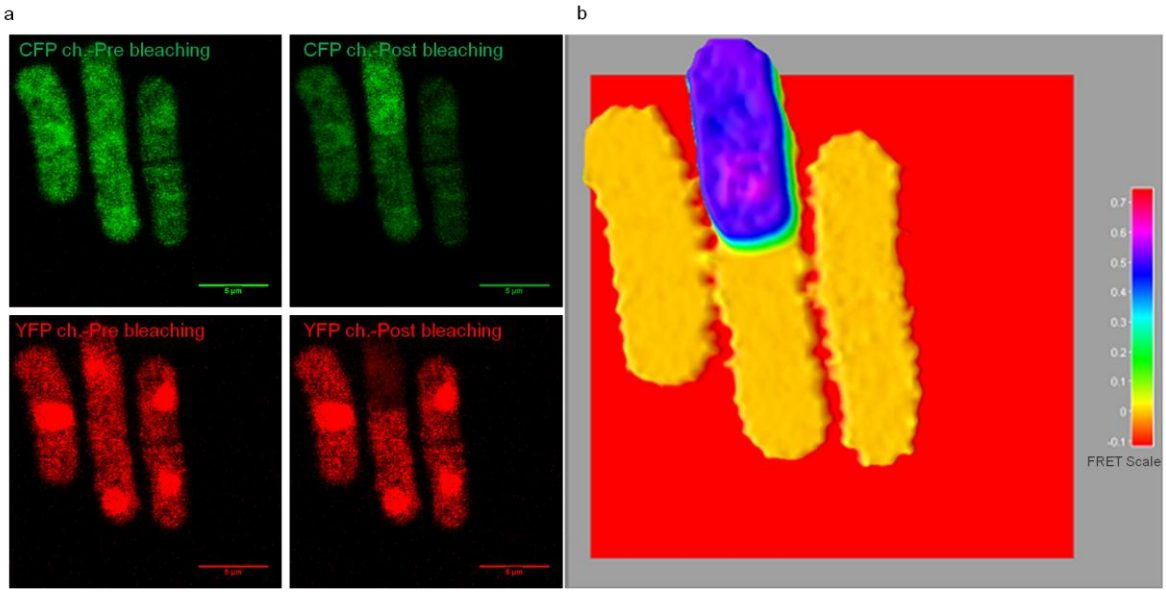

Figure 4.3: a) YFP– CFP *spd1*-m12 images at 458 nm, prior to and following photobleaching of YFP at 514 nm. B) Surface plot display of the normalized covariance image between pre and post CFP.

4.2.1 A test of system stability and reproducibility

Given the large array of mutants screened, the level comparison between cells will be largely dependent on the quality and reproducibility of the images. In order to eliminate as much variability the experimental conditions as possible, from cell culture growth and sample preparation to imaging and photobleaching laser intensities, FRET experiments were performed on a subset of mutant strains on the same day, under essentially the same conditions. *S. pombe* mutants exhibiting positive FRET efficienies were considered most important since the measured efficiency will be most sensitive to under- or over-bleaching YFP and the incidental photobleaching of CFP. By repeating the same experiment on a separate day, measure FRET efficiencies were found to be highly reproducible indicating the cell system and imaging platform are stable or at least the measurment of FRET in these cells is insensitive to any small changes in the experimental conditions that may have occurred between independent measurements. Histograms of FRET efficiencies were constructed from a population of over 18 number of cells for the wild type and *spd1* mutants in both nucleus and cytoplasm for S phase and G2 phase for two sparate days is presented in Figure 4.4.

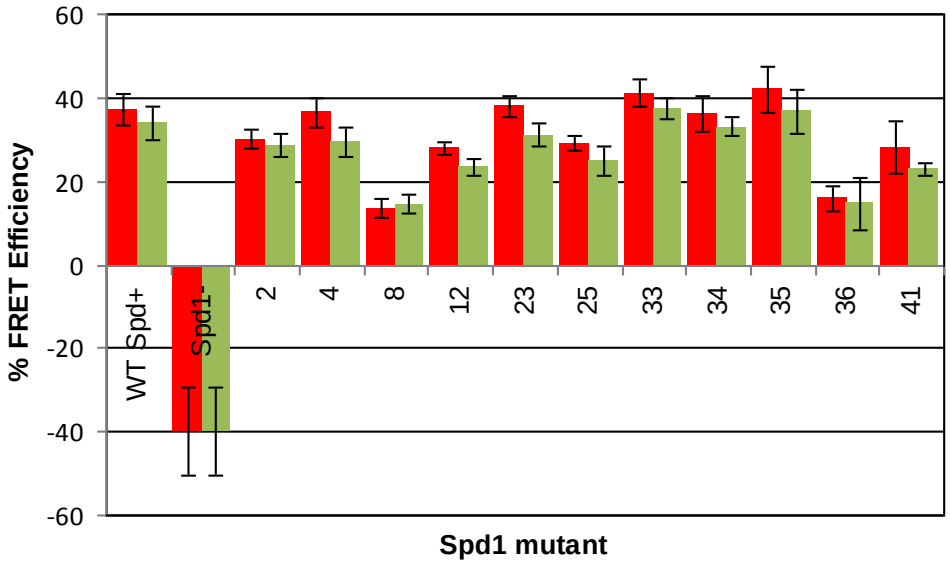

Figure 4.4: Histogram of %FRET Efficiencies in Wt, *spd1::ura4+* and FRET positive Spd1 mutants in the cytoplasm for S phase carried out on two separate days (red and green respectively) to test reliability of FRET measurments and reproducibility. All mutants were examined for FRET under the same conditions on each day (within the limits of control). FRET efficiencies represent averages over a sample population of each mutant.

4.2.2 Suc22-Cdc22 FRET vs RNR inhibition and Suc22 localisation

Additional experiments on the FRET postive Wt and *spd1* mutants strains were performed to examine the variability between FRET efficiencies in the nucleus and the cytoplasm for both S and G2 phase for which measured values and their standerd diviation errors are presented in Table 4.1. Cytoplasmic FRET does not vary significantly between phases or indeed mutants and Wt with the exception of *spd1-m8*, *spd1-m12* and *m36* that should reduced levels of enhanced donor CFP by up to 50%. These reduced levels of FRET do not appear to correlate an any way with either loss of nuclear localisation or RNR restraint. For example *spd1-m8* and *spd1-m36* display comparable levels of FRET yet have substantially different levels of RNR activity, *spd1-m36* showing no restraint, while *spd1-m8* has a more moderate effect on RNR restraint [63]. On the other hand *spd1-m12* and *spd1-m36*,

have been shown to exhibit no localisation defect and but comparable loss of RNR restaint, yet show different levels of FRET. This lack of correlation is more apparent when FRET positive mutants are compared to those lacking FRET but possessing similar RNR phenotypes in terms of R2 localisation and RNR restraint as highlighted below.

***S. pombe* strain**	**S phase Nucleus**	**S Phase Cytoplasm**	**G2 Phase Nucleus**	**G2 Phase Cytoplasm**
Wt	17.5 (3.6)	36 (4)	9 (1.7)	34.9 (3.5)
spd1-m2	14 (2.8)	33 (2.6)	7.1 (2.01)	30.7 (2.78)
spd1-m4	15 (2.1)	35 (3.4)	7.4 (2.6)	27.7 (3.98)
spd1-m8	10 (1.5)	16 (2.29)	6.32 (1.34)	16.6 (2.54)
spd1-m12	11 (1.67)	25.5 (1.96)	6.79 (1.29)	25.3 (1.770
spd1-m23	15.5 (2.1)	36.5 (2.68)	8.5 (1.88)	31 (2.3)
spd1-m25	13.5 (1.99)	30 (3.55)	7.8 (2.18)	28 (2.02)
spd1-m33	18.4 (2.76)	40 (2.35)	9.5 (2.11)	37.8 (3.5)
spd1-m34	17.9 (3.02)	39 (2.26)	9.2 (3.01)	32.6 (4.01)
spd1-m35	16.9 (2.45)	44.5 (5.15)	8.5 (2.76)	37.45 (4.12)
spd1-m36	11.6 (1.56)	14 (6.4)	7.3 (1.55)	16.5 (1.97)
spd1-m41	12.6 (3.6)	30 (1.57)	6.6 (1.67)	25.8 (2.76)

Table 4.1: The average percentage of FRET in S and G2 phase both the nucleus and cytoplasm over a small population of *S. pombe* cells. The standard deviation over the cell number is given in brackets.

For example, the *S. pombe* mutant strain *spd1-m2* undergoes FRET but lacks the Suc22 nuclear localization function. Mutant *spd1-m12* similarly shows R1–R2 FRET, however, it lacks the ability to restrain RNR activity according to the *rad3-ts csn1-d* double mutant and *dbb1-d* assays of Nesteros group [63] as described in Chapter 2. The results of these

experiments are summarised in Figure 4.5, which score the restraint of RNR activity in terms of moderated mutant culture growth in the former assay and lack of spore formation in the latter.

a

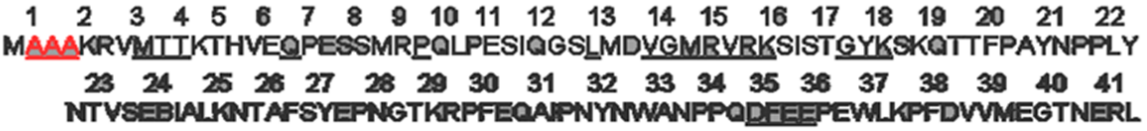

b

Residue No.	*spd1*-mutant No.	RNR	Residue No.	*spd1*-mutant No.	RNR
1-3	*spd1-m1*	Highly regulated	64-66	*spd1-m22*	Highly regulated
4-6	*spd1-m2*	Highly regulated	67-69	*spd1-m23*	Highly regulated
7-9	*spd1-m3*	Highly regulated	70-72	*spd1-m24*	Highly regulated
10-12	*spd1-m4*	Highly regulated	73-75	*spd1-m25*	Highly regulated
13-15	*spd1-m5*	Highly regulated	76-78	*spd1-m26*	Not regulated
16-18	*spd1-m6*	Highly regulated	79-81	*spd1-m27*	Highly regulated
19-21	*spd1-m7*	Highly regulated	82-84	*spd1-m28*	Highly regulated
22-24	*spd1-m8*	Highly regulated	85-87	*spd1-m29*	Highly regulated
25-27	*spd1-m9*	Highly regulated	88-90	*spd1-m30*	Highly regulated
28-30	*spd1-m10*	Low regulation	91-93	*spd1-m31*	Highly regulated
31-33	*spd1-m11*	Not regulated	94-96	*spd1-m32*	Highly regulated
34-36	*spd1-m12*	Low regulation	97-99	*spd1-m33*	Highly regulated
37-39	*spd1-m13*	Low regulation	100-102	*spd1-m34*	Low regulation
40-42	*spd1-m14*	Not regulated	103-105	*spd1-m35*	Low regulation
43-45	*spd1-m15*	Low regulation	106-108	*spd1-m36*	Highly regulated
46-48	*spd1-m16*	Low regulation	109-111	*spd1-m37*	Highly regulated
49-51	*spd1-m17*	Highly regulated	112-114	*spd1-m38*	Highly regulated
52-54	*spd1-m18*	Low regulation	115-117	*spd1-m39*	Highly regulated
55-57	*spd1-m19*	Low regulation	118-120	*spd1-m40*	Highly regulated
58-60	*spd1-m20*	Highly regulated	121-123	*spd1-m41*	Low regulation
61-63	*spd1-m21*	Highly regulated			

Figure 4.5: *spd1* sequences, every three amino acids were replaced by three alanines to produce one mutant. b) Mutant array (labelled *spd1-m1* to *spd1-m41*). Mutant with red colour shown no FRET while the green once show FRET, according to Nestoras data some mutants show high RNR restraint like Wt and some show low RNR restraint and some behave like *spd1*deleted [63].

Mutants like *spd1-m1* have both the Suc22 nuclear import function and the ability to restrain RNR activity in a similar mannner to Wt cells, but did not promote FRET [63] as seen in the histogram of FRET efficiencies across all mutants, presented in Figure 4.6. For each mutant the FRET efficiency corresponds to the average over a population of 60 cells, measured in the cytoplasm of cells in the S phase of the cell-cycle. Mutants, *spd1-m10* and *spd1-m11* have

little or no import defect, but are significantly unable to restrain RNR activity in the same way as *spd1-m12*, but in this case show no FRET. The mutations in the region of *spd1-m10* through to *spd1-m20* influence both import and restraint functions. In the extreme, *spd1-m14* exhibits, both loss of localisation and restraint of RNR activity and displays no FRET, phenocopying of *spd1* deleted. In this case the residues 30-62 span a R2 binding region by homology with Dif1, the R2 nuclear localisation protein of *S. cerevisiae*[62]. Mutations in the C-terminal region (*spd1-m34* through *spd1-m41*) also influence both import and restraint activity, and while this region is associated with R1 binding in Dif1, the effect of mutations in this region on nuclear import suggests there may be a role in binding R2 (Suc22) in the case of Spd1 in *S. pombe*. Finally, mutations within the R1-binding region (*spd1-m28* through to *spd1-m32*), upstream from the C-terminal region, were found not to strongly influence either import or restraint of RNR activity. These mutants, might therefore be expected to phenocopy FP-tagged Wt, however no FRET was observed. Overall it appears that the ability to promote FRET does not correlate with RNR inhibition or nuclear import. However, loss of both R2 localisation and RNR restraint does correlate with the loss of FRET as observed in the *Spd1::ura4*, *spd1-m14* and *spd1-m26* mutants. The results indicate that in the *S. pombe* system reported here FRET provides and indication of a Suc22-Cdc22 interaction, at least at the level of the Forster distance for CFP-YFP, but not at the level of an active RNR complex.

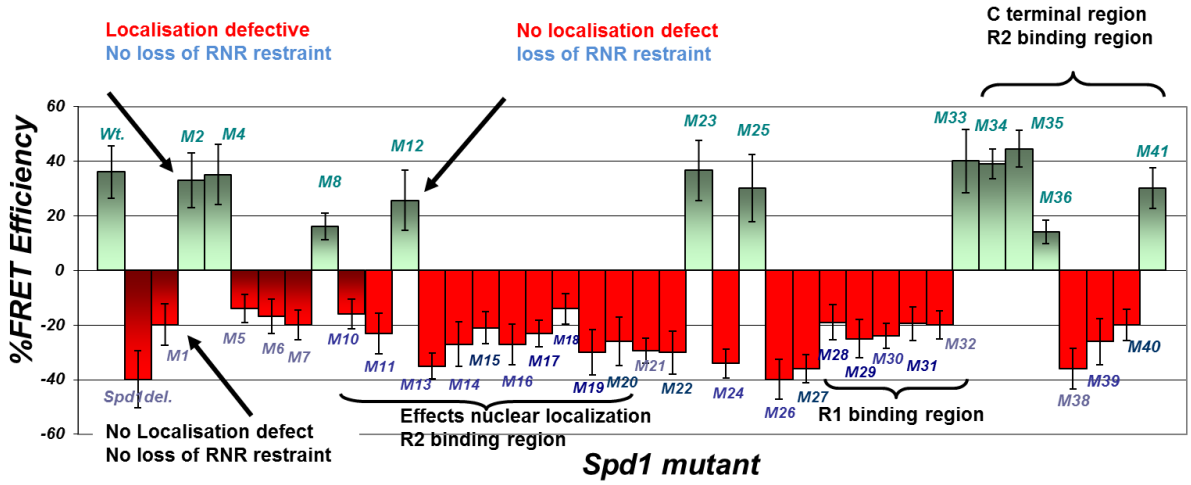

Figure 4.6: Histogram of %FRET Efficiencies in Wt, *spd1*deleted and *spd1* mutants in the cytoplasm for S.phase in different days with different cultures.

4.3 FRET analysis of Spd1 mutants after HU and 4NQO treatment

For completeness *S. pombe* with *spd1* mutants were treated with hydroxyurea and the DNA damage inducing drug 4NQO in the same way as the FP-tagged Wt and *spd1::ura4+* strains and examined for FRET. Results were consistent with previous Wt and *spd1::ura4+* data presented in Chapter 3, all mutants showed no FRET after HU treatment including those mutants, that left untreated, exhibit FRET (Figure 4.7).

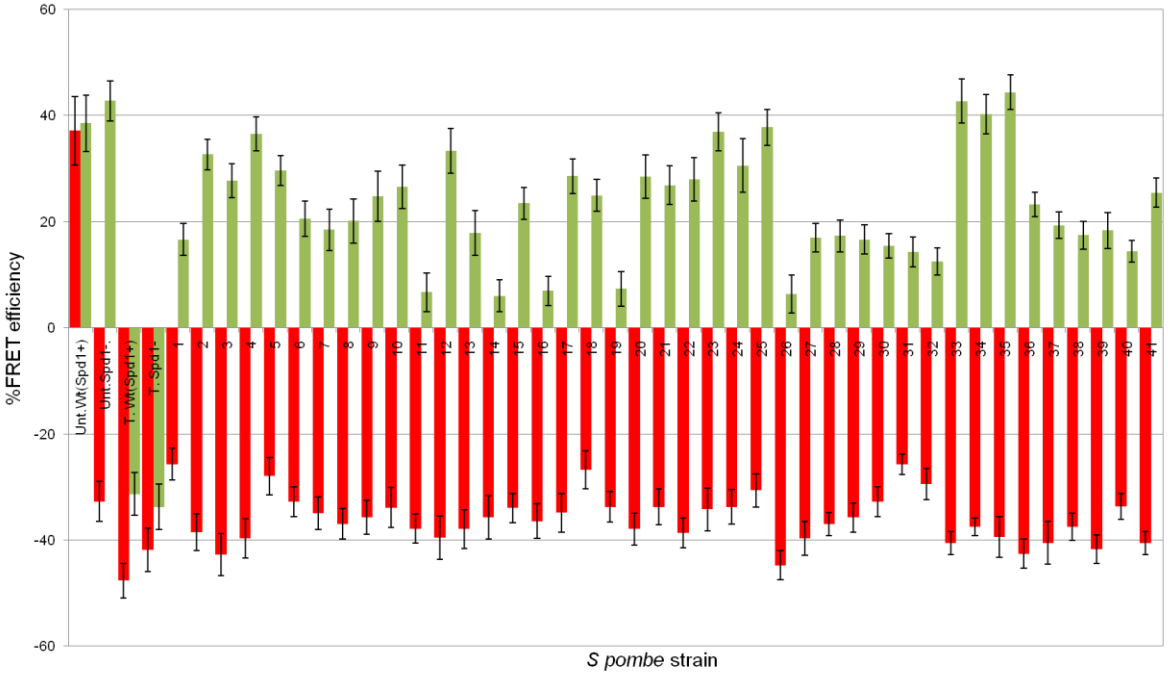

Figure 4.7: Percentage of FRET efficiency in the untreated Wt, untreated *spd1::ura+4*, treated with HU and 4NQO Wt, treated *spd1::ura4+* and *spd1* mutants after treating the cells with HU (red bars) and treated with 4NQO(green bars) with their error bars for apopulation of more than 60 cells.

It is apparent that the HU, while scavenging the free radical and inactivating the RNR catalytic activity, also appears to either disturb the architecture of FRET competent complexes or quenches the FP excited states with the subsequent loss of FRET [70,108,119-121].

The converse result was obtained after 4NQO treatment. All Spd1 mutants showed FRET including those mutants did not normally display FRET (Figure 4.7). This indicates that through some mechanism and after DNA damage, the RNR complex is more active as it increases its dNTPs levels [70]. Therefore the RNR complex is modified into a mature/active complex and allows FRET. As Spd1 is degraded after this treatment and therefore its degradation brings the RNR in the correct conformation or alignment to allow FRET [122].

Chapter 5

Development of near-TIRF microscopy for enhanced cellular imaging

5.1 Introduction

In the modern era of biological research, microscopy has been an invaluable tool for visualizing biological structures, from tissue cultures and the single cell, to individual organelles and bio-macromolecules. In fluorescence microscopy, various mechanisms are commonly used to enhance contrast, often by limiting the excitation and detection of fluorophores to a thin region of the specimen. Elimination of autofluorescence from outside the focal plane can considerably improve the signal-to-noise ratio, and hence the resolution of the object of interest. In confocal fluorescence microscopy, as has been described previously, this is achieved by exploiting the narrow depth-of-focus of a high numerical aperture objective lens and a pinhole to sample fluorescence only in the focal plane of the lens.

An alternative technique that has found an increasing number of applications in life sciences is total internal reflection fluorescence (TIRF) microscopy, which restricts the excitation of fluorescence to a plane at the interface between a high refractive index substrate and low refractive index medium. In this case, the optical phenomenon by which light, incident on the substrate at a supercritical angle, is completely reflected at the interface with a lower refractive index medium to produce a shallow evanescent field is exploited to restrict the excitation depth. Since the first reported application of TIR microscopy by Daniel Axelrod in the early 1980s, TIRF microscopy has been used in numerous applications in the field of cellular biophysics including the study of membrane structure and dynamics, cell

signalling and molecular motility assays [123-128]. The ability to restrict illumination and detection to a well defined plane, without the constraint of an interface, whilst maintaining the wide-field imaging advantages of TIRF, has lead to a the development of a number of novel techniques outlined below.

5.2 Optical near-TIRF enhancement

The interaction at the boundary of two media having different refractive indices, n1 and n2, is described in Figure 5.1.

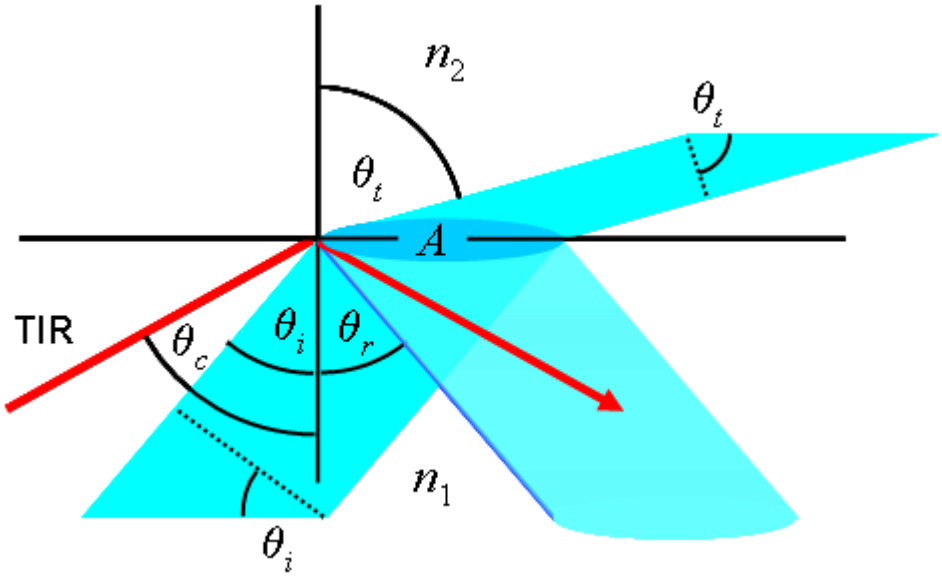

Figure 5.1: Schematic of incident, refracted, reflected rays of light at the interface between two media (having refractive indices n_1 and n_2). TIR (red line) is produced when the rays pass from a higher to a lower refractive index at an angle $\theta_i > \theta_c$ the critical angle. The illuminated area A is a projection of the incident beam cross-section and hence a function of the incident angle θ_i.

Total internal reflection occurs at a maximum angle of refraction $\theta_t = 90^o$, which then defines a critical angle θ_c at which the light must be incident for the beam to undergo TIR.

$$\theta_c = \sin^{-1}\left(\frac{n_2}{n_1}\right) \qquad 5.1$$

For an interface between glass (n_1 = 1.52) and water (n_2 = 1.33), the value of the critical angle θ_c is ~ 61^o which rises to ~65.2^o in the case where the low refractive medium is a cell, where the refractive index is typically that of the cytosol (n_2 = 1.38).

As explained in Chapter, for an incident angle $\theta_i > 0$ the electric field of the beam will have a component parallel and perpendicular to the interface the fraction of the incident field reflected into each component are given by the reflection coefficients and to obtain t^2 the fraction of the incident intensity in the transmitted beam at the interface as a function of the incident beam angle θ_i, which is given by

$$t^2 = \frac{\left(1-r^2\right)n_1 \cos\theta_i}{n_2\sqrt{1-\left(n_1/n_2\right)^2 \sin^2\theta_i}} \qquad 5.9$$

The function is plotted in Figure 5.2 (red), along with the ratio of incident beam to transmitted beam cross-section (blue) and the functions r^2 (yellow) and (1-r^2) (green). It is from the graph that an enhancement in the transmitted field intensity is observed at high angles of incidence, primarily due to the reduced transmitted beam cross-section increasing the photon flux per unit area, compared to that of the incident beam (blue).

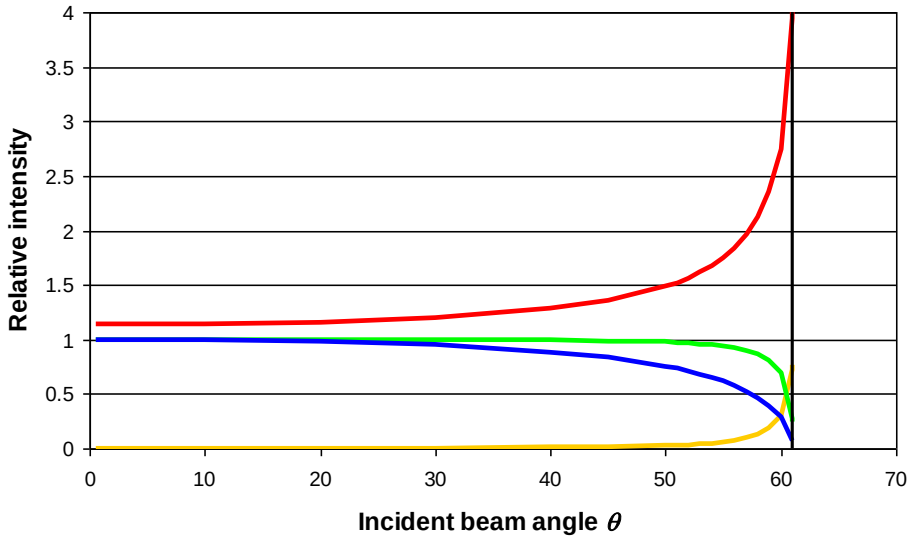

Figure 5.2: Plot of the fraction of incident beam intensity in the reflected beam, r^2 (yellow) and transmitted beam ($1-r^2$) (green) and the beam intensity at the interface (red), corrected for the reduction in beam size (blue) as a function of the incident beam angle. The high and low refractive index medium correspond to glass (n_1 = 1.52) and water (n_2 = 1.33).

The advantage of the nTIRF system developed here was the ability to switch simply from an epi-illumination configuration to total internal reflection by simply rotation of an input mirror. In the epi-illumination set-up the excitation beam lies along the optical axis throughout the optical excitation train from the external focusing lens through the objective, while in TIRF the excitation beam is rotated off the axis of the focusing lens by an amount that adjusts the angle of incidence on the sample coverslip to just above critical. By acquiring a stack of images (a movie) whilst rotating the input mirror images over the the entire range of incident angles from 0 to θ_c were recorded to observed the level of enhancement expected from the above solution to the Fresnel equations. Figure 5.3 shows four images from an image stack of 65 frames covering the entire range from epi-illumination to TIR.

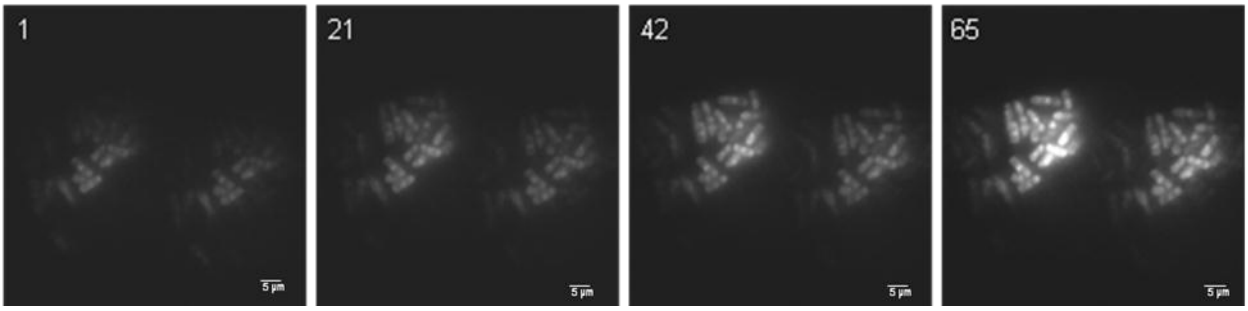

Figure 5.3: A series of images from a stack (movie) recorded during the translation of the excitation beam through angles of incidence that covered on-axis epi-illumination at $\theta_i = 0$ to TIR with $\theta_i > 61^o$. The angle is uncalibrated but an increasing brightness reflects the field enhancement due to changes in the Fresnel coefficients of reflection and transmission and the diameter of the incident and transmitted beams.

By analysing the entire image stack the effect of enhancement was made semi-quantitative using the Weber contrast ratio that considers the object intensity corrected for background against the background signal Image [139]. This measure of contrast is considered highly suited to images that a dominated by background as is clearly seen in the case of images in Figure 5.5. For simplicity we use the maximum intensity in each image and the mode that is the most frequent pixel intensity, to reflect the background. The contrast is then given by $(I_{max} - I_{mode}) / I_{mode.}$, the values of which are plotted in Figure 5.4 for a 65 frame stack progressing from epi-illumination in frame 1 to TIR by frame 59. The curve, although not calibrated in the angle of incidence of the excitation beam does show good qualitative agreement with the theoretical enhancement predicted above. Indeed, the four-fold enhancement predicted around the critical angle for TIR is reproduced well in frame 58 after which the contrast drops rapidly as the beam undergoes TIR and fluorescence in the nucleus and cytoplasm becomes inaccessible to excitation by the shallow evanescent field depth.

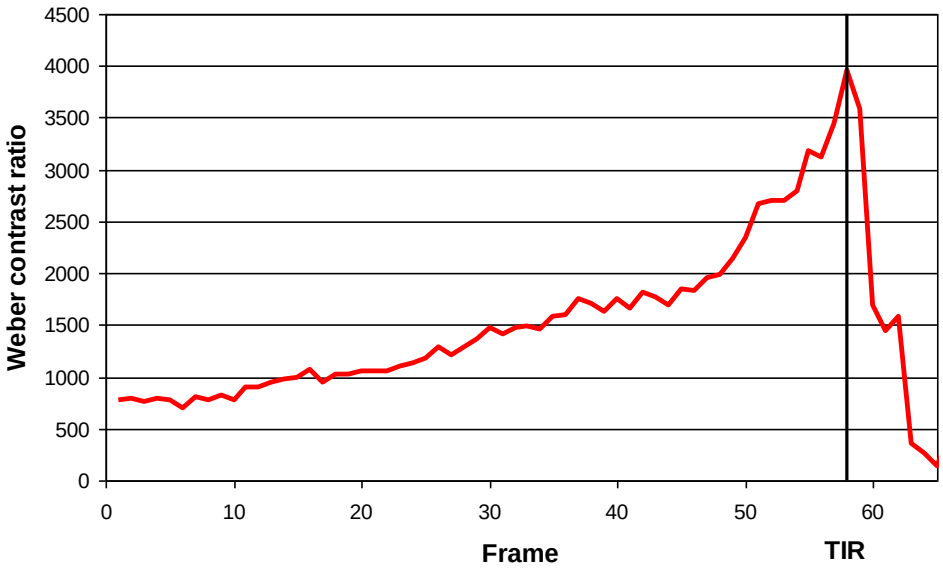

Figure 5.4: Graph showing the Weber contrast ratio as a function of the frame in an image stack corresponding to a changing incident beam angle. The per-frame angle is uncalibrated but a clear four-fold enhancement is observed as the angle approaches the critical angle for total internal reflection.

5.3 Constrained excitation by oblique angle illumination

The fluorescence enhancement observed in the nTIRF images and more specifically the contrast ratio derived is primarily due the nature of the excitation field under highly inclined illumination. However the accompanying restriction in the excitation depth will also contribute to an increase in contrast ratio, since fluorescence contributions from above the specimen plane will reduce as the transmitted excitation beam penetrates less of the bulk liquid at increasing angles of refraction. Given the relationship between the incident excitation beam cross-section and the illuminated area it is possible to estimate the effective depth of the "optical slice" from images at the extremes of epi-illumination ($\theta_i = 0$) and maximum enhancement just prior to TIR. Under epi-illumination the image footprint simply represents the circular cross-section of the 2D Gaussian beam intensity profile. At increasing angles of incidence the footprint becomes elliptical with a short axis of the same diameter as

the beam cross-section but with a long axis increasing as $D/\cos\theta_i$, where D is the diameter of the incident beam reported by the fluorescence footprint in epi-illumination mode. Thus, the angle of incidence of the excitation beam is readily determined from the ratio of the diameters of the fluorescence footprint in epi-illumination and oblique angle modes according to the relationship $\cos\theta_i = D_{\text{epi}} / D_{\text{nTIR}}$, where D_{epi} and D_{nTIR} are the diameters of the fluorescence footprint in epi-illumination and at highly inclined angles near-TIR. Snell's law can then be applied to determine the angle of refraction, θ_t, of the transmitted beam and the effective depth, *dz*, in the nTIRF image determined before. Presented in Figure 5.5a and 5.5b are fluorescence images of Suc22-CFP+Cdc22-YFP tagged *S. pombe* cells recorded in epi-fluorescence mode and in the oblique angle nTIRF configuration, respectively. Also shown are the corresponding intensity profiles through the marked lines (yellow). The circular profile of the excitation beam is clearly evident in epi-fluorescence, while in nTIRF the long axis of the elliptical footprint has approximately doubled. Indeed measuring across the line profiles at a common intensity (red lines) the epi-fluorescence cross-section measures 107 pixels, while in nTIF fluorescence is still detected at the same intensity at 219 pixels.

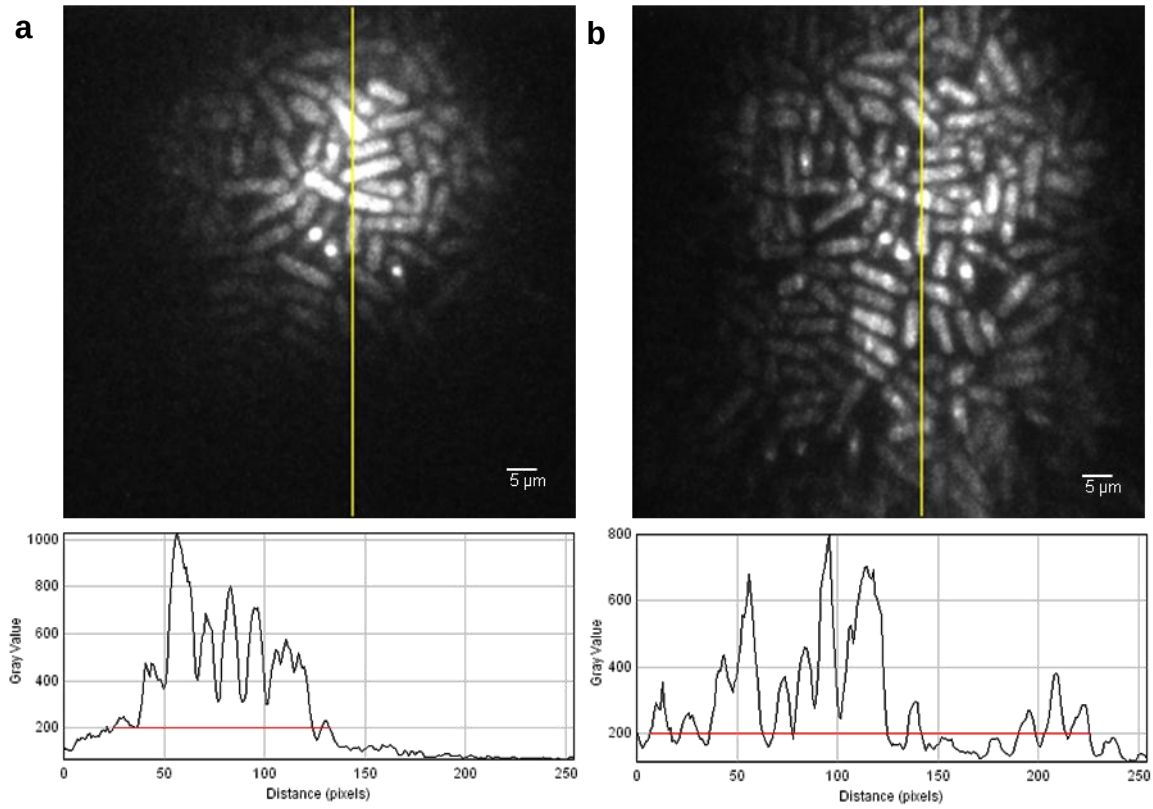

Figure 5.5: Images of double-tagged *S. pombe* (Suc22 CFP-Cdc22 YFP) cells with excitation laser line 458 nm under single channel detection in a) Epi-illumination mode ($\theta_i = 0$) and b) the nTIR configuration with $\theta_i \sim 60^o$. Present below each image is the intensity profile defined by the yellow line which has the same displacement and length in each image. The red line in these profiles highlight the increase in the fluorescence footprint diameter at a common fluorescence intensity. In the case of epi-illumination the profile covers approximately 107 pixels ~ 50 μm, while the nTIR footprint extends 219 pixels ~ 103 μm.

The ratio of these diameter gives an incident beam angle $\theta_i = \cos^{-1}(107/219) = 60.8^o$, close to the critical angle for TIR at the glass/water interface. The angle of refraction is then $\theta_t = (1.52/1.33)\sin^{-1}(60.8) = 86.0^o$. The pixel size in the images is measured to be ~ 0.47 μm, from the length of S phase ~ 14 μm that covers ~ 30 pixels, such that the fluorescence footprint in nTIRF has a long axis of 219 x 0.47 = 103 μm. Thus, the optical slab depth of dz = 103/tan(86.0) ~ 7 μm which is only about twice the width of the *S. pombe* cell (3-4 μm). By accurately controlling the incident beam angle close to the critical angle it may be possible to

reduce this depth further to highlight internal structures. For example, it is evident from 5.4b that in certain cells particularly in the lower half of the image, nuclei appear to be highlighted over and above cytoplasmic fluorescence. Non-uniformity in the excitation intensity profile and scatter from cells does lead to some variation and apparent striations in the image that may be eliminated to some degree by removing the coherency of the laser source, with for example a diffusive optical element.

5.4 FRET imaging of the RNR interaction in *S. pombe* by near-TIRF

As a final demonstration of the sensitivity of nTIRF the technique was applied to been the visualization of *S. pombe* cells and the interrogation of the RNR interaction by performing photobleaching FRET. Samples of *S pombe* cells (Wt/Suc22-YFP-Cdc22-CFP) were fixed with methanol and controls (Wt, single- tagged protein Suc22-YFP/CFP and Cdc22-CFP/YFP) were imaged. Preliminary results were encouraging and showed FRET was maintained for Wt (Spd1+) in the nucleus and cytoplasm for both S and G2 phase as shown in Figures 5.6- 5.9.

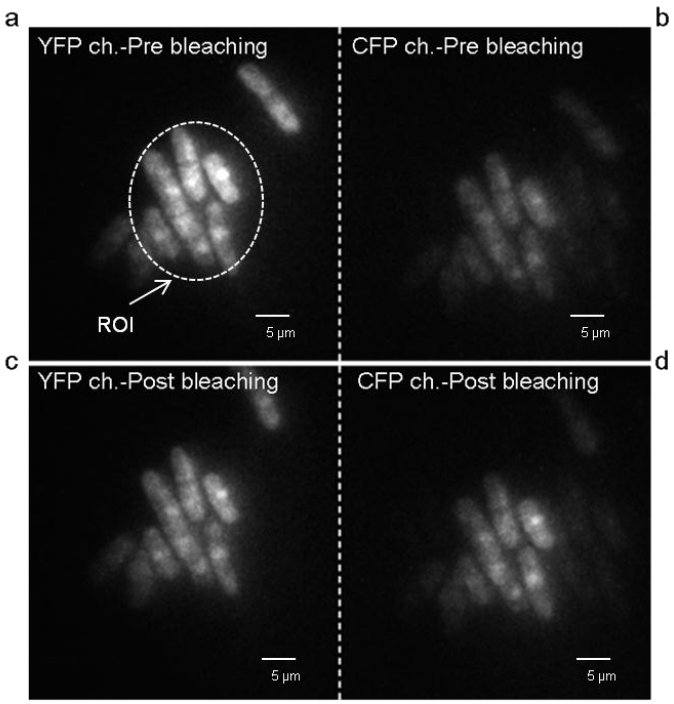

Figure 5.6: A typical image set of the *S. pombe* (Wt/Suc22-CFP- Cdc22-YFP) at 458 nm prior to and following photobleaching of YFP at 514 nm. a) Pre-bleached on YFP ch, b) Pre-bleached on CFP ch., c) Post-bleaching of YFP on the YFP ch. and d) Post-bleach of CFP on the CFP ch.

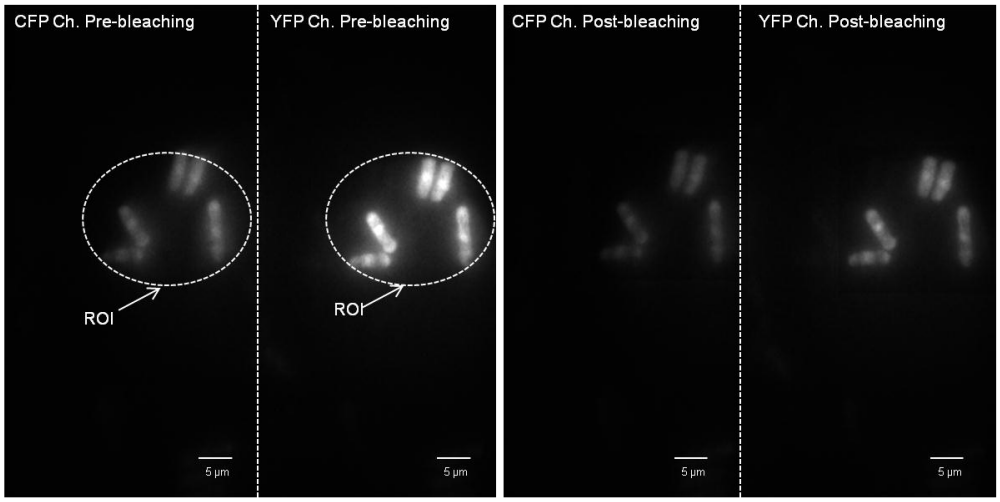

Figure 5.7: A typical image set of single tag *S. pombe* (Suc22-CFP-) cells at 458 nm prior to and following photobleaching of YFP at 514 nm and the corresponding images of the cells at the CFP channel pre and post bleaching.

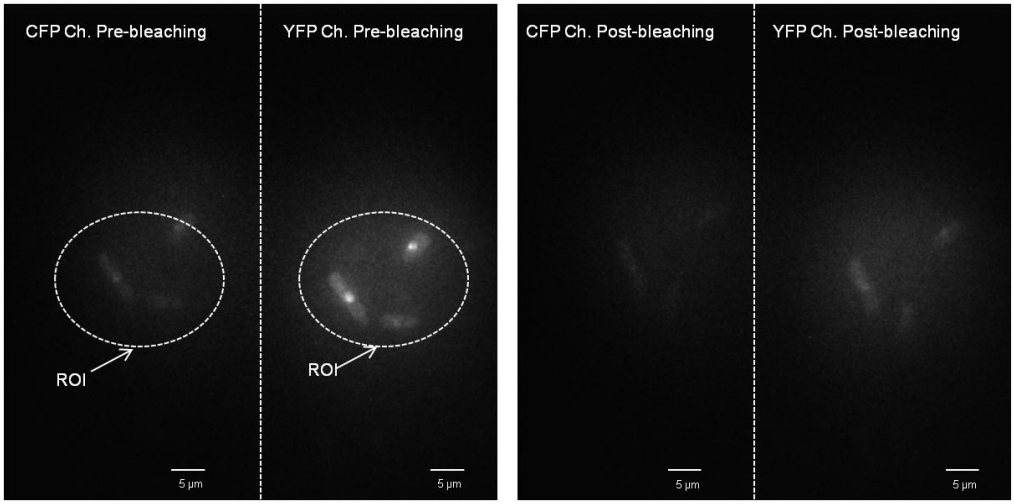

Figure 5.8: A typical image set of single tag *S. pombe* (Suc22-YFP-) cells at 458 nm prior to and following photobleaching of YFP at 514 nm and the corresponding images of the cells at the CFP channel pre and post bleaching.

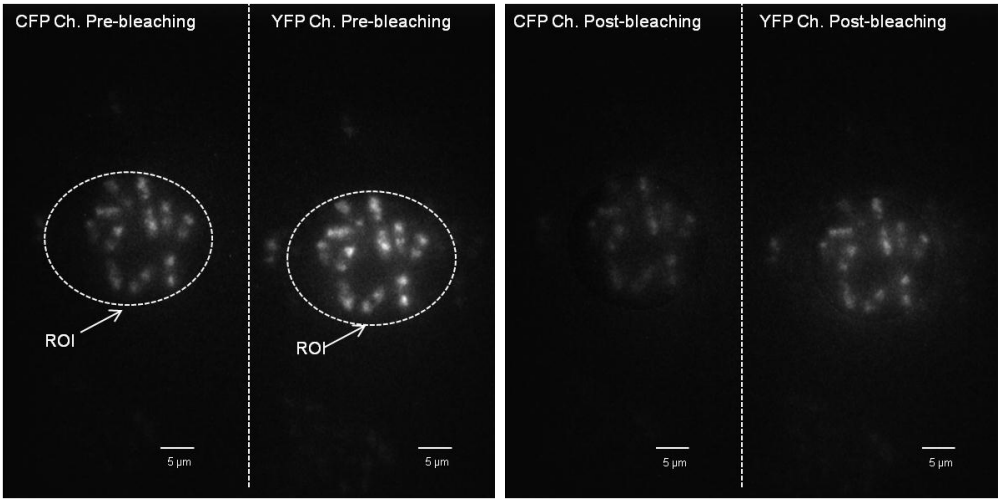

Figure 5.9: A typical image set of untagged wilde type *S. pombe* (Wt) cells at 458 nm prior to and following photobleaching of YFP at 514 nm and the corresponding images of the cells at the CFP channel pre and post bleaching.

FRET calculations were performed on ROIs in a similar way as that described in Chapter 3. Prior to measuring the intensities I_{DA} and I_D from the pre- and post-bleached CFP images, the individual frames are background subtracted, I_D is then calculated as an average

over each bleached ROI and the same ROI is used in the pre-bleached image for measurement of I_{DA}.

By accumulating a small number of FRET images spanning more than 20 cells, representative of the S phase of the cell-cycle and 20 cells in the G2 phase and interrogating both the cytoplasm and nucleus for FRET in each case, averages and standard deviations over the population were determined as presented in Figure 5.9. Cells in the G2 phase reported a percentage of FRET efficiency of 43 ± 7 % in the cytoplasm and 23 ± 11 % in the nucleus whereas for S phase; 40 ± 2% and 20 ± 4 % for both cytoplasm and nucleus respectively FRET values are close to those of the CLSM and provide confirmation that the system performs as expected (Figure 5.10).

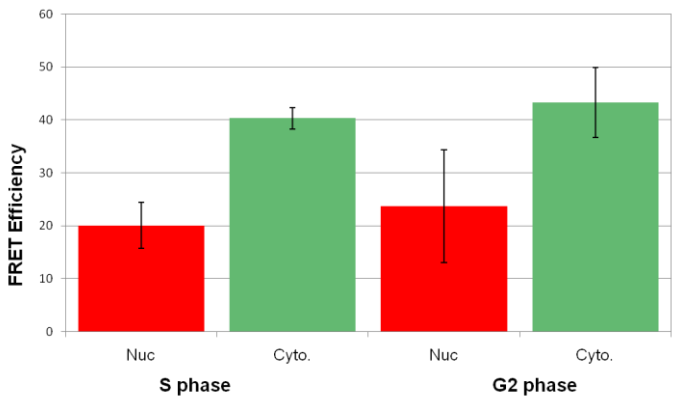

Figure 5.11: Histograms of %FRET efficiencies of the RNR in different phases and compartments for small number of cells (20 cells). Where the red bars represent the %FRET efficiency in the Nuc. whilest the green bars represent the FRET level in the cytoplasm.

Chapter 6

Conclusions and future work.

6.1 Conclusions

The faithful replication of DNA is prerequisite for maintaining the integrity of the genome. One important aspect of faithful DNA replication is the maintaining the correct concentration and relative ratio of dNTP precursors. dNTPs are formed by ribonuleotide reductase (RNR), which converts ribonucleotide diphosphates into their deoxy forms. If the levels of dNTPs or the relative ratios between the four bases are not carefully controlled, then DNA replication errors and thus mutation frequencies increase [21, 58]. In eukaryotes ribonucleotide reductase activity is dependent on type I RNR complexes, which consist of two large (R1) and two small (R2) subunits forming a tetramer [22]. The catalytic activity of the complex is associated with the R1 subunit, while the R2 subunit provides the diferic-tyrosyl radial [37]. Allosteric control of RNR regulates both the overall levels of dNTP synthesis and the precise ratio between the four different bases. The associated nucleotide binding sites are found on the R1 subunit [35, 58]. In addition to allosteric control, RNR is regulated by a number of further mechanisms: in all organisms studied RNR protein levels are regulated *via* transcription. This is particularly obvious in response to genotoxic stress, when DNA repair synthesis requires dNTP precursors to be present outside of S phase. In both the fission and budding yeasts, the R2 subunit of RNR has recently been shown to be re-localised from the nucleus to the cytoplasm in response to either S phase entry or genotoxic stress. Because the majority of the R1 subunit is constitutively cytoplasmic in both organisms, this relocalisation

has been proposed to promote the formation of active RNR complexes and thus contribute to regulation [47,116].

In fission yeast, R1 and R2 are represented by Cdc22 and Suc22 respectively. In another word, Regulation deoxyribonucleoside triphosphates (dNTPs) pools for faithful DNA replication ultimately requires the formation of the ribonucleotide reductase (RNR) complex *via* the interaction of the Suc22 and Cdc22 subunits. The ability to tag these subunits with fluorescent proteins now allows the application of FRET spectroscopy to interrogate the Suc22-Cdc22 interaction directly, in vivo.

Significant FRET levels (+ve FRET) were detected for RNR-tagged strains (both; Wt/Suc22-CFP-Cdc22-YFP and Wt/Suc-YFP-Cdc22-CFP) in both compartments (nucleus and cytoplasm) and in different cell-cycle phases (G2 and S phase) during which RNR is tightly regulated. Various single-tagged strains, Suc22-CFP/YFP and separately Cdc22-CFP/YFP, and wild type untagged-cells were examined to ensure there was no donor enhancement from photoinduced by products or autofluorescence.

Surprisingly, in S phase, the FRET level reported in the cytoplasm was found to be comparable to that in the G2 phase. The former phase (DNA replication) was predicted to have higher FRET signals due to delocalisation of Suc22 from the nucleus to the cytoplasm, as a result of Spd1 degradation, and hence an expected increased level of interaction with Cdc22 (formation of active complex due to the requirement of dNTPs) [47, 57,87,105,112]. Detected FRET levels in the nucleus in the S phase was found to be approximately double that in the G2 phase. Indeed the strongest changes in FRET were observed in the nucleus suggesting the component of the RNR regulatory pathway that induces, Cdc22 and Suc22 subunit interaction may be proliferate in the nuclei as well as the cytoplasm.

Spd1 is reported to be intrinsically disorderd protein (IDP) and NMR studies reported that IDP tends to adopt folding onto its interaction partner during their association [117]. This process can take place in protein-protein interactions with low affinity but high specificity [118]. When Spd1 deletion, the nuclear localisations of Suc22 were undetected in the samples under fluorescence microscopy. Furthermore, both double-tagged RNR strains showed no FRET (-ve FRET) in both S and G2 phase and since FRET is an indicator of RNR interaction. Thus, Spd1 is also important in mediating the Suc22-Cdc22 interaction in the formation of a FRET competent, but not necessarily active RNR complex.

When Spd1 present and *spd1::ura4+*cells were treated with HU, Cdc22-Suc22 FRET was also lost. When Wt (Spd1+) cells blocked in G2 and then treated with HU showed no FRET despite not progressing into S phase, indicating that HU may independently quench the FRET signal. Treating *S. pombe* cells with 4NQO, an inducer of DNA damage, nuclear localisation was largely detected and also FRET maintained in both nucleus and cytoplasmic compartments in both S and G2 phase as for the wild type double-taggged strain but only in the presence of Spd1.

The library of double FP-tagged *spd1* mutant *S. pombe* strains have been successfully screened for FRET using CLSM and have provided the means of separating the primary functions of Spd1, that of nuclear import of the RNR subunit R2 (Succ22) and inhibition or restraint of RNR activity. Analysis of Wt (Suc22-CFP + Cdc22-YFP) or swapped tagged strains and the equivalent Spd1 deleted strains provide examples in which, in the former case RNR actvity is “naturally” restrained and Suc22 localised in the nucleus by Spd1, while in the latter loss of Spd1 results in unrestrained RNR activity and complete delocalisation of the R2 subunit. The assays of Nesteros group [63] have established the effects of the systematic mutation of Spd1 by alanine scanning on Suc22 localisation and more importantly here the

restraint of RNR activity. Data showed that restraint of RNR activity did not correlate with Suc22 nuclear localization function. Imaging experiments reported here, provided confirmation of those mutants that displayed Suc22 localisation deficiencies (by lack or low intensity nuclei), no information on RNR activity is retreivable. Of the 41 mutants examined for FRET between FP-tagged Suc22 and Cdc22, only 12 exhibited FRET at levels that appeared not to vary significantly from Wt in either S phase or G2 phase, cytoplasm or nucleus. Of greater interest was the observation that the ability of Spd1 mutants to undergo FRET was not correlated with the nuclear import function of Spd1 or restraint of RNR activity, except in mutants that exhibited loss of both nuclear localisation and restraint, no example of positive FRET was found.

The lack of correlation between FRET efficient mutants and their ability to restrain RNR raises the question of what the FRET signal represents in terms the RNR architecture and changes thereof in response to Spd1 degradation, deletion or mutation. The RNR complex is composed of a tetramer of subunits, 2 x R1 (Cdc22) and 2 x R2 (Suc22) in the form of an $\alpha_2\beta_2$ complex [27]. In case of *Spd1::ura4*, FRET is undetectable and is therefore unable to report active tetramers since RNR in the *Spd1::ura4* background remains in an active form. Evidently, Spd1 has a significant role in promoting FRET between RNR subunits, while inhibiting activity in its native form. Studies on RNR in E. coli [113] and mouse [114] have indicated the possible formation of an octameric complex $\alpha_6\beta_2$ consisting of R1 hexamers (α_6) that can associate with the R2 dimer (β_2) subunit. Although, no clear evidence of such high order complexes were reported for RNR in *S. pombe* [63] the possibility that FRET derives from the oligomerisation of the RNR is cannot discounted without further structural studies.

A more attractive hypothesis, consistent with active RNR as an $\alpha_2\beta_2$ tetramer, is one in which Spd1 mediates the formation of immature, inactive RNR but FRET efficient complexes. In this case the fluorescent proteins are proximal and in an alignment that promotes FRET between the FP-tagged Suc22 and Cdc22 subunits. The model, along with the possibility of oligomerisation and their outcomes are schematised in Figure 6.1

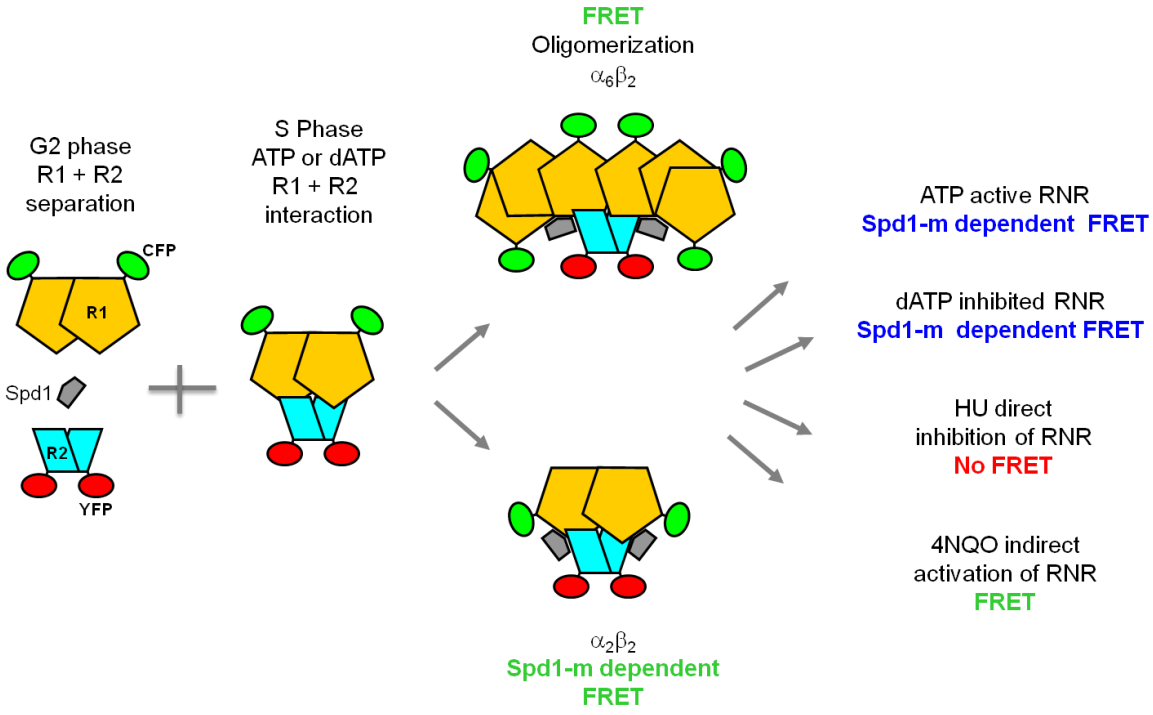

Figure 6.1: Schematic hypothesis of Spd1 in the regulation of RNR. In the presence of Spd1, FRET map reflects the immature inactive RNR (when bind to dATP substrate) complexes (in both cases: $\alpha_2\beta_2$ tetramer or octameric complex $\alpha_6\beta_2$) in appropriate aligned fluorophors. In case of *Spd1::ura4*, the complex is active (binds to ATP) in the favourable architecture and hence the fluorophors are far enough to show no FRET.

Two scenarios can then be postulated for the conversion of the $\alpha_2\beta_2$ tetramer to active RNR. Firstly it is possible that the Spd1 primes the RNR in an optimal architecture for activity upon Spd1 degradation and that no loss of FRET is observed during progression through S phase. In this case it is postulated that the lack of FRET observed in *spd1* deleted strains is attributed to RNR complexes in an active, but sub-optimal form for FRET with FP-

tags proximally or oriented in an unfavourable manner. Unrestrained RNR activity must then be associated with the lack of inhibition due to Spd1 deletion and an abundance of sub-optimal complexes that compensates for Spd1-dependent forms.

Alternatively Spd1 renders the RNR inactive in a sub-optimal configuration for NDP reduction but primed for FRET. Upon Spd1 degradation, the complex changes conformation to an active, but FRET deficient form due to a concomitant change in the position or orientation of the FP-tags. The fact that no significant variation in FRET efficiencies are observed across the S-phase population, which presumably samples different points throughout segregation, requires that the FRET signal is dominated by immature complexes in which Spd1 has not been degraded. This is consistent with a lack of complete delocalisation of Suc22 observed in the Wt, S phase cells, which implies the incomplete degradation of Spd1 in this case. In this instance, lack of FRET from FP-tagged RNR in the *Spd1::ura4* background is attributed to the formation of the active RNR complex directly without inhibition but with sub-optimal FP-tag distances or orientations for FRET.

In the context of the cell cycle, a scenario in which FRET is sensitive to Spd1 degradation can be envisaged. In the G2 phase Spd1 acts to import R2 (Suc22) but also binds to R1 (Cdc22). Upon entering the S-phase initial Spd1 degradation leads R2 relocation from the nucleus to the cytoplasm where levels of Spd1 are still sufficient to mediate a FRET efficient but inactive RNR complex. Continued Spd1 degradation leads to a population of FRET deficient but active RNR complexes. If this population remains small compared to those of the immature complexes the level of FRET will not change significantly from the start to completion of the S phase. With a typical uncertainty of ±10% in the FRET measurements reported here the experiment may not be sensitive to small changes in FRET associated with incomplete Spd1 degradation. This model, as schematised in Figure 6.2

would predict that further Spd1 degradation will lead to a larger population of active RNR with loss of FRET, which in the extreme case of the Spd1 deleted strain is complete.

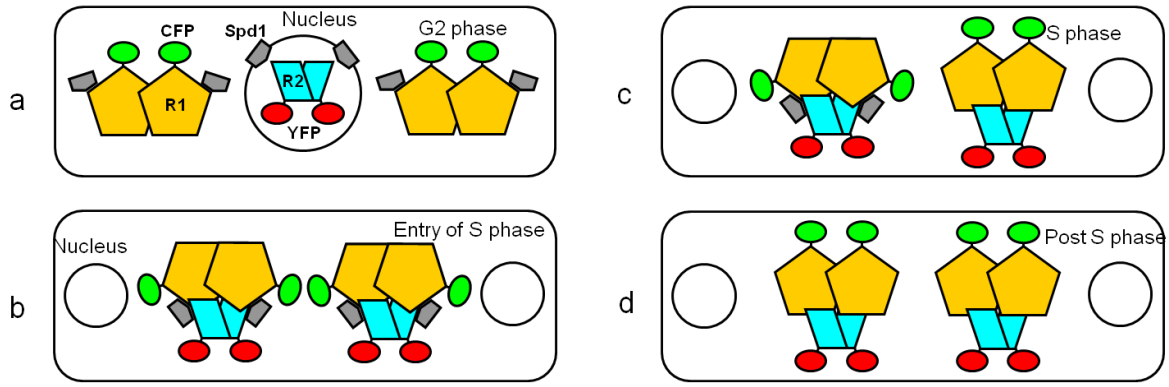

Figure 6.2: a) Localisation of R2 by Spd1 nuclear import and pan-cellular Cdc22 in the G2 phase. b) Start of S phase where, initially, low levels of Spd1 degradation leads to delocalisation of Suc22 to the cytoplasm and formation of FRET efficient R1-R2 complex. c) Continued, but incomplete, degradation leads to a sub-population of active but FRET deficient RNR complexes. d) *spd1* deleted results in FRET deficient but unrestrained RNR in the S-phase.

A semi-quantitative in vivo assay for the *spd1* mutant *S. pombe* strains identified near complete degradation of Spd1 which also correlated with complete loss of Suc22 localisation and FRET, an apparent phenocopy of *spd1::ura4+* [63]. On-the-hand, *spd1-m2* displayed lower levels of Spd1 degradation than Wt cells but with comparable FRET, despite the apparent loss of the Spd1 nuclear import function. In a final analysis there is the possibility that a more subtle correlation exists between the FRET observed in the RNR *S. pombe* system reported here and the role of Spd1 as an R2 nuclear import protein, its effect on restraining RNR activity but also its level of degradation. Correlations across the *spd1* mutant library may then provide greater insight in Spd1 domain specific roles. Such an analysis would require a more quantitative and accurate approach to measuring FRET, R1 localisation, RNR activity and Spd1 degradation and is beyond the scope of this thesis

nTIR microscopy is performed on a modified TIRF microscopy which has a number of advantages over established microscopy techniques such as epi-fluorescence microscopy and CLSM. The most important benefits are: a relatively high time resolution using a low laser power, with a reduction of photo-toxicity and improved signal to noise ratio. Moreover, TIRFM provides the potential for wide-field optical-sectioning with a narrow depth-of-field (illumination) and fast image acquisition with high contrast. Near-TIR is a highly inclined thin beam technique which was employed to image *S pombe* cells. The sample was illuminated at a high angle just below the critical angle for total internal reflection. As predicted from theoretical field enhancement, the nTIR field contrast closely reflects this enhancement with a demonstrated four-fold increase in the Weber contrast ratio. More specifically, the contrast ratio of the images has been improved as the excitation field is enhanced by a reduction in the transmitted beam diameter in addition to the reduced background due to the restriction in the excitation depth. Moreover, excitation depth was determined close that of the cell diameter ~7μm. Finally, the dual-view nTIRF has been successfully applied to FRET imaging of the FP-tagged RNR in *S. pombe*. The percentage of FRET efficiencies were maintained in RNR compartments (nucleus and cytoplasm) in both S and G2 phase at levels comparable to those of the CLSM experiments reported in this thesis.

6.2 Future work

For future wok, the motivation of this study was to use other technique like FCS to determine average mean diffusion times of species through detection volume in order to study the different conformations of RNR (dimers α_2 and ß$_2$ or tetramer α_2ß$_2$) and investigate these

results in presence or absence of Spd1. Given the differences of molecular weight between each subunit, one can expect to see a drastic change in the diffusion time between bound and unbound species. This may help to understand better the behaviour of both subunit and cast a light on the exact role of the Spd1.

The aim also is the investigation of *in vitro* interactions between purified proteins Suc22 and Cdc22. Hopes to observe the RNR complex formation and depending on the result, it would be then possible to add Spd1 and correlate results with previous in vivo work.

PhotoActivable Laser Microscopy (PALM), in association with TIRF, will be used for *in vivo* single molecules experiments. Indeed, this super-resolution tool has the ability to give nanometer resolution, photoactivation, localization, bleaching and fitting process. This may be useful to acquire more information on the proteins behavior in the cell.

Moreover, microfluidic chambers will be used to keep the cells in optimal conditions during TIRF experiment. This may allow us to measure different proteins levels during the cell cycle and have an idea of the influence of Spd1 on the RNR activity.

Bibliography

1. Forsburg, S. *et al. Regulation of the cell cycle in the yeasts Saccharomyces cerevisiae and Schizosaccharomyces pombe*, Annu. Rev. Cell Biol., 1991, **7**, 227-256.

2. Forsburg, S.L., *The yeasts Saccharomyces and Schizosaccharomyces pombe :Models for cell biology research*, Gravitational and Space Biology, 2005, **18**(2), 3-10

3. Augusto Cogoli et al.,Gravitational and Space Biology, Publication of the American Society for Gravitational and Space Biology, 2005, **18** (2), 162.

4. Leupold U., *Die Vererbung von Homothallie und Heterothallie bei Schizosaccharomyces pombe*. CR Trav Lab Carlsberg Ser Physiol, 1950, **24**, 381-480.

5. Leupold U, *The origins of Schizosaccharomyces pombe genetics in: Hall MN, Linder P. eds. The Early Days of Yeast Genetics*. New York. Cold Spring Harbor Laboratory Press, 1993, 125-128.

6. Sergio Morerno, A.K., Paul Nurse, *Method in Enzymology*, Academic Press, 1991, **194**, 793-823.

7. James B. Moseley, A.M., Anne Paoletti & Paul Nurse, *A spatial gradient coordinates cell size and mitotic entry in fission yeast*. Nature, 2009, **459**, 857-860.

8. Sawin, K.E., *Cell cycle: Cell division brought down to size*. Nature, 2009, **459**, 782-783.

9. Ding, D.Q., Tomita, Y., Yamamoto, A., Chikashige, Y., Haraguchi, T. & Hiraoka, Y., *Large-scale screening of intracellular protein localization in living fission yeast cells bythe use of a GFP-fusion genomic DNA library*, Genes Cells, 2000, **5**, 169–190.

10. Sawin, K.E., and Nurse, P., *Identification of fission yeast nuclear markers using random polypeptide fusions with green fluorescent protein*. Proc Natl Acad Sci U S A 1996, **93**, 15146-15151.

11. Simpson AJ, R.F., Arruda P, Abreu FA, Acencio M, Alvarenga R, Alves LM, Araya JE, Baia GS, Baptista CS, Barros MH, Bonaccorsi ED, Bordin S, Bové JM, Briones MR, Bueno MR, Camargo AA, Camargo LE, Carraro DM, Carrer H, Colauto NB, Colombo C, Costa FF, Costa MC, Costa-Neto CM, Coutinho LL, Cristofani M, Dias-

Neto E, Docena C, El-Dorry H, Facincani AP, Ferreira AJ, Ferreira VC, Ferro JA, Fraga JS, França SC, Franco MC, Frohme M, Furlan LR, Garnier M, Goldman GH, Goldman MH, Gomes SL, Gruber A, Ho PL, Hoheisel JD, Junqueira ML, Kemper EL, Kitajima JP, Krieger JE, Kuramae EE, Laigret F, Lambais MR, Leite LC, Lemos EG, Lemos MV, Lopes SA, Lopes CR, Machado JA, Machado MA, Madeira AM, Madeira HM, Marino CL, Marques MV, Martins EA, Martins EM, Matsukuma AY, Menck CF, Miracca EC, Miyaki CY, Monteriro-Vitorello CB, Moon DH, Nagai MA, Nascimento AL, Netto LE, Nhani A Jr, Nobrega FG, Nunes LR, Oliveira MA, de Oliveira MC, de Oliveira RC, Palmieri DA, Paris A, Peixoto BR, Pereira GA, Pereira HA Jr, Pesquero JB, Quaggio RB, Roberto PG, Rodrigues V, de M Rosa AJ, de Rosa VE Jr, de Sá RG, Santelli RV, Sawasaki HE, da Silva AC, da Silva AM, da Silva FR, da Silva WA Jr, da Silveira JF, Silvestri ML, Siqueira WJ, de Souza AA, de Souza AP, Terenzi MF, Truffi D, Tsai SM, Tsuhako MH, Vallada H, Van Sluys MA, Verjovski-Almeida S, Vettore AL, Zago MA, Zatz M, Meidanis J, Setubal JC., *The genome sequence of the plant pathogen Xylella fastidiosa. The Xylella fastidiosa Consortium of the Organization for Nucleotide Sequencing and Analysis*. Nature 2000, **406**, 6798-6826.

12. Forsburg, S.L., *The Best Yeast?* Trends Genet, 1999, **15**, 340-344

13. Aki Hayashi, D., Chihiro Tsutsumi, Yuji Chikashige, Hirohisa Masuda, Tokuko Haraguchi and Yasushi Hiraoka., *Localization of gene products using a chromosomally tagged GFP-fusion library in the fission yeast Schizosaccharomyces pombe*. Genes to Cells 2009, **14**, 217-225.

14. Niedenthal RK, R.L., Johnston M, Hegemann JH., *Green fluorescent protein as a marker for gene expression and subcellular localization in budding yeast*. Yeast, 1996, **12**(8), 773-86.

15. Nestoras., K., *A study of sumoylation and ubiquitination of the DNA damage and replication checkpoint proteins in the fission yeast, in school of life science*. 2006, University of Sussex: Sussex. p. 170.

16. Willson, J.C., *Investigation of the fission yeast response to DNA damage*, in school of life science. 1997, University of Sussex: Sussex. p. 150.

17. Mitchison, J.M.N., P., *Growth in cell length in the fission yeast Schizosaccharomyces pombe*. J. Cell Sci., 1985, **75**, 357-376.

18. Guertin, D.A., Trautmann, S. and McCollum D., *Cytokinesis in eukaryotes. Microbiol.* Mol. Biol. Rev., 2002, **66**, 155-178.

19. Balasubramanian, M.K., Bi, E. and Glotzer, M., *Comparative analysis of cytokinesis in budding yeast, fission yeast and animal cells.* Curr. Biol, 2004, **14**, R806-R818.

20. Wolfe, B.A.G., K.L., *Split decisions: coordinating cytokinesis in yeast.* Trends Cell Biol, 2005, **15**, 10-18.

21. Chanez, A.-L., *Division of the single mitochondrion in Trypanosoma brucei and its impact on the cell cycle*, in Département de Biologie, Unité de Zoologie 2006, Université de Fribourg: Suisse. p. 102.

22. Pär Nordlund and Peter Reichard, *Ribonucleotide Reductases*. Annual Review of Biochemistry 2006, **75**, 681-706.

23. Ollagnier S, M.E., Gaillard J, Elias son R, Fontecave M, Reichard P., *The anaerobic Escherichia coli ribonucleotide reductase. Subunit structure and iron sulfur center*. J. Biol. Chem. , 1996, **271**, 9410-9416.

24. Bult C.J., W.O., Olsen GJ, Zhou L, Fleischmann RD, et al., *Complete genome sequence of the methanogenic archaeon, Methanococcus jannaschii.* Science, 1996, **273**, 1058-1073.

25. Nordlund, P.E., H., *Structure and Function of the Escherichia Coli*, Journal of Biological Chemistry, 1993, **268**, 8383-8386

26. Jordan, A. and P. Reichard, *Ribonucleotide reductases.* Annual Review of Biochemistry, 1998, **67**, 71-98.

27. Akos Sveiczera, John J. Tysonb and Bela Novaka, *A stochastic, molecular model of the fission yeast cell cycle: role of the nucleocytoplasmic ratio in cycle time regulation*, Biophysical Chemistry, 2001, **92**, 1-15.

28. J. Shao, B.Z., Bernard Chu and Y. Yen, *Ribonucleotide Reductase Inhibitors and Future Drug Design*. Current Cancer Drug Targets, 2006, **6**, 409-431.

29. Jordan A, P.E., Atta M, Krook M, Gibert I. et al., Proc. Natl. Acad. Sci. USA, 1994, **91**, 12892-96.

30. Elledge, S.J., Zhou, Z. and Allen, J.B., *Ribonucleotide reductase: regulation*. Trends in Biochemical Science, 1992, **17**, 119-123.

31. Elledge, R.W., *Two genes differentially regulated in the cell cycle and by DNA-damaging agents encode alternative regulatory subunits of ribonucleotide reductase.* Genes and Development 1990, **4**, 740-751.

32. Atta, M.N., P, Aberg, Eklund,H. &Fontecave, M., *Substitution of manganes for iron in ribonucleotide reductase from Escherichia coli. Spectroscopic and crystallographic characterization*. Journal of Biological Chemistry, 1992, **267**, 20682-20688.

33. Eklund, U.U.H., *Structure of ribonucleotide reductase protein R1*. Nature , 1994, **370**, 533-539.

34. Reichard, P., *Interaction between deoxyribonucleotide andDNA synthesis*. Annu. Rev. Biochem, 1988, **57**, 349-374.

35. Reichard, P., Eliasson, R., Ingemarson, R., and Thelander, L, *Cross-talk between the allosteric effector-binding site in mouse ribonucleotide reductase*. J. Biol. Chem. , 2000, **275**, 33021-33026.

36. www.accessexcellence.org, Cell Chemistry.

37. Stubbe, J., *Ribonucleotide reductases in the first century*. Proceedings of the National Academy of Science of the United States of America, 1998, **95**, 2723-2724.

38. Offenbacher, A.R., Vassiliev, I.R., Seyedsayamdost, M.R., Stubbe, J. & Barry, B.A., *Redox-Linked Structural Changes in Ribonucleotide Reductase.* Journal of the American Chemical Society, 2009, **131**, 7496-7497.

39. www.genedb.org, CDS Suc22.

40. Karlsson, M., Sahlin, M. &Sjaqberg, B.M, *Escherichia coli ribonucleotide reductase. Radical susceptibility to hydroxyurea is dependent on the regulatory state of the enzyme*. Journal of Biological Chemistry 1992, **267**, 12622-12626.

41. Jordan A, P.E., A slund F, Hellman U, Gibert I, Reichard P.,*The Ribonucleotide reductase,* J. Biol. Chem., 1996, **271**, 8779-85.

42. Thelander, L.a.R., P., *Reduction of Ribonucleotides*. Annual Review of Biochemistry, 1979, **48**, 133-158.

43. Jeremy M Berg, J.L.T.L.S., Johns Hopkins ed. Biochemistry 5th editionUniversity School of Medicine, Carleton College and Stanford University. New York 5th edition,. 2002.

44. Gordon, C.B., and Fantes, P. A., *The Cdc22 gene of Schizosaccharomyces pombe encodes a cell cycle-regulated transcript.* EMBO J., 1986, **5**, 2981-2985.

45. Fernandez Sarabia, M.-J., McInerny, C., Harris, P., Gordon, C. and Fantes, P., *The cell cycle genes cdc22+ and suc22+ of the fission yeast Schizosaccharomyces pombe encode the large and small subunit of ribonucleotide reductase*. Mol. Gen. Genet, 1993, **238**, 241-251.

46. Harris, P., Kersey, P. J., McInerny, C. J., and Fantes, P. A., *Cell cycle, DNA damage and heat shock regulate succ22+ expression in fission yeast*. Mol. Gen. Genet, 1996, **252**, 284-291.

47. Liu, C., Powell, K.A., Mundt, K., Wu, L., Carr,A.M.,and Caspari,T., *Cop9/sgnalosome subunits and Pcu4 regulate ribonucleotide reductase by both checkpoint-dependent and independent mechanisms*. Genes Dev., 2003, **9**, 1130-1140.

48. Kurtzman, C.P., Fell, J.W. 2006. *"Yeast Systematics and Phylogeny—Implications of Molecular Identification Methods for Studies in Ecology.", Biodiversity and Ecophysiology of Yeasts*, The Yeast Handbook, Springer, 2007.

49. NingWei and XingWang Deng, *THE COP9 SIGNALOSOME*. Annu. Rev. Cell Dev. Biol, 2003, **19**, 261-86.

50. Schwechheimer, C.*et al., Interactions of the COP9 signalosome with the E3 ubiquitin ligase SCFTIRI in mediating auxin response.* Science 2001, **292**, 1379-1382.

51. Mundt, K.E.P., J., Murray, J. M., Brikos, C., Christensen, P.U., Caspari, T., Hagan, I.M., Millar, J. B., Simanis, V., Hofmannn, K., and Carr. A.M.T., *The Cop9/Signalosome complex is conserved in fission yeast and a role in S phase.* Curr. Biol. Cell, 1999, **13**, 493-502.

52. Thrower, J., Hoffman,Rechsteiner, *Recognition of the polyubiuitin proteolytic signal.* Pichart EMBO journal 2000, **19**(1), 94-102.

53. Gregory A., C.J.D., *Cop9/signalsosme a multifunctional regulator of SCF and other Cullin-based ubiquitin ligase.* Cell 2003, **114**, 663-671.

54. Nurse P, T.P., Nasmyth K., *Genetic control of the cell division cycle in the fission yeast Schizosaccharomyces pombe.* Mol Gen Genet, 1976, **146**, 167-78.

55. Borgne, A.N., P. T., *The Spd1p S phase inhibitor can activate the DNA replication checkpoint pathway in fission yeas*. J Cell Sci, 2000, **113**, 4341-4350.

56. Pelle Håkansson, L.D., Olga Chilkova, *The Schizosaccharomyces pombe Replication Inhibitor Spd1 Regulates Ribonucleotide Reductase Activity and dNTPs by Binding to the Large Cdc22*. The American Society for Biochemistry and Molecular Biology, 2005, **281**, 1778-1783.

57. Liu, C.e.a., *Transactivation of Schizosaccharomyces pombe cdt2+stimulates a Pcu4-Ddb1-CSN ubiquitin ligase*. EMBO J 2005, **24**, 3940-3951.

58. Holmberg, C.*et al.*, *Ddb1 controls genome stability and meiosis in fissionyeast.* Genes & Development 2005, **19**, 853-862

59. Alo Nag, T.B., Shalu Shiv, and Pradip Raychaudhuri, *The Xeroderma Pigmentosum Group E Gene Product DDB2 Is a Specific Target of Cullin 4A in Mammalian Cells. molecular and cellular biology*, 2001, **21**, 6738-6747.

60. Tanya Bondar, A.P.P.R., *Ddb1 Is Required for the Proteolysis of the Schizosaccharomyces pombe Replication Inhibitor Spd1 during S Phase and after `DNA Damage.* The journal of biological chemistry 2004, **279**(11), 9937-9943.

61. Takahashi, S., Kontani, K., Araki, Y. & Katada, T., *Caf1 regulates translocation of ribonucleotide reductase by releasing nucleoplasmic Spd1- Suc22 assembly*. Nucl. Acids Res, 2007, **35**, 1187-1197.

62. Lee YD, W.J., Stubbe J, Elledge SJ., *Dif1 is a DNAdamage- regulated facilitator of nuclear import for ribonucleotide reductase*. Mol Cell, 2008, **32**, 70-80.

63. Konstantinos Nestoras, A.H.M., Ann-Sofie Schreurs, et al., *Regulation of ribonucleotide reductase by Spd1 involves multiple mechanisms,* Genes & Development, 2010, **24**, 1145-1159.

64. Basrai M.A., V.V., Kinzler KW, Hieter P., *NORF5/ HUG1 is a component of the MEC1-mediated checkpoint response to DNA damage and replication arrest in Saccharomyces cerevisiae.* Mol Cell Biol 1999. **19**: p. 7041-7049.

65. Benton MG, S.S., Glasner JD, Palecek SP, *Analyzing the dose-dependence of the Saccharomyces cerevisiae global transcriptional response to methyl methanesulfonate and ionizing radiation*, BMC Genomics, 2006, **7**, 1-18.

66. Zhao X, G.B., Chabes A, Domkin V, Ippel JH, Schleucher J, Wijmenga S, Thelander L, Rothstein R., *Mutational and structural analyses of the ribonucleotide reductase inhibitor Sml1 define its Rnr1 interaction domain whose inactivation allows suppression of mec1 and rad53 lethality*. Mol Cell Biol, 2000, **20**, 9076-9083.

67. Russell, N.R.a.P., *Chk1 and Cds1: linchpins of the DNA damage and replication checkpoint pathways.* Journal of Cell Science 2000, **113**, 3889-3896

68. Carr A.M., *DNA checkpoints in fission yeast*. Journal of Cell Science 2003, **116**, 3847-3848.

69. Mizianty MJ, S.W., Chen K, Kedarisetti KD, Disfani FM, Kurgan L., I*mproved sequence-based prediction of disordered regions with multilayer fusion of multiple information sources*. Bioinformatics (Oxford, England), 2010, **26**, 1489-1496.

70. Håkansson, P. and O.C. Lina Dahl, Vladimir Domkin, and Lars Thelander, *The Schizosaccharomyces pombe Replication Inhibitor Spd1 Regulates Ribonucleotide Reductase Activity and dNTPs by Binding to the Large Cdc22 Subunit*, Journal of Biological Chemistry, 2006, **281**(3), 1778-1783.

71. Orly Noivirt-Brik, *Low folding propensity and high translation efficiency distinguish in vivo substrates of GroEL from other Escherichia coli protein*. Bioformatics, 2007, **23**(24), 3276-3279.

72. Vale´ rie Leuranguer, S.P.K.G.B., *Organization of Calcium Channel β1a Subunits in TriadJunctions in Skeletal Muscle*. Journal of Biological Chemistry, 2006, **281**(6), 3521-3527.

73. Ammasi Periasamy, H.W., Ye Chen and Margarida Barroso, *Quantitation of Protein–Protein Interactions: Confocal FRET Microscopy.* Methods in Cell Biology, 2008, **89**, 569-598.

74. Jares-Erijman, E.A.J.T.M., *Principles of Resonance Energy Transfer.* Nat. Biotechnol, 2003, **21**, 1387-1395.

75. Aka, M.K.O.B., *A Nanoscale Communication Channel with Fluorescence Resonance Energy Transfer (FRET).* Molecular and Nano Scale Communication (MoNaCom), 2009, 425-430.

76. YE Chen, M.E.A.A.P., *FRET Data Analysis:* The Algorith. Oxford University Pres, 2005, Chapter 7, 1-43.

77. Geddes, C.D., *Reviews in Fluorescence 2008 Science*, 2009, **5**, 489.

78. Periasamy, Y.C.a.A., *Quantitative FRET data analysis: protein localization in living specimens*. Conference Proceedings, 2006, 519-524

79. Stephen W. Paddock, *Confocal Laser Scanning Confocal Microscopy, Molecular Biotechnology*, 1999, **27**, 992-1004.

80. Stokes, G.G.P., Trans., 1952, **142**, 463-562.

81. J. Pawley, *Fundamental Limits in Confocal Microscopy*, J. B. Pawley (ed.), Handbook of Biological Confocal Microscopy, New York: Plenum Press, 2000, 19-37.

82. Pawley, J.B., *Handbook of Biological confocal microscopy.*, Science, 2006, Third Edition, 985.

83. Minisky Marvin, *Memoir on inventing the confocal scanning microscope*. Scanning, 1988, **10**, 128-138.

84. Minsky, M., *Microscopy Apparatus*. USA Pat., 1961, **3**(013), 467.

85. Nathan S. Claxton, and Michael W. Davidson, *Laser scanning confocal microscopy*, Department of Optical Microscopy and Digital Imaging, National High Magnetic Field Laboratory, The Florida State University, Tallahassee, Florida, 32310, retrieved Feb 15 2008 from

http://www.microscopyu.com/tutorials/java/virtual/confocal/index.

86. G. J. Brakenhoff, P.B., and P. Barends, *Confocal Scanning Light Microscopy with High Aperture Immersion Lenses. Journal of Microscopy*, 1979, **117**, 219-232.

87. Pawley, J.B., *Handbook of Biological Confocal Microscopy*, New York Press, 1995.

88. Pawley, J.B., and Centonze, V., *Practical laser-scanning confocal light microscopy: Obtaining optimal performance from your instrument*, In: Cell Biology: A Laboratory Handbook (J.E. Celis, ed.), New York. Press, 1997, 44-64.

89. Inoue, S., *In The Hand of Biological Confocal Microscopy,* IMR Press Madison,1986, 92-97.

90. R, I.S., S.K., Video Microscopy: *The Fundamentals* Plenum: (New York.), 1997,

91. White, J.G., Amos, W.B., Fordham, M., *An evaluation of confocal versus conventional imaging of biological structures by fluorescence light microscopy.* J. Cell Biology, 1987,. **105**, 41-48.

92. White, A.and.J.G., *How the Confocal Laser Scanning Microscope entered Biological Research.* Biology of the Cell, 2003, **95**, 335-342.

93. Stelzer, E.H.K., *Contrast, Resolution, Pixelation, Dynamic range, and Signal-to-Noise Ratio: Fundamental Limits to Resolution in Fluorescence Light Microscopy*. Journal of Microscopy, 1997, **189**, 15-24.

94. Stelzer, E.H.K., *Practical Limits to Resolution in Fluorescence Light Microscopy,* Imaging Neurons: A Laboratory Manual. New York: Cold Spring HarborPress, 2000, 12.1-12.9

95. Murray, J., *Confocal Microscopy Deconvolution, and Structured Illumination Methods*, Live Cell Imaging: A Laboratory Manual, New York:, Cold Spring Harbor Press, 2005, 239-280.

96. K. R. Spring and S. Inoué, Video Microscopy: The Fundamentals, in New York: Plenum Press. 1997. p 1-741

97. Cohen, S.N., A. C. Y. Chang, H. W. Boyer, and R. B. Helling and y. *genetics, Construction of biologically functional bacterial plasmids in vitro*, Proc. Natl. Acad. Sci. USA, 1973, **70**, 3240-3244.

98. Lee, M.G.N., P., *Complementation used to clone a human homologue of the fission yeast cell cycle control gene cdc2.* Nature, 1987, **327**, 31-35.

99. Fields S, S.O., *A novel genetic system to detect protein-protein interactions.* Nature, 1989, **340**(6230), 245-6.

100. Krishna S., S.R., Helena R., and Paul R., *Human homolog of fission yeast cdc25 mitotic inducer is predominantly expressed in G2.* Proc. Nati. Acad. Sci. USA 1990, **87**, 5139-514.

101. Christian M. Udell, S.K.L.S.D., *HRAD1 and MRAD1 encode mammalian homologues of the fission yeast rad1+ cell cycle checkpoint control gene5*. Oxford University Press Nucleic Acids Research, 1998, **26**(17), 3971-3976.

102. Julian Lai, S.K.N., Fang Fang Liu, Rajesh Narhari Patkar, Yanfen Lu, Jing Ru Chan, Angayarkanni Suresh, Naweed Naqvi, and Gregory Jedd, Marker Fusion Tagging, a *New Method for Production of Chromosomally Encoded Fusion Proteins.* American Society for Microbiology, 2010, **9** (5), 827-830.

103. Werler P.J., H.E., Carr AM., *A simple Cre-loxP method for chromosomal Nterminal tagging of essential and non-essential Schizosaccharomyces pombe genes*. Gene 2003, **304**, 133-41.

104. Caspari T., D.M., Kanter-Smoler G., Lindsay H.D., Hoffmann K., Papadimitriou K.,Sunnerhagen P.,Carr A.M., *Characterization ofSchizosaccharomyces pombe Hus1: A PCNA-related protein that associates with Rad1 and Rad9.* Mol. Cell. Biol., 2000, **74**, 1254-1262.

105. Pelle Håkansson, L.D., Olga Chilkova, Vladimir Domkin and Lars Thelander. Department of Medical Biochemistry and Biophysics, Umeå University, SE-901 87 Umeå, Sweden. JBC Papers in Press, 2005.

106. Holmberg C, F.O., Hansen HA, Liu C, Slaaby R, Carr AM, Nielsen O, *Ddb1 controls genome stability and meiosis in fission yeast*. Genes Dev 2005, **19**, 853-862.

107. Wu X, Hung M., *Dif1 controls subcellular localization of ribonucleotide reductase by mediating nuclear import of the R2 subunit*. Mol Cell Biol 2008, **28**,7156-7167.

108. Nordlund, P.r.R., P., *Ribonucleotide Reductases*. Annual Review of Biochemistry, 2006, **75**, 681-706.

109. D., S., *FRETcalc plugin for calculation of FRET in non-continuous intracellular compartments.* Biochem Biophys Res Commun., 2007, **175557**.

110. Robert D. Goldman, D.L.S., *Live cell imaging:a laboratory manual*. Science 2005, 631.

111. Nuno M.F.S.A. Cerqueria, P.A.F.a.M.J.R., *Ribonucleutide reductase :A critical enzyme for cancer chemotherapy and antiviral agent*. Bentham Science Publishers Ltd., 2007, **2**, 11-29.

112. Zhang Z, A.X., Yang K, Perlstein DL, Hicks L, Kelleher N, Stubbe J, Huang M., *Nuclear localization of the Saccharomyces cerevisiae ribonucleotide reductase small subunit requires a karyopherin and a WD40 repeat protein*. Proc Natl Acad Sci U S A 2006, **103**, 1422-1427.

113. Rofougaran, R., Crona, M., Vodnala, M., SjÃberg, B.-M. & Hofer, *A.*, *Oligomerization Status Directs Overall Activity Regulation of the Escherichia coli Class Ia Ribonucleotide Reductase*. Journal of Biological Chemistry 2008. **283**, 35310-35318.

114. Rofougaran R, V.M., &Hofer A., *Enzymatically active mammalian ribonucleotide reductase exists primarily as an alpha6beta2 octamer*. Journal of Biological Chemistry, 2006, **281**, 27705-27711.

115. Gallo, G.J., Prentice, H. & Kingston, R.E. , *Heat shock factor is required for growth at normal temperatures in the fission yeast Schizosaccharomyces pombe*. Mol. Cell. Biol., 1993, **13**, 749-761.

116. Wu X, H. M., *Dif1 controls subcellular localization of ribonucleotide reductase by mediating nuclear import of the R2 subunit.* Mol Cell Biol, 2008, **28**, 7156-7167.

117. P. Tomp., Intrinsically unstructured proteins. Trends Biochem Sci, 2002, **27**, 527.

118. Sugase K, D. H., Wright P.E., *Mechanism of coupled folding and binding of an intrinsically disordered protein*. Nature 2007, **447**, 1021-1025.

119. Elford, H.L., *Effect of hydroxyurea on ribonucleotide reductase.* Biochemical and Biophysical Research Communications, 1968, **33**, 129-135.

120. Truong, K.I., M. T., *The use of FRET imaging microscopy to detect protein-protein interactions and protein conformational changes in vivo*. Current Opinion in Structural Biology, 2001, **11**, 573-578.

121. Kenworthy, A.K., *Imaging Protein-Protein Interactions Using Fluorescence Resonance Energy Transfer Microscopy*. Methods, 2001, **24**, 289-296.

122. Deniz, A.A., Mukhopadhyay, S. & Lemke, E.A., *Single-molecule biophysics: at the interface of biology, physics and chemistry*. Journal of The Royal Society Interface, 2008, **5**, 15-45

123. Axelrod D., *Total Internal Reflection Fluorescence Microscopy and in Cell Biology*. Traffic, 2001, 764-774.

124. Nancy L Thompson and B Christoffer Lagerholm, *Total internal reflection fluorescence: applications in cellular biophysics*, Current Biology Ltd, 8, 58-64.

125. Mattheyses AL, S.S., Rappoport J. Z, *Imaging with total internal reflection fluorescence microscopy for the cell biologist*. J. Cell Sci. 2010, 3621-8.

126. Ana J. and Petra Schwille, A.J.G.-S., *Surface analysis of membrane dynamics*, Elsevier, 2009, 766-776.

127. Merrifield, C.J., Feldman, M.E., Wan, L., and Almers, W., *Imaging actin and dynamin recruitment during invagination of single clathrin-coated pits*. NatureCellBiology, 2002, **4**, 691-698.

128. Iwadate Y, Y.S., *Molecular dynamics and forces of a motile cell simultaneously visualized by TIRF and force microscopies.* Biotechniques, 2008, 44739-50.

129. H. Peter Lu and .X. Sunny Xie, *Single -Molecules Kinetics of interfacial Electron Transfer*, J. Phys. Chem. B. 1997, **101**, 2753-2757.

130. Yildiz, A.F., J.N., McKinney, S.A., Ha, T.J., Goldman, Y.E.; Selvin, P.R.: *Walks hand-over-hand: Single fluorophore imaging with 1.5-nm.* Science, 2003, **300**, 2061-2065.

131. Gordon, M.P.H., T., Selvin, P.R., *Single molecule high resolution imaging*, Proc. Natl. Acad. Sci. U.S.A., 2004, **17**(101), 6462-6465.

132. Toprak E., Enderlein J.; Syed S.; McKinney S.A.; Petschek R.G.; Ha T.; Goldman Y.E.; Selvin P.R. *Defocused orientation and position imaging (DOPI) of myosin,*V. Poc. Natl. Acad. Sci.*:* 2006, **103**, 6495-6499.

133. Huang, B.W., W., Bates, M., Zhuang X., *Three dimensional super- Resolution Imaging by Stochastic Optical Reconstraction Microscopy,* Science, 2008, **319**, 810-813.

134. Tipler, P.A., *Physics for Scientist and Engineers*, 4th Edition. W.H Freeman Company, 1999, 1044.

135. Edman, L.M., U., Rigler, R. *Conformational transitions monitored for single molecules in solution,* Proc. Natl. Acad. Sci. U.S.A. 1996, **93**, 6710-6715.

136. Tokunaga M., I.N., Sakata-Sogawa K., *Highly inclined thin illumination enables clear single-molecule imaging in cells*. Nat. Methods, 2008, **5**, 159-16.

137. Marcel van 't Hoff, V.d.S., and Martin Oheim, *A programmable light engine for quantitativesingle molecule TIRF and HILO imaging*. Optical Society of America, 2008. **16**: p. 18495-18504.

138. Wolleschensky, R., *Arrangement for microscopic observation and/or detection in a light scanning microscope with line scanning and use*. US Patent Appl. US, 2008, 20080030850.

139. Eli Peli, *Contrast in complex images*. J. Opt. Soc. Am. A, 1990, **7**, 2032-2040.

140 Hershko A, Ciechanover, *The ubiquitin system*. Annu Rev Biochem., 1998, **67**, 425-79.

141 Michael H. Glickman and Aaron Ciechanover, *The Ubiquitin-Proteasome Proteolytic Pathway: Destruction for the Sake of Construction*, Physiol Rev. 2002, **82**, 373–428.

Publication:

Konstantinos Nestoras, Asma Hadi Mohammed, Ann-Sofie Schreurs, *et al.*, *Regulation of Ribonucleotide Reductase by Spd1 involves multiple mechanisms*, Genes Dev. 2010 24: p 1145-1159